UNIVERSIDAD POLITÉCNICA DE MADRID

ESCUELA TÉCNICA SUPERIOR
DE INGENIEROS DE TELECOMUNICACIÓN

A MODULAR DATA ACQUISITION SYSTEM FOR HIGH RESOLUTION CLINICAL PET SCANNERS

TESIS DOCTORAL

Giancarlo Sportelli
Ingeniero en Electrónica

2010

DEPARTAMENTO DE INGENIERÍA ELECTRÓNICA

ESCUELA TÉCNICA SUPERIOR DE INGENIEROS DE TELECOMUNICACIÓN

PH.D. THESIS

A MODULAR DATA ACQUISITION SYSTEM FOR HIGH RESOLUTION CLINICAL PET SCANNERS

Author:

Giancarlo Sportelli
Electronics Engineer

Advisors:

Andrés Santos Lleó
Telecommunication Engineer, Ph.D.

Pedro Guerra Gutiérrez
Telecommunication Engineer, Ph.D.

2010

UNIVERSIDAD POLITÉCNICA DE MADRID

Tribunal nombrado por el Magfco. y Excmo. Sr. Rector de la Universidad Politécnica de Madrid, el día de de 2010

Presidente: ____

Secretario: ____

Vocal: ____

Vocal: ____

Vocal: ____

Realizado el acto de defensa y lectura de Tesis el día de de 2010
en la E.T.S. de Ingenieros de Telecomunicación
Calificación:

EL PRESIDENTE EL SECRETARIO

LOS VOCALES

.

Biomedical Image Technologies
Departamento de Ingeniería Electrónica
Escuela Técnica Superior de Ingenieros de Telecomunicación
Universidad Politécnica de Madrid

Ph.D. Thesis
A Modular Data Acquisition System For High Resolution Clinical PET Scanners

Author
Giancarlo Sportelli

Advisors
Andrés Santos and Pedro Guerra Gutiérrez

This Ph.D. Thesis has been carried out in close collaboration with the Dipartimento di Fisica of the Universitá di Pisa. The research internships in this institution have been supervised by Alberto Del Guerra.

Resumen

En las últimas dos décadas, la Tomografía por Emisión de Positrones (PET) ha demostrado ser una modalidad clave para el estudio de la biología del cáncer y trastornos cardíacos, y para la realización *imágenes moleculares*, una técnica que permite la terapia individualizada de la enfermedad [Weissleder01].

La mejor característica de la PET es su sensibilidad: es la técnica que proporciona imágenes moleculares con la mayor sensibilidad, y las imágenes de cuerpo entero que produce no pueden ser igualadas por otras modalidades [Hoh97, Chae07].

Por otra parte, la PET no proporciona referencias anatómicas, lo cual es un problema fácilmente resoluble a través de su integración o coregistro con la tomografía computarizada de rayos X (CT) [Lu07]. Además, en comparación con otras modalidades de imagen, la PET se caracteriza por bajas estadísticas de conteo (es decir, desintegraciones por unidad de tiempo), lo cual generalmente limita la resolución de la imagen. Sin embargo, detectores con geometrías dedicadas permiten solventar ester problema, y producir excelentes resultados [Humm03]. Dos ejemplos destacables de especialización, que tomaremos como aplicaciones de referencia, son la Mamografía por Emisión de Positrones (PEM) y la monitorización en línea de dosis en hadroterapia (in-beam PET o, brevemente, ibPET).

Las amplias posibilidades de especialización tienen, sin embargo, una contrapartida: es necesario el desarrollo de sistemas de adquisición igualmente especializados, cuyo coste y prestaciones puede impedir de hecho conseguir las ventajas teóricas proporcionadas por una geometría dedicada.

El objetivo de esta tesis doctoral es proponer una nueva arquitectura tecnológica flexible, capaz de obtener prestaciones similares al estado del arte en distintas aplicaciones, a través de una plataforma de adquisición compacta y eficiente en coste, adecuada para PEM e ibPET.

En primer lugar, se explorarán el estado del arte y los problemas que han evitado la amplia difusión de equipos PET dedicados en entornos clínicos. Especial atención se dedicará a las soluciones tecnológicas y las características de los escáneres PEM anteriores. Se revisará también la situación de los equipos ibPET, especialmente las prestaciones requeridas para soportar eficazmente la planificación de tratamiento en hadroterapia.

En segundo lugar, se tratará un diseño conceptual propuesto como solución al problema. Se propondrán y justificarán diferentes alternativas, con el fin de maximizar la eficiencia de detección y minimizar el coste. A través de una serie de prototipos intermedios, se implementarán y caracterizarán las opciones de diseño elegidas.

Por ultimo, se propondrá el diseño e implementación de un prototipo final de sistema de adquisición. El equipo en cuestión integrará y extenderá la soluciones validadas con los prototipos anteriores.

La investigación llevada a cabo durante esta tesis ha permitido realizar un sistema de adquisición, con prestaciones al estado del arte, apto para el uso de PET dedicado en el entorno clínico del paciente, y que apoyará la investigación en PEM e ibPET.

Summary

In the last two decades, Positron Emission Tomography (PET) showed to be a key modality to interrogate biology for cancer and cardiac disorders, and to perform *molecular imaging*, a technology that permits individualized therapy of disease [Weissleder01].

PET's best characteristic is sensitivity: it is the most sensitive technique for medical molecular imaging, and the whole-body images it produces are unequalled by any other modality [Hoh97, Chae07]. Of course, it lacks anatomical reference, but this is a problem that can be easily overcome with X-ray (CT) (Computed Tomography) integration or coregistration [Lu07]. Moreover, even if PET uses relatively low statistics with respect to other modalities, which generally limits image resolution, it can produce excellent results by using dedicated detector geometries [Humm03]. Two remarkable examples for this kind of system specialization, that we will take as reference applications, are Positron Emission Mammography (PEM) and in-beam PET (ibPET) for dose delivery monitoring in hadrontherapy.

However, the wide range of design possibilities has a counter effect: it requires the development of specifically tailored acquisition systems, whose cost and performances could actually prevent the achievement of the theoretical advantages obtainable with a specialized detector assembly.

This doctoral thesis aims at proposing an alternative technological architecture, able to achieve state of the art PET imaging performances by means of a compact, cost efficient acquisition platform, suitable for its adoption in both PEM and ibPET.

Firstly, the state of the art and the controversies that prevent the broad use of dedicated PET in clinics will be explored. Special attention will be paid to the technological solutions and characteristics of previous PEM scanners. It will be also reviewed the current status of ibPET, with particular focus on the performances required to effectively support treatment planning in hadrontherapy.

Secondly, a conceptual design solution will be discussed. Various alternatives will be proposed and justified, with the aim of maximizing detection efficiency and minimize system cost. Through a series of intermediate prototypes the various design choices are implemented and characterized.

Thirdly, a final prototype of the acquisition system is designed and implemented. This piece of hardware integrates and extends the solutions that have been validated through the previous systems.

The research carried out during this thesis has allowed realizing a state of the art acquisition system that is suitable for specialized PET imaging in the clinical environment of the patient, and that will be used for further research in PEM and ibPET imaging.

Contents

List of Figures

List of Tables

Per Mariangela

”It is not the strongest of the species that survives, nor the most intelligent, but rather the one most adaptable to change.”

Said by Clarence Darrow,
erroneously citing Charles Darwin,
during its defence in the *Scopes Monkey Trial* in 1925.

Chapter 1

Introduction

Positron emission tomography (PET) is the imaging modality of choice when it comes to diagnose and survey cancer in humans. This thesis intends to contribute to the recent efforts in making this modality also a convenient tool for cancer prevention and control.

The reason of researching in imaging technology for fighting cancer, the second cause of death in men [WHO08], comes from its strong resistance against standard therapy methods. Today cancer mortality is almost the same as thirty years ago, which makes a strong contrast with heart diseases mortality, still the first cause of death, that dropped by 56% in people below 85 years and by 35% in older people [Jemal09]. Despite the notable advances in chemio-, radio-therapy and cancer surgery, it is a fact that once cancer manifests, the patient's life-expectancy reduces dramatically, unless it is still at an early growing stage. The natural deduction is that newer strategies must be adopted in order to protect cancer affected patients.

The worldwide organized response against Cancer is embodied by the concept of *Cancer Control* [Boyle08] which develops in three levels of prevention: risk reduction, prompt cancer treatment and eventually cancer recovery. The European Union *Code Against Cancer*, is a good example of achieving Cancer Control through the first two levels, commonly referred to as *primary* and *secondary prevention* [Boyle03]. During the lifespan of the "Europe Against Cancer" program, cancer mortality in the EU Member States had started to decline and left the evidence that the majority of human cancers might be avoidable, and for several of them, avoidable causes have been already identified. In global terms, the greatest impact would be from the control of tobacco smoking and the control of breast cancer [IARC04]. However, while tobacco control could be achieved using a series of government and social actions [Boyle04], prospects for the prevention of other cancers, most of all breast cancer, are more remote.

Failing primary prevention, preventive cancer screening could have significant effect on reducing mortality from this common disease. With the expansion in the absolute numbers of cases of cancer set to continue into the next decades, the role of prevention in cancer control strategies will increase in importance. A major challenge for many countries is finding sufficient funds to develop the capacity to treat the large numbers of cancers that will be diagnosed in the coming years. Effective prevention would reduce the risk of cancer and effective screening would allow many others to be successfully treated for their disease. But the benefit-cost ratio represents a determinant, limiting factor.

Although increasingly many medium-resource countries assign high priority in their national health strategies to chronic diseases including cancer, the donor community and most bilateral development agencies do not as yet consider cancer control a high priority. If cancer is not given higher priority through focused global efforts, health-care systems in low-resource and middle-resource countries will encounter even further problems as the number of cancer cases increases. Cancer could become a major impediment to socioeconomic development in low resource and economically emerging nations [Boyle08].

1.1 Motivation of this thesis

The need of new diagnostic methods for cancer control motivated the beginning of this work. The good results obtained in the past with preclinical, high resolution PET scanners, in particular the recent achievements in digital acquisition systems of our group [Guerra08], and the general scientific trend of the last decade in researching on improved PET scanners for humans, often adopting techniques already proven in small animal imaging, made us willing to contribute the field of dedicated PET imaging for clinical environments.

Most interesting dedicated clinical PET applications include brain, prostate and breast imaging [Zaidi06,Schuster07,Thompson06]. Recently, the first and currently only commercially available dedicated breast scanner, the PEM Flex Solo II (Naviscan Inc, San Diego, U.S.A.), has shown interesting results in cancer screening [Weinberg05a]. As it will be discussed more in the next chapter, first clinical trials in the U.S.A. with PEM Flex showed that PEM could overcome many of the limitations of current imaging techniques.

We believe indeed that PEM is a promising technique and for this reason we started researching on it. In doing so, we established a collaboration with the Functional Imaging and Instrumentation Group (FIIG) of the Università di Pisa, one of the most active European groups in dedicated clinical

PET imaging. A scientific collaboration agreement, signed in 2006 between the FIIG and the BIT (Biomedical Imaging Technologies) group, settles the starting point of the joint work on the realization of a positron emission imager for nuclear medicine applications and, as the first impulsing action, a first short stay of three months has been realized with the initial aim of deepen our studies on the field.

The stay resulted very fruitful. After only three months the main challenges for the enhancement of current PEM state of the art were identified, and the basis for a new PEM scanner with a novel architecture and improved characteristics were settled. We also set up a collaborative framework in which participated members of the BIT, FIIG, INFN (Istituto Nazionale di Fisica Nucleare) and AGE Scientific. In the context of this collaborative framework each party was assigned with specific competencies and technical responsibilities, as they will be described in the course of this text. As it became paramount to work closely, on many of the aspects of this research, a further stay of six months has been done in Pisa, and as a result two PEM prototypes have been realized.

As an additional result of this tight and profitable collaboration, we become in contact with another ongoing project of INFN, the *Treatment Planning System* (TPS) project, and its applications in hadrontherapy. In fact, one of the fundamental bricks of a hadrontherapy facility is the dose delivery monitoring system, which will be further described, and the most promising monitoring technique is precisely positron emission imaging. Such a positron imager has to be placed around the therapeutic hadron beam, therefore is referred to as in-beam PET, or briefly ibPET. Moreover, the detector geometry chosen in the TPS project is the dual planar head, exactly the same as the one adopted for our PEM, and most of acquisition requirements are shared between both systems. It became then natural, prior to the design of the new prototype, to focus the ongoing studies on both applications.

This thesis contributes to both project by providing the knowledge necessary to design an efficient, feasible acquisition system for both applications, and it has been carried out under the supervision of Prof. Andres Santos and Dr. Pedro Guerra, with the financement of the "Consejería de Educación de la Comunidad de Madrid" and the European Social Fund. The work accomplished during the stays in Pisa has been also directed by Prof. Alberto Del Guerra and Dr. Nicola Belcari, who directed and supported the acquisition tests at FIIG laboratories and at the CNR (Consiglio Nazionale delle Ricerche).

1.2 Objective of this thesis

The thesis here presented is committed to the research on the optimal acquisition strategy for a planar configurable PET system for both PEM and ibPET, and a given detector technology. The geometry of choice is the dual planar head, but a degree of freedom must be kept on the number and arrangement of opposed head detector modules. The research will focus in detecting possible bottlenecks and architectural traps that could hamper the applicability of the system to one of the cited applications. Moreover, the key requirements of both PEM and ibPET will be analysed from the technological point of view, in order to determine similarities and differences that might imply specific design constraints.

The objective is to equal state of the art acquisition performances within a self-consistent, compact, cost-efficient hardware equipment, compatible with the clinical out-patient environment. The key performance parameters that will be tackled will be dead time, data throughput and coincidence resolution.

In order to make the instrument a useful tool for further researches in nuclear imaging, such as the exploration of newer clinical applications, geometry comparisons and thoroughful detectors characterization, a critical objective is to make the system flexible and reconfigurable. Moreover, a programmable statistics collection methodology must be provided, in a manner that it can be expanded according to the specific application needs without compromising the rest of the acquisition process.

Having a comprehensive set of design constraints an acquisition architecture will be proposed and discussed. A prototype will be then realized and characterised in order to validate the model.

Achieving these objectives will require to fulfil the steps listed below:

1. Define a conceptual system design. Although a first design proposal was already present prior to this thesis, a series of questions were still unanswered and a full feasible design was not available. In order to obtain a final conceptual design the characteristics of each system component have to be studied and related to the system as a whole. Special attention must be paid to timing requirements, system bandwidth, power consumption and cost.

2. Propose a coincidence acquisition architecture. The most controversial and sophisticated hardware component of a PET system is the coincidence processor. Coincidence processing strategy is likely to have the greatest impact on development effort, system cost and power consumption. The work at this point will be aimed at reducing these variables without compromising coincidence discrimination performances.

3. Implement the proposed architecture. Once the complete system design satisfies the imposed constraints, its hardware, firmware and software will be implemented. The aim is to provide a functional prototype in order to allow system characterization.

4. Validate and characterise. The functionality of the prototype will be experimentally validated, and the properties that were tackled during this research will be characterized. Most notably, dead time will be assessed, which represents one of the main figures of merit of PET acquisition systems.

The results of the characterisation are discussed and the degree to which the objectives are achieved will be the starting point for a proposal on further research.

1.3 Work flow

The first step in defining a conceptual design is to integrate the experience and preliminary studies of collaborating parties. The main fields of expertise are on one hand the clinical applicability and requirements of both PEM and ibPET, the detector technology and PCB (Printed Circuit Board) technology, that are mainly provided by the members of FIIG, INFN and AGE Scientific; on the other hand is the FPGA (Field Programmable Gate Array) firmware/software technology that makes part of this thesis as the contribution of the BIT group. The attainment of this step has to result in a series of constraints and indicative directives.

Once all parts are put together, an operation concept must be drawn: this brings to the design of a system architecture and an acquisition protocol, taking into account the characteristics and limitations of existing sub-parts and exploring, when possible, technological alternatives. The final design must satisfy all the imposed constraints.

Most notably, coincidence processing appears to be a critical passage. Today coincidence processing is still a challenging task for the scientific community, and a considerable part of the work consists in finding a coincidence detection method suitable for our aims.

Once the architecture has been designed a prototype must be realized and characterized. The development is carried out by all the involved parties: the design of missing printed circuit boards is carried out by AGE Scientific, the design of FPGA related circuitry, firmware and software is developed by the BIT group, and the data collection and detectors characterization is completed by FIIG and INFN members.

Chapter 2

Background

2.1 High resolution PET imaging in clinics

As long as PET has been used for human whole body imaging (WB-PET), the images it produced had to face its fundamental limit: the non-collinearity effect [Derenzo93, Levin99, Stickel05]. That was not the case of preclinical imaging on small animals: being the subject much smaller, the distance between detectors could be reduced thus reducing the non-colinearity radial error [Weissleder01]. This situation led to a sort of distinction, with a few exceptions, between whole body clinical PET scanners and high-resolution HR preclinical ones.

With the introduction of dedicated clinical PET scanners, such as brain, mammography and more recently in-beam PET scanners, things are changing considerably. The main difference between small animal and clinical HR PET scanners is, let's say, the patient. This implies that the used radiopharmaceuticals have different chemical compositions and must be injected with different doses [Fowler97]. The imaging scanner is then exposed to very different radioactivity situations, and it is easy to understand that it may require different capabilities for each one of them. Usually, in the case of small animals, we are allowed to use chemical species with quite long life times, in relatively high doses, and also long lasting image scans. With humans we tend instead to use as low radiation as possible, and shorter exams, in order to minimize the risk of radiation exposure and patient's unease. But we still want high spatial resolution, which strongly depends on the quantity of acquired radiation, specially in HR scanners [Herraiz05]. Therefore, lower radioactivity in human scanners must be compensated with *higher sensitivity*.

Traditionally, preclinical PET studies covered many aspects of molecular biology, from oncology to cardiopathies and cerebral functions, while clinical PET focused in cancer surveillance. The use of WB-PET in cancer screening is still hotly debated because its high cost is not justified by any concrete evidence of improvement in the expectancy of life of screened population [Czernin02, Schoder07, Yasuda05]. We will see in detail the current condition of both cancer screening and therapy in order to understand how resolution and sensitivity can hold the balance of power between available medical scanners, and possibly find a solution that can effectively help in the fight against cancer.

2.1.1 Breast cancer screening

Breast cancer is the first cause of death for cancer in women [WHO08]. The early detection of a breast tumour is the critical factor to increase the probability for the cancer to be cured. The first test for the detection of a tumour is breast self-examination. In this way the subject is able to detect tumours only when they are large enough to be palpable, i.e., about 1 cm diameter. The detection of such large tumours does not assure a successful treatment. For the detection of smaller tumours an X-ray mammogram is the standard technique. Staging, is the process of finding out how much the cancer has grown, and hence how far the cancer has spread. This is very important because the treatment and the survival expectation depend on the staging of the cancer. The staging of breast cancer follows the TNM (Tumours, Node, Metastasis) classification [Fleming97], which is based on two factors: the metastasis level in the surrounding tissues, taking particular care of lymph nodes involvement (N), and the primary tumour dimensions (M). Following the TNM classification the tumour dimensions can be defined as:

- T1a: a tumour diameter $\in [0.1, 0.5]$ cm
- T1b: a tumour diameter $\in [0.5, 1]$ cm
- T1c: a tumour diameter $\in [1, 2]$ cm

The limit between T1b and T1c defines approximately the threshold between palpable and non-palpable tumours. Nowadays the diagnosis at T1a and T1b stage represents the fundamental step for successful therapy: in fact, at this stage, the incidence of positive lymph nodes is only 3%. On the contrary a T1c tumour, with a high invasive grade, is characterized by 49% of positive lymph nodes [Barth97]. It is clear that the most relevant diagnostic techniques for breast cancer are those that have the greatest efficiency for detecting small tumours. The efficiency of a diagnostic technique is characterized by its sensitivity and specificity defined as:

$$\text{Sensitivity} = \frac{P}{P + \overline{N}} \tag{2.1}$$

$$\text{Specificity} = \frac{N}{N + \overline{P}} \tag{2.2}$$

Where P is the number of true positives, N the number of true negatives, $\overline{P}$ and $\overline{N}$ the numbers of false positives and negatives, respectively. The sensitivity measures the capacity of the technique in detecting a cancer, while the specificity measures the capacity of the technique in diagnosing its absence. The statistical parameter that determines the minimal desired values for both sensitivity and specificity is the *positive predictive value* (PPV).

$$PPV = \frac{P}{P + \overline{P}} \tag{2.3}$$

This value depends on cancer incidence and measures the probability that the patient is correctly diagnosed positive. If the prevalence of individuals with cancer is below 5%, as it is for many breast and lung screening programs [Liberman04, Mulshine05, Jr00], the PPV is bound to be low, even if the test is highly sensitive and specific. In such conditions, in order to detect more true-positive cases than false-positives, the screening test must have an exceedingly high sensitivity, greater than 95%, if the specificity is slightly below 95%, and vice versa. Although desirable, in reality, most screening tests do not meet this standard, and this is the cause that provoked the debate on the real usefulness of screening techniques [Liberman04, Schoder07].

2.1.2 Positron emission mammography

When a breast cancer is diagnosed for the first time, the common suggested treatment is lumpectomy surgery, which requires a detailed information about the extent of the diseased tissue. X-ray mammography and clinical breast examination often do not depict the full extent of cancer. As a result, at the initial treatment surgery, a certain positive margin must be taken, thus aggravating an already aggressive therapy [Tafra07]. Moreover, these techniques have limited capabilities in early detection of small tumoural masses, which is extremely important for preventive screening.

Magnetic resonance imaging (MRI) has proved to be highly sensitive in depicting the full extent of tumour, and is often used in planning treatment

[Kriege04, Kuhl00, Buchanan05]. However, there are many non cancerous lesions that show up as suspicious on MRI, making its use recommendable with only selected high risk patients [Heywang-Köbrunner96] and, among those, it has been showed that nearly half of the times the MRI exam is declined because of the nuisance of the scan [Berg10]. Recent studies still argue that there is no evidence that MRI improves surgical care or prognosis over standard mammography [Houssami09].

Use of WB-PET for the evaluation of breast cancer has shown that most of its usefulness rests in the evaluation of patients with either an *advanced breast cancer* or those suffering recurrent breast cancer. Breast screening and primary breast tumours imaging are not recommended to be performed with WB-PET scanners, because of an insufficient sensitivity improvement respect to conventional imaging techniques [Tafra07]. Partial volume effects and varying metabolic activity seems also to represent significant limitations to spatial resolution for breast imaging in standard PET scanners [Avril00].

Single photon computed tomography (SPECT), showed that can improve the examination outcome for specific kinds of tumour, if combined with WBPET [Uematsu05]. However, the obtained sensitivity is in these cases was still lower than 85% and, therefore, insufficient [Escalona10].

The key properties of PET that seem to be insufficient in WB scanners can be enhanced by reducing the size of the field of view (which increases the detectors solid angle and reduces the non-collinearity effect), as in pre-clinical scanners. A PET scanner, with a small field of view and mechanics able to be used in the environment of patients (a *dedicated clinical PET scanner*), can then be used to overcome the limits presented by other breast imaging modalities.

Positron emission mammography is the application of such a technology to breast imaging. PEM is not a recent technique, and it was first proposed in 1994 by Thompson et al. [Thompson94, Thompson95]. Preliminary studies, available since a few years, indicated how PEM can be better than MRI, mammography and ultrasounds at showing small tumours [Tafra07], and it may be also less likely to show non cancerous lesions than MRI [Weir05, Tafra07, Schilling08]. PEM showed to have better specificity, that is of great importance especially for women under the age of 30, for which the incidence of breast cancer is rare [Baum97]. The high-resolution can also help tailoring breast-surgical procedures, thus mitigating the effects of lumpectomy in the quality of life after therapy.

Unfortunately, only two PEM systems have reached the clinical test stage so far, the PEM-I scanner proposed by Thompson [Tafra05, Thompson06] and the Naviscan PEM Flex scanner [MacDonald09a] which actually is likely an evolution of the PEM-I [Thompson06]. This fact has the implication that a clinical-level comparison cannot be done between all existent PEM scanners, which would be interesting for example to determine which is the most efficient detector geometry. As long as the geometry remains analogue, it is easy to understand that better detector performances or faster acquisition systems should entail better diagnostics. The same cannot be said in the case we have a ring or a rectangular box array of detectors. Perhaps the lack of any clinical comparison is also one of the reasons of the absence of camera testing standards, such as NEMA (National Electrical Manufacturers Association, U.S.A.) standards for small animals, which in turn makes the classification of the state of the technique a bit more difficult.

2.1.3 Hadrontherapy treatment

Whilst cancer control programs in developing world contemplate many competing priorities, such as cancer screening, early detection, prevention and palliative care, this does not detract from the requirement to treat patients who present with established cancer. The therapeutic mainstays of cancer today are surgery, chemotherapy and radiotherapy, being the relative contribution of each mandated by the natural history of the specific tumour. For each of them, molecular imaging has proved to be helpful in the treatment outcome. Image guided surgical interventions, PET cancer surveillance in chemotherapy and proton therapy, are foreseen as the future of cancer treatment in the last Cancer Report of the World Health Organization [Boyle08].

Among these, proton therapy, which is the main form of hadrontherapy, is seen as an incoming major breakthrough in the field of radiotherapy, the technique that, in all its forms, already accounts for the treatment of more than the 50% of patients affected by cancer.

This new technique, that employs light nuclei beams of medium energy[1] instead of X-rays as in conventional radiotherapy, may overcome several of the limits of the latter thanks to a more localized in depth and transversally energy deposit and a higher relative biological effectiveness. However, the higher physical selectivity of ion therapy demands higher precision in the monitoring of the applied treatment, especially if the target volume is located close to critical organs and a fractioned therapy is applied. In fact, minimal inaccuracies in the positioning of the patient or local anatomical changes, with respect to the information of the therapy planning X-ray CT may produce unpredictable ions range deviations and consequently dramatic spatial changes of the planned dose. For these reasons, in vivo information on the range of ions are desirable, but the complete stopping of the ions

---

[1] Few hundreds of MeV

in patient prevents the application of electronic portal imaging methods as used in conventional radiotherapy. All the ions used in hadrontherapy, protons included, induce in the biologic material nuclear reactions which led to the production of β^+ emitters, i.e. mainly ^{15}O and ^{11}C from their correspondent stable isotopes. By using other ions like carbon or oxygen, through the fragmentation of beam ions themselves there is an additional production of other β^+ emitters. The induced activity can be measured with the so-called *in beam PET* to extract in-vivo information about the effective ion path and stopping point. Through the comparison with the foreseen activity, evaluated from the dose profile stated by the treatment plan, a qualitative indication of discrepancies from the planned dose can be extracted.

The positive clinical impact of in-beam PET has been already demonstrated at GSI (Centre for Heavy Ion Research, Darmstadt, Germany) in case of ^{12}C irradiation by using a commercial PET scanner adapted to the purpose [Parodi08a]. The next goal is then to demonstrate the positive clinical impact for the use of a dedicated PET system for the Bragg's peak localization in case of hadrontherapy with proton beams. A feasibility study is in progress in the FIIG of Pisa and other divisions of INFN, for verifying the applicability of an in beam PET for indirect extrapolation of radiation range in tissues, in the field of proton therapy. The DoPET (Dosimetry PET) project is the framework in which this study is being developed.

2.1.4 In-beam PET monitoring

Differently from X-ray radiotherapy, in which the incident beam is made of high energy photons, hadron beams offer a much higher target depth control, thanks to the effect of the Bragg peak [Munzenrider99]. In-beam PET monitoring is a technique that is expected to boost hadrontherapy efficiency. This can be accomplished thanks to the direct feedback control path on the incident beam provided by a HR PET scanner [Parodi07b,Parodi07a,Parodi08b]. Currently there are in literature only two examples of dedicated acquisition setups. The first is based on BASTEI detectors, mounted on a whole-body PET system and synchronized with a pulsing hadron beam [Crespo06]. The second is DoPET, the first dedicated imaging prototype which consists of two planar detector heads, each made up of 21 × 21 lutetium-yttrium oxyorthosilicate (LYSO) square crystals (2 mm size, 2.15 mm pitch) and coupled to one squared multi-anode Hamamatsu H8500 PMT (Photomultiplier) [Vecchio09]. A comprehensive analysis of both systems can be found in [Attanasi09]. The main difference between the two systems is that only DoPET is equipped with specialized detectors, while the BASTEI prototype was experimented with a system completely designed for different applications. However, also the

DoPET scanner borrowed (with some minor modification) acquisition electronics from the YAP-PET scanner, specialized for small animal imaging. At the current state, DoPET is capable of acquiring images with resolutions of 1.7 mm axial and 7 mm transversal [Attanasi09]. Next years research will be based on semi-analytical radioisotopes unfolding, based on the distribution of acquired events on time, and enhancing system performance by increasing detectors area and reducing dead time. It will also be studied the possibility of keeping the acquisition running with the hadron beam turned on, which is a condition that requires extremely low dead times in order not to saturate the system. The strategy adopted to reduce dead time has been to parallelize acquisition electronics into detector modules, so that when an event is acquired, the processing and front-end dead time affects only a fraction of the whole detector area. This would lead to relatively large planar detectors (15 cm × 15 cm) and therefore to a system very similar to the PEM scanner we want to realize. The detectors arrangement and the specific front-end electronics proposed for this new DoPET2 are well suitable also for PEM imaging, and for this reason we decided to share the same hardware for both projects.

2.2 Physical principles of PET imaging

Positron emission tomography (PET) is based on the characteristics of radionuclides that decay by positron emission. These radionuclides are produced in a cyclotron and are then used to label compounds of biological interest. The labeled compound (typically $10^{13} - 10^{15}$ labeled molecules) is introduced into the body, usually by intravenous injection, and is distributed in tissues in a manner determined by its biochemical pathways. When the radioactive atom on a particular molecule decays, a positron is ejected from the nucleus, ultimately leading to the emission of high-energy photons that have a good probability of escaping from the body. A PET scanner consists of a set of detectors that surround the object to be imaged and are designed to convert these high-energy photons into an electrical signal that can be fed to subsequent electronics. In a typical PET scan, 10^6 to 10^9 decays will be detected. These events are corrected for a number of factors and then reconstructed into a tomographic image using mathematical algorithms. The output of the reconstruction process is a three-dimensional image volume, where the signal intensity in any particular image voxel is proportional to the amount of radionuclide (and, hence, the amount of labeled molecules to which it is attached) in that voxel. Thus, PET images allow the spatial distribution of radiolabeled tracers to be mapped quantitatively in a living human. By taking a time sequence of images, the tissue concentration of the radiolabeled molecules as a function of time is measured, and with appropriate mathematical modeling, the rate of specific biological processes can be determined.

2.2.1 The annihilation process

If a nucleus has either an excess of protons or neutrons, it is unstable and prone to radioactive decay, leading to a change in the number of protons or neutrons in the nucleus and a more stable configuration.

Nuclei that decay in this manner are known as radionuclides. For a specific element with atomic number Z, isotopes that are unstable and which undergo radioactive decay are known as radioisotopes of that element. One common method by which nuclei with an excess of protons may decay is through positron emission (also known as β^+ decay). Essentially, a proton in the nucleus of the atom is converted into a neutron (n) and a positron (e^+). The positron is the antiparticle to the electron with the same mass but opposite electric charge. The positron is ejected from the nucleus, along with a neutrino (ν) that is not detected. An example of a radionuclide that decays by positron emission is ^{18}F:

$$^{18}F \rightarrow ^{18}O + \beta^+ + \nu \tag{2.4}$$

The net energy released during positron emission is shared between the daughter nucleus, the positron, and the neutrino. Positrons are therefore emitted with a range of energies which rapidly loose in inelastic interactions with atomic electrons in the tissue. Once most of positron energy is dissipated, it will combine with an electron and form a hydrogen-like state known as *positronium.* In the analogy to hydrogen, the proton that forms the nucleus in a hydrogen atom is substituted by a positron. This state lasts only about 10^{-10} seconds before a process known as annihilation occurs, where the mass of the electron and the positron is converted into electromagnetic energy. Because the positron and electron are almost at rest when this occurs, the energy released comes largely from the mass of the particles and can be computed from Einstein's mass-energy equivalence as:

$$E = mc^2 = m_e c^2 + m_p c^2 \tag{2.5}$$

Where m_e is the mass of the electron, m_p is the mass of the positron, and c is the speed of light. Inserting the constant values for each quantity, the energy released can be shown to be 1.022 MeV. The energy is released in the form of high-energy photons. As the positron and electron are almost at rest

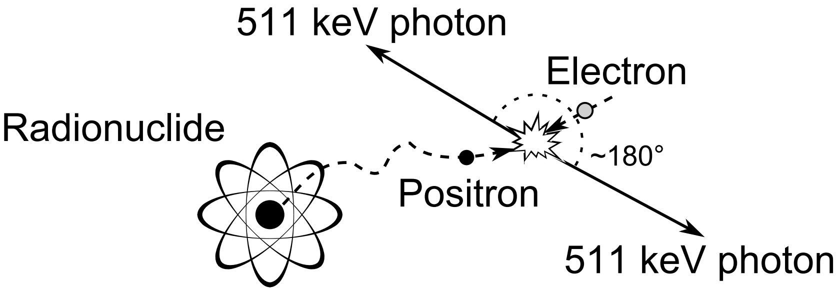

Figure 2.1: The annihilation process.

when the annihilation occurs, the net momentum is close to zero. Because momentum as well as energy must be conserved, it is not in general possible for annihilation to result in the emission of a single photon; otherwise, a net momentum would occur in the direction of that photon. Instead, two photons are emitted simultaneously in opposite directions (180° apart), carrying an energy equal to 1.022 MeV/2, or 511 keV, ensuring that both energy and momentum are conserved. This process is shown schematically in Figure 2.1. The annihilation process has a number of very important properties that are advantageous for imaging and lead directly to the concept of PET. First, the annihilation photons are very energetic (they fall in the gamma-ray region of the electromagnetic spectrum and are roughly a factor of ten higher in energy than diagnostic x-rays), which means they have a good chance of escaping the body for external detection.

The precise geometric relationship with which the two photons are emitted, and eventually detected, is the key that allows us to reconstruct positron annihilation points, and therefore estimate radiotracers distribution in the imaged subject. Indeed, the annihilation process forms the basis for PET imaging. A PET scanner is designed to detect and localize the simultaneous back-to-back annihilation photons that are emitted following decay of a radionuclide by positron emission. The line joining the two photons is the raw data that is fed to the reconstruction algorithm and is usually referred to as the *line of response* or shortly *LOR*.

2.2.2 Radiation detectors

In order to detect annihilation radiation, a set of two or more high-energy photon detectors must be used. To obtain the best quality image for a given injected dose of radioactivity, the detectors must have a high *efficiency* at 511 keV and must also give precise information on the spatial location of the interaction. The latter is generally achieved in one of two ways, either by using arrays of small detector elements, in which case the precision of localization is related to the size of the detector element, or by using a larger area detector that has position-sensing capability built in.

It is also important to be able to determine when a photon struck the detectors, so that the time of all detected events can be compared to determine which ones arrived closely enough in time to correspond to an annihilation pair. The ability of a pair of detectors to determine the time difference in arrival of the annihilation photons is known as the *timing resolution* and is typically on the order of few nanoseconds.

A typical timing window that is used in PET scanners so as not to accidentally reject annihilation photon pairs is typically 2 to 3 times the timing resolution, leading to values typically between 4 and 20 ns. Finally, the detectors should indicate the energy of the incoming annihilation photon such that those that have scattered and therefore altered their geometrical properties can be rejected. The ability of the detector to determine the energy of the photon is known as the *energy resolution*.

Scintillation detectors are widely used gamma-ray detectors that form the basis for almost all PET scanners in use today. These detectors consist of a dense crystalline scintillator material that serves as an interacting medium for gamma rays and high-energy photons and which emits visible light when energy is deposited inside them. This light is then subsequently detected and amplified by a photon detector, usually a PMT and converted into an electrical current.

The amount and rising instant of the generated current are typically the quantities that bear the information on both energy and timing of received photons. Position sensitive photomultipliers (PS-PMT) can distribute the current to an array of anodes according to the position of the light spot. The position acquisition is therefore performed by retrieving such a distribution.

Given the relatively high number of signals to process, a common approach is to use a resistive network that can encode the set of currents into four voltages. The most common is the Anger network in which the photon energy is proportional to the sum of the four output voltages and its impact position can be derived from the relationships between each one of the four values. The line of response is then usually derived from photon positions in post processing, contextually with the reconstruction process.

2.2.3 Tomographic reconstruction and imaging data structures

The goal of image reconstruction is to provide quantitatively accurate cross-sectional images of the distribution of positron-emitting radiopharmaceuticals in the object that is being scanned, using the externally detected radiation with the mathematical algorithms of computed tomography. This essentially allows us to see "inside" the body in a completely non-invasive fashion. The reconstruction step is necessary because the raw PET data only defines the location of the emitting atom along a line across the object, the line of response. To reconstruct tomographic images also requires that data from the object be adequately sampled. A PET scan consists of the detection of a large number of pairs of annihilation photons. During the course of the PET scan, the total number of counts measured by a particular detector pair will be proportional to the integrated radioactivity along the line joining the two detectors. This data are commonly referred to as line integral data and the process of photon pairing and line detection is referred to as *collimation*, which will be covered in Section 2.4.2.

The role of image reconstruction is to convert the line integrals measured at many different angles around the object into a set of 2D images that reflect the distribution of positron-emitting atoms (and, therefore, the molecule to which it is attached) in slices orthogonal to the detector plane.

There are two basic approaches to image reconstruction. One approach is analytic in nature and utilizes the mathematics of computed tomography that relates line integral measurements to the activity distribution in the object. These algorithms have a variety of names, including filtered backprojection, which makes use of Radon's transform theory, and Fourier reconstruction. The second approach is to use iterative methods that model the data collection process in a PET scanner and attempt, in a series of successive iterations, to find the image that is most consistent (using appropriate criteria) with the measured data.

Line integrals are commonly stored in specific 2D arrays whose coordinates are the rotation angle around the object and the coronal offset with respect to a reference detector position. This coordinate system is particularly efficient in the case of cylindrical multiring scanners, and the 2D space it determines is defined as the Radon's domain. Because of the particular geometrical relationship between the imaged object and its representation in Radon's domain, a punctual radiation source converts into a sinusoid in the line integral array, which therefore takes the name of *sinogram*. In Figure 2.2 is illustrated a simple example of an object in the spatial domain and its corresponding sinogram.

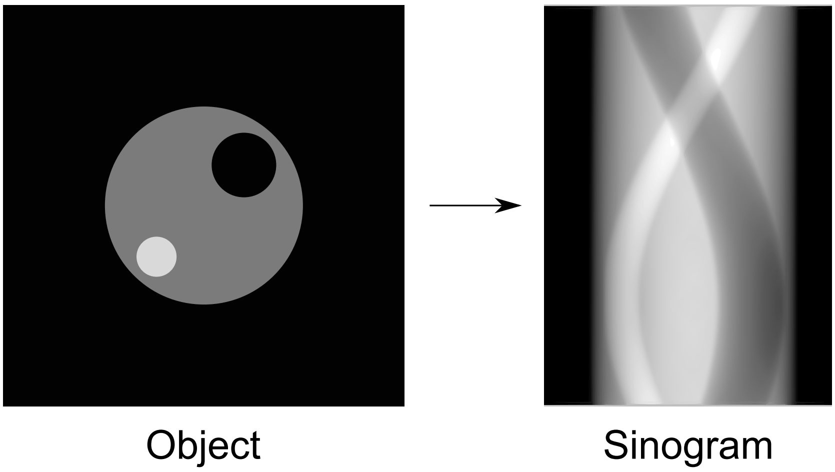

Figure 2.2: A simple object and the sinogram (simulation) that would result from taking projection views over 180° around this object. (Data courtesy of Dr. Juan Enrique Ortuño-Fisac.)

By feeding a sinogram to a reconstruction algorithm it is possible to perform two-dimensional reconstruction of a two-dimensional image. A set of parallel sinograms, obtained for example by a set of parallel detector rings, can be also used to perform two-dimensional reconstruction of a three-dimensional image. A more complex approach would be to acquire also cross-ring lines of response, thus giving cross-plane sinograms, which are usually stored in data structures called *michelograms*. These data structures are therefore an extension of sinograms that enable three-dimensional reconstruction of three-dimensional images, which is a technique orders of magnitude more sensitive than two-dimensional reconstruction.

When the PET scanner is equipped with parallel flat-panel detectors, instead of ring ones, a more efficient approach is to use *planograms*, which are the three-dimensional extension of *linograms*. Planograms are 4D arrays whose coordinates are the discrete spatial coordinate of both scintillator pixels hit by the annihilation photon pair. As in sinograms, each point of the planogram represents a line integral across the imaged object.

2.3 Theoretical limitations of PET

The physical and statistical effects involved in PET impose a series of *fundamental limits* in three major imaging aspects: spatial resolution, noise and sensitivity. The main limiting factors for spatial resolution are summarized in Figure 2.3.

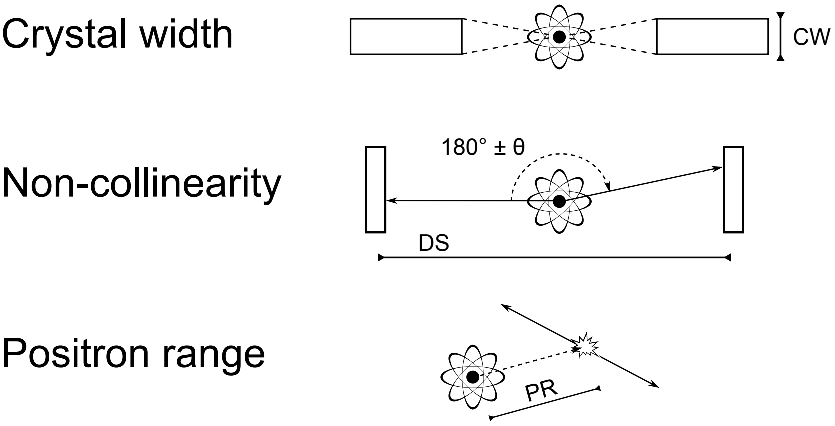

Figure 2.3: Main limiting factors for spatial resolution.

Another limiting factor is the pixel depth, which introduces parallax error. The theoretical spatial resolution achievable with PET can be calculated as [Thompson06]:

$$R * \sqrt{PR^2 + (0.0044 * DS)^2 + (CW/2)^2 + (BE)^2} \tag{2.6}$$

Where R is a factor that relates to the reconstruction method and filter and its commonly accepted value is 1.25 [Moses93], PR is the effective positron range in tissue $0.005 = 1/2 * tan(\theta/2)$, θ is the mean angle of non-collinearity, DS is the detector separation, CW is the crystal width, and BE combines the effects of other blurring effects. The resolution in equation 2.6 is defined assuming *infinite statistics*, i.e. it does not include effects from noise.

Noise characteristics have important implications for quantitation and detection performance in PET imaging, especially in high-resolution scanners. A high signal to noise ratio S/N should be expected in PET images, given that used emitters are highly localized and structured in the patient's body [Dahlbom87]. Attenuation corrections and low sensitivity can increase background noise thus severely reducing the S/N. This kind of noise can be compensated by means of background subtraction. However, statistical noise due to scattered photons and random coincidences still remains. The *Noise equivalent count rate* ($NECR$) is the figure of merit that quantifies the amount of background and statistical noise characteristic of a given PET scanner. The formulation of NECR is as follows:

$$NECR = \frac{T^2}{T + S + 2R} \tag{2.7}$$

Where T is the ratio of true coincidences, S the ratio of scattered photons and R the random coincidences. Assimilating the 2.7 to the S/N, T represents the signal, while scatters and randoms represent the noise. The image quality increases with NECR, as well as the sensitivity. In order to calculate the NECR the imaged object must be defined, and it is for this reason that NECR comparisons between different systems can be done only after a rigorous normalized characterization, usually following the latest NEMA standard.

The benefit in determining which are the fundamental limits of PET comes from the identification of their direct correlation with respect to some key system design parameters. We can assume that it would be hard to reduce the positron range (although in PET/MRI integrated scanners it would be possible) and pixels width strictly depends on the used crystal structure. However, it is evident that we have more chances in reducing detectors separation, if we accept to specialize the PET system for the imaging of a small organ, as we do for PEM or ibPET. Moreover, the count rate statistics and the resulting S/N ratio can be tackled by improving the data acquisition technology.

In the following section we will survey the technological aspects of PET acquisition, in order to establish which are the causes for imaging degradation and how can we engineer the system in order to face and overcome the above mentioned limits.

2.4 Technological aspects of PET scanners

Dedicated PET systems have undergone dramatic changes since the first PET systems were designed in the mid 1970s. The first systems could produce images at a resolution of 1 cm to 2 cm, they were low-sensitive, single-slice, small-diameter systems, using heavily collimated NaI(Tl) detectors. State of the art, high-resolution systems now have an intrinsic resolution of 1 mm to 5 mm, sensitivity higher by orders of magnitude, and an axial coverage of 15 cm or greater, with a minimal amount of mechanical collimation. The design of the most widely distributed high-end PET systems is fundamentally the same. The detecting system is based on the block detector concept. Depending on the manufacturer and the particular model, the size of the individual detector elements vary. These high-end dedicated systems provide the user with the maximum flexibility in the type of PET studies that can be acquired. Since the early 1980s, the majority of dedicated PET systems have used Bismuth germanate (BGO) as the scintillation material. Although this material has excellent absorption properties, the relatively long scintillation

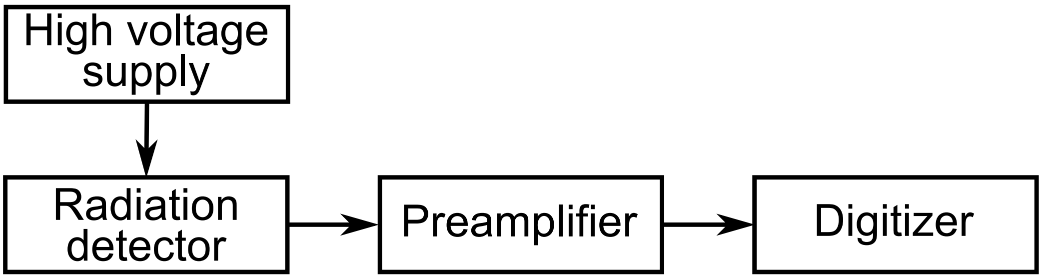

Figure 2.4: Schematic of front-end electronics

decay time limits the count rate performance, especially in the high counting-rate environment of 3D scans. Because of this limitation, the injected dose has to be reduced when operating a BGO in this 3D mode, which tends to offset the sensitivity gain. Recently, Lutetium-based crystals were introduced as the scintillation material. The speed of LSO/LYSO allows 3D scans to be acquired at the full injected dose, which provides an improvement in image quality and improved patient throughput. In the following sections we will survey the fundamental blocks that compose a modern PET scanner, as an instrument capable of recording the photon pairs produced by positron annihilation and impinged in the scintillating crystals.

2.4.1 Front-end electronics

Most of the radiation detectors used in nuclear medicine are operated in ”pulse mode”; that is, they generate pulses of electrical charge or current that are counted to determine the number of radiation events detected. In addition, by analysing the amplitude of pulses from the detector, it is possible with energy-sensitive detectors, such as scintillation, semiconductor detectors and proportional counters, to determine the energy of each radiation event detected. Selection of a narrow energy range for counting permits discrimination against events other than those of the energy of interest, such as scattered radiation and background radiation or the multiple emissions from a mixture of radionuclides.

Figure 2.4 shows in schematic form the basic electronic components of a nuclear radiation counting instrument. These components are present in systems ranging from the most simple counters to complex imaging instruments.

Most of common used radiation detectors produce signals of relatively small amplitude and high impedance. For this reason a *preamplifier* is required to bring the signal to an acceptable dynamic range and matched impedance to be digitized in the following stage. Digitization usually happens at two levels: the timing digitization and the energy digitization. The first consists in generating either a synchronous or asynchronous digital pulse that brings the information on the photon arrival time. This pulse will be used in the collimation stage to resolve coincident events from single ones. The energy digitization is usually implemented with a series of ADC channels connected either in charge, voltage or free running mode. The values converted by the ADCs are later processed to characterize the acquired event.

2.4.2 Electronic collimation

With collimation we refer to the process of defining the line, or tube, covered by the photon pair from the annihilation point to the two detectors. This line is the raw data that brings, through the reconstruction process, to the tomographic image. In PET, collimation is performed electronically by combining detected photons in pairs and deriving geometrically the line that joins the two hit points: hence the term electronic collimation [Semmler08], in contrast with mechanical collimation used in Single Photon Emission Computed Tomography (SPECT), where parallel photons are filtered by means of deep pinhole grids. Pairing is made by selecting events received within intervals of the order of nanoseconds: the pair becomes a single information unit that we call *coincidence*, which in this context represents the *signal*. The narrower the interval is, the higher is the probability that both paired photons belong to the same positron annihilation, i.e. that the pair did not derive from two uncorrelated, random events. We refer to those events as *randoms*, and we can think about them as our *noise*.

The coincidence detection is based on the timing information given by the front-end electronics. This information can be a pulse or a digital *timestamp*. In the first case, a combinational comparator resolves a coincidence when two pulses arrive at the same time. In the second case, coincidences are resolved by computing timestamp differences. The technological cost and performance of both techniques will be more clear after an overview of current HR-PET systems.

Under ideal circumstances, only true coincidences would be recorded, that is, only events where the two detected annihilation photons originate from the same radioactive decay and have not changed direction or lost any energy before being detected. However, due to limitations of the detectors used in PET and the possible interaction of the 511 keV photons in the body before they reach the detector, the coincidences measured are contaminated with undesirable events, which include random, scattered and multiple coincidences (Figure 2.5).

All these events have a degrading effect on the measurement and need to

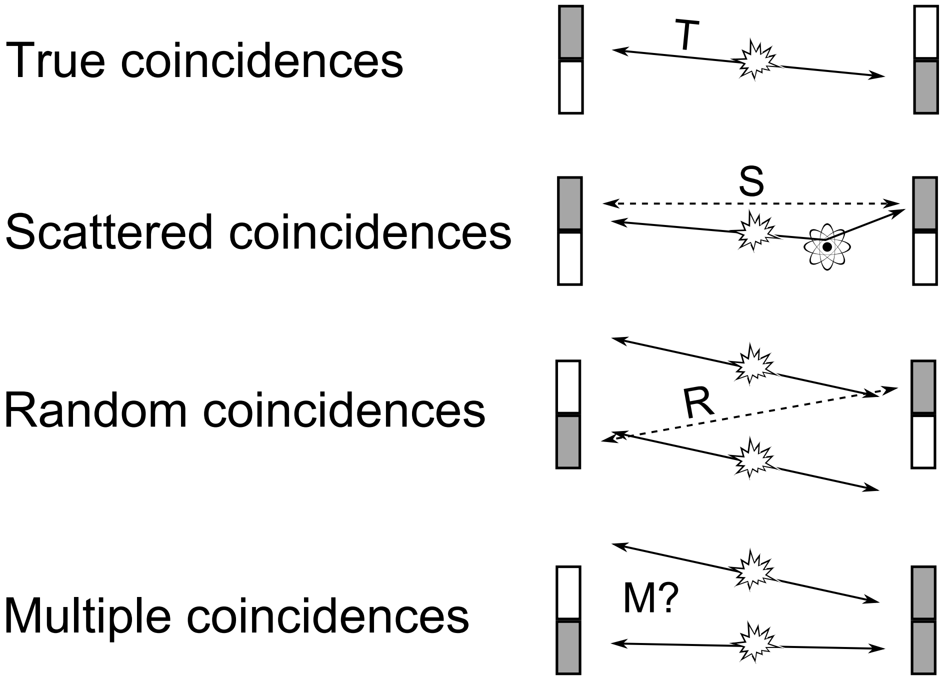

Figure 2.5: Accidental coincidences. T are the true coincidences, in which a gamma pair produced by positron annihilation is correctly detected. S are the scattered coincidences, in which the direction of one of the two photons is deviated, resulting in an incorrect line of response. R are random coincidences, i.e. those photons that are randomly detected at the same time, but belong to different annihilation processes. M are multiple coincidences, in which more than three photons are detected at the same time, thus preventing the possibility of deriving the valid photon pair.

be corrected to produce an image that represents as closely as possible the projection of true radioactivity concentration. Another point to consider is that the vast majority (typically 90% or more) of photons detected by the PET scanners are single events, in which only one of the two annihilation photons is registered. The partner photon may be on a trajectory such that either it does not intersect a detector (most PET scanners provide relatively modest solid angle coverage around the object), or the photon may not deposit sufficient energy in a detector to be detected or may not interact at all. These single events do not contribute to valid data, but they are responsible for random and multiple coincidence events. Given that they must still be processed by the electronics to see if they form part of a coincidence pair, they are the determining factor in issues related to detector dead time.

When positron annihilation occurs, the two 511 keV photons are emitted simultaneously. Therefore, the detectors should ideally respond simultaneously. Because of the finite time resolution of the detectors, signals must be accepted if they occur within a certain finite time interval or timing window. Because of the finite width of the timing window, it is possible that two unrelated single annihilation photons can be detected and registered as a valid coincidence. These unrelated events are referred to as accidental or *random* events. Because the random events are produced by photons emitted from unrelated isotope decays, they do not carry any spatial information about the activity distribution and produce an undesired background in the final images. If the individual photon detection rates (counts per second) in a pair of detectors are given by N_1 and N_2, then the rate of random coincidences, N_R (randoms per second) can be shown to be:

$$N_R = 2\tau N_1 N_2 \tag{2.8}$$

where τ is the width of the logic pulses produced when a photon is absorbed in the detector. The term 2τ is often referred to as the coincidence timing window. Because the individual detection rates N_1 and N_2 are directly proportional to the activity in the field of view of the scanner, the rate of random coincidences is proportional to the square of the activity in the field of view. The randoms rate is directly proportional to the coincidence timing window, which is why it is important not to make this any wider than required by the timing uncertainties in true coincidence events.

Scattered coincidences are another type of background event in need of correction. These events are in essence true coincidences, but one or both of the two annihilation photons has undergone a Compton scatter interaction and changed direction before they reach the detector pair. Using the coincidence detection technique, it is assumed that all detected coincidence events originate from an annihilation which, in turn, originates from a position anywhere on a line connecting the detector pairs. Because of the change in direction of the photon(s) in a scattered event, this is not true and the event is assigned to the incorrect LOR If not corrected, the scattered events produce a low spatial frequency background that reduces contrast. The distribution of scattered events depends on the distribution of the radioactivity and the shape of the scattering medium (i.e., the patient). As will be discussed later, this is probably the most difficult correction to perform in PET. The fraction of scattered events detected can range from 15% to well over 50% in typical PET studies, depending on the size of the object and the geometry and energy resolution of the PET scanner.

Although only two detectors are required to be activated within the coincidence time window to register a valid coincidence, at high count-rates it is possible that three or more detectors are involved. In this case, it becomes ambiguous where the event should be positioned. Because of this ambiguity, these multiple coincidences normally are discarded. However, they can contain information about the quantity and spatial location of positron emissions because these events are often composed of a true coincidence together with a single photon from an unrelated decay. In this situation, up to three possible LORs can intersect the field of view, only one of which will be correct. In some circumstances, it may be better to randomly select one of the possible LORs rather than completely discarding the event. A better solution, possible only with real time processing, would be to select the interesting LORs depending on their energy. The impact of random and multiple events is a topic that has been recently under study [Oliver08], although no determining evidences on the best acquisition policies have been found yet.

2.4.3 Data collection

The end point in most PET studies is to produce an image, from which diagnostic or quantitative parameters can be derived. These parameters can be as simple as a qualitative comparison of activity concentration in different tissue regions or more complex biologic parameters such as metabolic rate, receptor density, or levels of gene expression. The information that is to be extracted from the image will dictate how the PET data are collected. The most basic data acquisition protocol in PET is the collection of a single data set or static frame over a fixed length of time. The image reconstructed from such a data set represents the average tissue activity concentration during the acquisition. This is the typical acquisition mode used in studies where the tissue activity distribution remains relatively static during the collection of the data. An example where this acquisition mode is commonly used is for *fluorodeoxyglucose* (FDG) studies, where the tracer concentration remains fairly stable following an initial uptake period of 30 to 40 minutes. In these types of studies, the biologic parameter of interest (in this case the metabolic rate for glucose) is then assumed to be directly proportional to the measured activity concentration. For some radiotracers, it is necessary to follow the dynamic changes in concentration to extract a particular parameter of interest. In these studies, the data are collected as a sequence of dynamic time frames, where the PET images provide information about the changes in activity concentration distribution over time. This information represents the tissue response to the time course of the radiotracer in the plasma following intravenous injection. The tissue time-activity curve can then be processed with a statistical model to determine the parameters of interest. An example of this acquisition mode is the in-beam monitoring, in which the interesting quantities are the energy doses that must be derived from the acquired radioactivity.

During all the acquisition time the imaging system must be able to store events data and statistics, typically in a computer hard disk. Data can be streamed either with proprietary custom communication protocols, with standard Video Electronics Standards Association (VESA) based protocols or with commodity standards such as Peripheral Component Interconnect (PCI) and Universal Serial Bus (USB).

2.4.4 Problems in radiation detection

An important consideration for any radiation measurement instrument is its *detection efficiency.* Detection efficiency refers to the efficiency with which a radiation measuring instrument converts emissions from the radiation source into useful signals from the detector.

Maximum detection efficiency is desirable because one thus obtains maximum information with a minimum amount of radioactivity. Also important are the instrument's *counting rate limitations.* There are finite counting rate limits for all counting and imaging instruments used in nuclear medicine, above which inaccurate results are obtained because of data losses and other data distortions. Thus if a gamma ray emitting source of activity A emits η rays per disintegration, the emission rate ξ of that source is

$$\xi \left[\frac{\text{photons}}{\text{sec}}\right] = A\ [\text{Bq}] \times 1 \left[\frac{\text{decays}}{\text{sec} \cdot \text{Bq}}\right] \times \eta \left[\frac{\text{photons}}{\text{decays}}\right] \tag{2.9}$$

If the counting rate recorded from this source is R [Hz], then the detection efficiency D for the measuring system is

$$D = R/\xi \tag{2.10}$$

Alternatively, if the emission rate ξ and detection efficiency D are known, one can estimate the counting rate that will be recorded from the source from

$$R = D\xi \tag{2.11}$$

In general, it is desirable to have as large a detection efficiency as possible, so that a maximum counting rate can be obtained from a minimum amount of activity.

Detection efficiency is affected by several factors, including the following:

1. The geometric efficiency, which depends mostly on detectors size and positioning
2. The intrinsic detector efficiency, which depends mainly on absorbing material
3. The recording efficiency, i.e. the fraction of generated signals that are correctly recorded by the acquisition system
4. The absorption and scatter of radiation within the source itself

In theory, one therefore can describe the detection efficiency D as a product of individual factors:

$$D = g \times \varepsilon \times f \times F \tag{2.12}$$

Where g is the geometric efficiency, ε is the intrinsic efficiency, f is the recording efficiency and F is the factor of absorption and scatter occurring within the source.

Increasing detection efficiency is one of the major goals of the current thesis, as it will be described in the following sections. In doing so we will take as fixed value F and we will approach the design by using state of the art solution to maximize both geometric and intrinsic efficiencies. The major work will be then done to achieve the maximum recording efficiency while keeping the due flexibility in order to be able to *re-dedicate* the platform to different applications and still have the maximum values for both g and ε.

Another important limiting factor in PET imaging is *dead time*. Every radiation counting system exhibits a characteristic dead time or pulse resolving time τ that is related to the time required to process individual detected events. The pulses produced by a radiation detector have a finite time duration, such that if a second pulse occurs before the first has been processed, the two pulses will overlap to form a single distorted pulse. With common energy sensitive detectors, the overlap usually occurs in the pulse preamplifier causing baseline shift and pulse pile-up. Overlapped pulses may fall outside the acquisition window or may have amplitudes that are rejected by the processing machines thus resulting in a loss of valid events. Such losses are called *dead time losses*. The shorter the dead time, the smaller the dead time losses. Dead time losses can occur in different stages of the system, though the characteristic is often given for the system as a whole and coincides with the higher dead time in the acquisition pipeline.

2.4.5 Dead time mathematical models

The dead time is the time during which a counting system is busy processing an incoming event. Any counting system has a characteristic, finite dead time. These systems usually are classified as being paralysable or nonparalysable. A *nonparalysable system* is one for which, if an event occurs during the dead time τ of a preceding event, then the second event is simply ignored, with no effect on subsequently occurring events (Figure 2.6). Digital processors are typically nonparalysable. A *paralysable system* is one for which each event introduces a dead time τ whether or not that event actually was counted. Thus an event occurring during the dead time of a preceding event would not be counted but still would introduce its own dead time during which subsequent events could not be recorded. A paralysable system may be thought as one with an "extendable" dead time. Most radiation detectors behave as paralysable systems.

Because of dead time losses, the *observed* counting rate R_o [Hz] is less than the *true* counting rate R_t [Hz], where the latter is the counting rate that would be recorded if $\tau = 0$. The relationship among R_o, R_t and τ depends on the type of dead time [Evans55]. For nonparalysable systems,

$$R_o = R_t/(1 + R_t\tau) \tag{2.13}$$

$$R_t = R_o/(1 - R_o\tau) \tag{2.14}$$

If the system has a paralysable dead time, then

$$R_o = R_t e^{-R_t\tau} \tag{2.15}$$

There is no analytic equation for R_t as a function of R_o for the paralysable case. Figure 2.7 shows R_o versus R_t for the two types of systems.

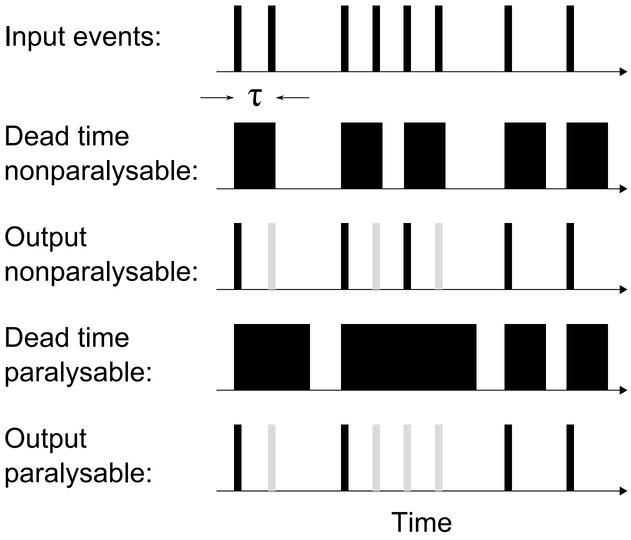

Figure 2.6: Difference in output signals between nonparalysable and paralysable systems, both with dead time τ. With a nonparalysable system, events are lost if they occur within a time τ of a preceding *recorded* event, whereas with a paralysable system events are lost if they occur within a time τ of *any* preceding event, regardless of whether that event has been recorded.

For a nonparalysable system, the observed counting rate increases asymptotically toward a maximum value

$$R_o^{max} = 1/\tau \tag{2.16}$$

At high count rates the system records one event per dead time interval.

For a paralysable system, the observed counting rate rises to a maximum value given by

$$R_o^{max} = 1/e\tau \tag{2.17}$$

and then *decreases* with a further increase in the counting rate. This is because additional events serve only to extend the dead time without contributing to the observed counting rate. At very high counting rates, the observed counting rate actually approaches zero. This is called *counter paralysis.*

Dead time losses are given by the difference between observed and true counting rates, $R_t - R_o$, and *percentage losses* are given by

$$\text{percentage losses} = [(R_t - R_o)/R_t] \times 100\% \tag{2.18}$$

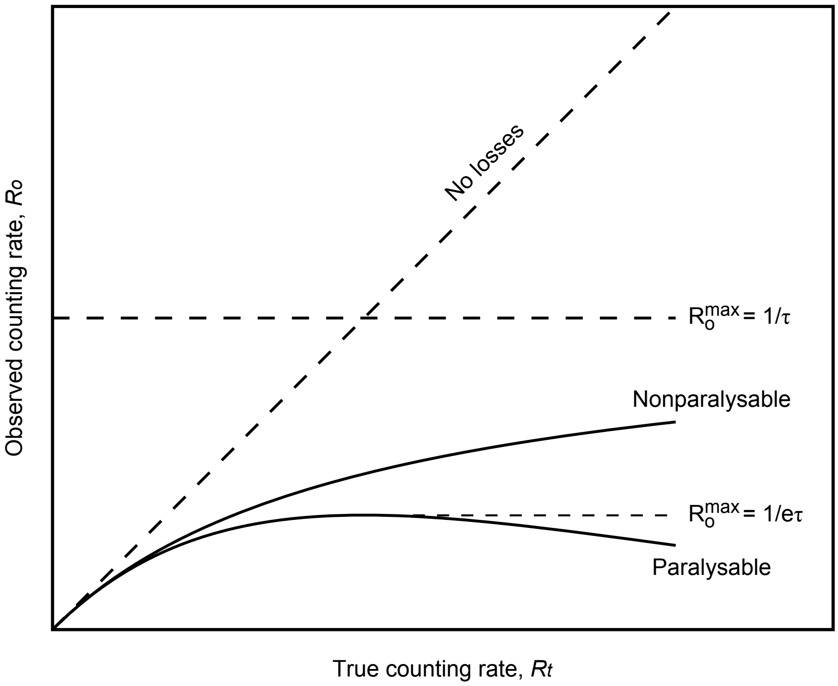

Figure 2.7: Observed (R_o) versus true (R_t) counting rate curves for paralysable and nonparalysable systems having the same dead time value, τ.

When the product $R_t\tau$ is small, the percentage losses can be described by the same equation for both paralysable and nonparalysable systems

$$\text{percentage losses} \approx (R_t\tau) \times 100\% \tag{2.19}$$

Many counting systems, such as nuclear medicine scanners, have multiple components in cascade, each with its own individual dead time. In some cases, one component of a cascaded system may be paralysable, e.g. the scintillation detector, whereas the other may be nonparalysable, e.g. the data acquisition board. In most cases one component dominates the system and its behaviour adequately describes the system behaviour. However, if cascaded paralysable and nonparalysable components have similar dead times, both components contribute to dead time losses and the behaviour is a hybrid of the two.

2.5 State of the art of PEM scanners

The first use of F-18 fluorodeoxyglucose- positron emission tomography (FDG-PET) for the study of breast cancer was reported in 1991 by Wahl et al. [Wahl91], and since then many other reports have been made [Adler93, Avril99].

Conventional PET scanners showed a limited spatial resolution compared with structural imaging modalities such as CT and MRI. Because the identification of small tumors leads to earlier diagnosis and treatment, much effort has gone into trying to improve the spatial resolution of PET.

The idea of a dedicated PET scanner for breast imaging was first proposed by Weinberg in 1993, in a US patent application [Weinberg93], and a successful proposal for a small business incentive for research (SBIR) grant from the US National Institutes of Health NIH

The first experiments to examine the concept were published in 1993 [Thompson94], and the name "positron emission mammography" PEM was coined to represent this technique.

The concept was to place two planar detectors capable of detecting the 511 keV annihilation photons in a conventional x-ray mammography unit.

The two detectors move out of the radiograph field for conventional mammography, and move back over and under the breast for the PEM acquisition [Thompson95], as illustrated in Figure 2.9. This concept predates PET-CT by several years [Bergman98], but the goal was very much the same as that of PET-CT as it has evolved today: to provide a coregistered anatomical and functional image in the same procedure with minimal movement of the patient.

An important finding of the first PEM work [Thompson94] was that a small hyperactive region was just as visible in a superposition of a few near vertical projections as it was in fully reconstructed tomographic images. The experiments were performed in a 15-slice brain scanner on a box phantom containing four tubes of various sizes with either no activity or 9.3 times the background. The images were made over different times, so that each consecutive image contains half the counts of the previous one. This paper provided the basic estimate of both the signal-to-noise ratio and count-rate that could be expected from a clinical PEM instrument.

Encouraged by these results, the group built and performed a preliminary clinical trail of an instrument known as "PEM-I". Because of the conclusion that back-projection images were sufficient to identify regions of higher-than-surrounding uptake, no sophisticated reconstruction techniques were applied, preferring to opt for an almost real-time image display of the PEM image. The goal was to perform the clinical trial using only 75 MBq (2 mCi) of

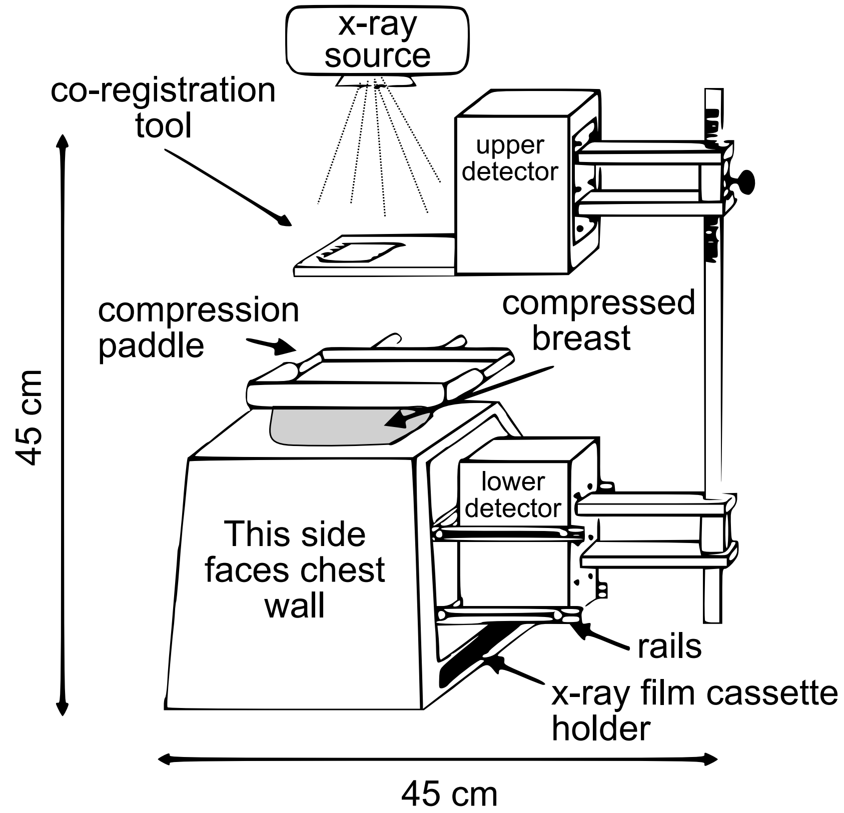

Figure 2.8: Layout of PEM-I breast imaging system. The two detectors, mounted on rails, are moved out of the radiographic field for conventional mammography, and back over and under the breast during the acquisition of a metabolic image [Thompson06].

FDG, and an imaging time of 2 minutes per breast, because this is about the time it takes to develop a radiograph film in an automatic film processor.

Today a certain number of similar instruments have been started. However, only one is commercially available, the Naviscan PEM Flex Solo II [Weinberg96b, Weinberg96a, Weinberg97, Raylman00, Weinberg02, Levine03, Weinberg04, Raylman05, Wollenweber04, Weinberg05b, Weinberg06a, Thompson06, Weinberg06b, Berg06, Luo08, Raylman08a, Raylman08b, MacDonald08], which has been developed, among others, by the same Weinberg that worked at the PEM-I project. A picture and the details of PEM Flex detectors geometry is shown in Figure 2.9. There are four scanners in a mature development stage: the YAP-PEM [Guerra02, Motta04, Belcari04, Motta05, Guerra06, Camarda06], ClearPEM [Lecoq02, Trindade03, Bento04, Santos04, Ribeiro04, Abreu05a, Varela05, Abreu05b, Leong06, Rodrigues07, Albuquerque09, Trummer09], DbPET/CT [Lamare05, Wu09, Bowen09] and MDA-PEM [Zhang08,

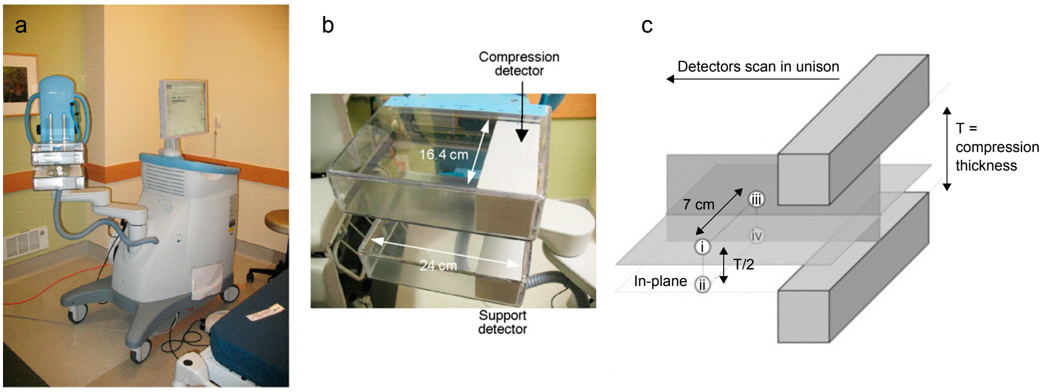

Figure 2.9: Images of the PEM Flex Solo II system [MacDonald09a]. (a) Picture of the scanner. (b) Close-up of detectors. (c) Illustration of in-planes and cross-planes. The markers i, ii, iii, and iv are the four cardinal positions within PEM Flex FOV used to investigate quantification consistency.

Ramirez09] scanners; other four had stopped to be investigated, either because the group switched target application or because the scanner went through so radical changes that the project evolved into a brand new one. These are the PEM-I [Thompson94,Thompson95,Robar97,Murthy97,Bergman98, Murthy99,Murthy00c,Murthy00b,Murthy00a,Zhang03,Thompson06], BPET [Freifelder95,Freifelder97,Freifelder01], maxPET [Cherry98,Doshi99,Doshi00b, Doshi00a, Doshi01] and LBNL-PEM [Moses01, Huber03, Wang04, Wang05, Moses06, Huber06, Wang06] scanners. Three very interesting PEM systems have been recently published, the C-PEM [Yamada07,Tonami07,Kitamura08b, Kitamura08a, Yamakawa08], which introduces a unprecedented C-shape geometry, the PEM-MRI [Maramraju08b,Maramraju08a,Ravindranath08] which pioneers PET-MRI integration in breast imaging, and the full ring MAMMI scanner [Martinez05]. There are also a few breast imaging experiments that are not treated here because of lack of information and generally poor public documentation up to now.

This situation shows an evident fact: dedicated breast and PEM systems are still globally in the early stages of development and implementation. Even with the presence of a commercially available system, no camera testing standards and system characterization procedures have been developed. In fact, in literature there are only few independent works that aim at making the way for the definition of a standardized dedicated breast PET evaluation [Luo08, MacDonald09b].

A comprehensive survey of development statuses and scanner properties is reported in Tables 3.1, 2.2, 2.3 and 2.4. Due to the lack of a standard characterization methodology, performance values cannot be normalized, and comparisons among different scanners should be done with care. Anyway, planar detector geometry shows to be the most used, and is the only one that produced clinical assessment, while rectangular and ring geometries were either abandoned or are still under early development. It must also be noted that curved geometries were always imported from a previous system, designed for other applications (whole-body or small animals) and adapted for breast imaging. As it can be seen, planar geometry is up to date the one that provides best spatial resolutions and sensitivities, independently from the detector technology, which instead tends to have more effect on energy resolution, and therefore on image contrast.

Name	Years	Institute	Status
PEM-I	’94-03	Montreal Neur.	Used for early clinical tests, stopped in 2000
PEM Flex	’94-09	NIH	Commercially available (State of the art)
BPET	’95-01	Unv. Pennsylv.	Characterized, stopped in 2001
maxPET	’98-01	UCLA	Characterized, stopped in 2001
LBNL-PEM	’01-06	LBNL	Characterized, stopped in 2006
YAP-PEM	’02-06	Univ. Pisa	Feasibility study, precursor of QPEM
ClearPEM	’02-09	CERN	Characterized, under development
DbPET/CT	’08-09	UC Davis	Partially characterized, under development
MDA PEM	’08-09	MDA	Partially characterized, under development
C PEM	’07-08	Shimadzu	Under development (from C-Shaped CT
PEM-MRI	’08-09	LBNL	Early prototype developed (from RatCAP)

Table 2.1: Status of current PEM systems development.

Name	Geometry	Detectors	Area cm^2	Pixel mm^2	DOI
PEM-I	Planar	BGO + PMT	103	2×2	No
PEM Flex	Planar	Transl. LYSO + PMT	$197 \div 787.2$	2×2	No
BPET	Split-ring	NaI(Tl) Slab + PMT	588	N/A	No
maxPET	Planar	LSO + PMT	364	2×2	No
LBNL-PEM	Rect. box	LSO + SiAPD + PMT	138	3×3	Yes
YAP-PEM	Planar	YAP:Ce + PMT	72	2×2	No
ClearPEM	Planar	LYSO:Ce + SiAPD	448	2×2	Yes
DbPET/CT	Planar	LSO + PMT	288	3×3	No
MDA PEM	Planar	LYSO + PMT	240	1.5×1.5	No
C PEM	C-Shape	LGSO + PMT	516	1.5×1.5	Yes
PEM-MRI	Ring	LSO + SiAPD	325	2×2	No

Table 2.2: Main specifications of current PEM systems.

Name	Sensitivity $Kcps/\mu Ci$	Spatial resolution mm	Energy resolution
PEM-I	1.1	2	53%
PEM Flex	5.9	2	N/D
BPET	0.123	3.8	10%
maxPET	14(*)	2.26	21.6%
LBNL-PEM	0.002	2	APD 24%, PMT 51%
YAP-PEM	N/D	5	19%
ClearPEM	2.4	2	13%
DbPET/CT	0.606	2.5	25%
MDA PEM	N/D	N/D	13%
PEM-MRI	N/D	N/D	18%

(*) System sensitivity for the maxPET scanner has not been published. The value here reported referes to the simulated sensitivity of a point source at the center of the field of view.

Table 2.3: Main performance characteristics of current PEM systems.

Another interesting comparison is related to the acquisition platforms. In order to do such a comparison it must be noted that a classification of acquisition systems is even harder than comparing system performances. This is because it seems that the hardware used is either custom built (and still in active development) or commercially available but with sub-optimal performance characteristics. Therefore is hard to find a common pattern among proposed alternatives. However, an attempt has been made in order to draw up a list of main characteristics, techniques and achieved performances, which are reporterd in table 2.4.

Name	Platform	Energy/Pixel	Max rate	Dead time
PEM-I	NIM-VME	Custom QDC + VAX	N/D	1000 ns
PEM Flex	cPCI crate	cPCI QDC	N/D	N/D
BPET	Philips CPET	QDC	3.8 MHz	240 ns
maxPET	NIM-VME	PCI-QDC	10 kHz	N/D
LBNL-PEM	Siemens HRRT	Free runn. ADC + FPGA	140 kHz	750 ns
YAP-PEM	NIM/YAP-PET	Custom QDC + PC	50 kHz	700 ns
ClearPEM	ClearPET	Free runn. ADC + FPGA	670 kHz	100 ns
DbPET/CT	maxPET	PCI-QDC	250 kHz	3600 ns
MDA-PEM	MDA-PET	Custom board QDC	2 MHz	22 ns
PEM-MRI	VME + FPGA	Within ASIC	262 kHz	N/D

Table 2.4: Acquisition platform of current PEM systems.

From the tables above emerges an interesting situation: even if custom hardware have been developed for energy characterization, the only PEM scanner that owns a fully dedicated acquisition system is the PEM Flex. The most common acquisition platform is the *Versa Module Europa* VME equipped with a set of *Nuclear Instrumentation Modules* NIM This equipment is widely used in physics research and very reliable and expensive. However, due to its general purpose target, it hardly can cope with acquisition requirements and often it must be coupled with custom built hardware. The other altenative has been to import existing acquisition hardware from different purpose PET scanners, such as whole-body Philips CPET, Siemens HRRT, MDA PET, or small animal ring scanners, such as ClearPET and YAP-PET. In this case performance is excellent, but the cost is high and the platform tends to be less flexible.

These considerations highlight another problem in PET imaging: there are no flexible, high-performance, scalable readout systems capable of handling detectors in both different geometries and detector technologies. Although this concerns mainly small research laboratories, that cannot afford expensive WB-PET systems for research in detectors materials and geometries, it is a widely sensed problem in the scientific community. As a result in 2009 the *OpenPET* project has been jointly promoted by the Lawrence Berkeley National Laboratory and SensL [Chaudhari10], in order to provide the scientists with such a demanded tool.

As it will be described in next chapter, our purpose will be to tackle this deficiency, specifically for clinical applications.

2.6 State of the art of in-beam monitoring

Apart from the isolated pioneering and very preliminary work of [Bennett78], the possibility of proton therapy monitoring by means of PET was recently investigated by various groups [Litzenberg92, Oelfke96, Paans92, Vynckier93] in off-line experiments, where the irradiated objects had to be transported to remote PET scanners. Due to the practical limitations coming from the off-line approach, no definitive conclusion on the clinical usefulness of the method was drawn. The first attempts at operating an in-beam positron tomograph at the Lawrence Berkeley National Laboratory had to be abandoned due to detector activation arising most probably from the flux of secondary particles caused by passive beam shaping techniques [Llacer88]. This situation made the in-beam PET scanner integrated into the treatment facility at GSI Darmstadt [Enghardt99] the first functional tool for the on-line investigation of the β^+ activation induced by hadron irradiation. The tomograph was named *Beta Activity Measurements at the Therapy with Energetic Ions*, shortly *BASTEI*, and in the last years it provided the researchers with a huge amount of data on β^+ activation during hadron impinging and its correlation with dose[2] distribution in the patient. First of all it demonstrated the neat superiority of PET imaging with respect to other imaging modalities [Müller06, Crespo06]: it provides three-dimensional capabilities, which are necessary to locate the delivery Bragg peak and are not supported by common beam portal techniques [Kramer00] used in radiotherapy, and it does not require additional radiation to be inflicted to healthy tissues as in x-ray beam delivery systems [Jaffray02]. Secondly, it demonstrated in the practice what had been only hypothesized, i.e. that the β^+ radioactivity distribution was of the same strength of common PET scenarios and that it would be related univocally with the dose distribution [Parodi02, Enghardt04, Müller06].

Using the BASTEI scanner some new problems were also addressed. During the experiments two different geometrical layouts where used: the full ring detector asset and the dual head asset. Being the dual asset a subset of the full ring from which a series of detectors where removed. Both using the same acquisition platform, a custom adapted system derived from parts of an ECAT EXACT tomograph (CTI PET Systems Inc, Knoxville U.S.A.) and complemented with VESA NIM modules [Pawelke96, Parodi05]. A comparison of obtained results [Crespo06] showed how the full ring approach provided better images although with awkward mechanical constraints on the maximum widths of both the patient's bed and the detector ring. This was because the ring had to be turned of 45° with respect to the bed in order to not to obstruct the beam [Pawelke96]. The main disadvantage of the dual head configuration was the strict need of precise alignment the beam irradiation spot and the isocentre of the field of view (FOV) of the PET scanner. In fact, major losses in image quality where at the borders of the FOV.

This led to the decision of adopting a full ring scanner for in-beam monitoring at GSI, eventually adopting new avalanche photodiode detectors (APD) technology to make the ring more compact [Crespo06]. Curiously, the cited technology comes from a PEM scanner.

At this point, it should be noted that the comparison presented in [Crespo06] cannot be taken as a comparison between ring scanners and dual head scanners. Indeed the dual scanner in question is the same ring version deprived of part of its detector elements. It is then obvious that the acquired image would result worse and the point of the paper is more related to the convenience of removing some detectors in favour of mechanical advantages, and the answer was negative.

However, the belief that a dual planar PET scanner, specifically developed for in-beam monitoring could have outperformed the current unique scanner

---

[2] In radiotherapy the dose is the energy deposited by incident photons per mass unit

used for such purpose led to development of the DoPET scanner at FIIG. Here again, the idea was to adapt the electronics previously developed for the YAP(S)-PEM scanner to a dual planar PS-PMT/LYSO based detector assembly [Vecchio08, Vecchio09].

A comprehensive and very interesting comparative study on both DoPET and BASTEI scanners, in its dual head form, has been done [Attanasi09]. The results of this study are the main reason for the interest in using, one more time, the PEM system developed in this thesis, for in-beam monitoring.

In fact, the main conclusion was that dual head geometry was applicable, and detection efficiency could be boosted if DoPET detectors were enlarged, the acquisition system were customized for beam gating and able to record the short heavy bursts of ^{15}O generated radioactivity in the first tens of seconds after each beam spill [Attanasi09].

2.7 Discussion

From the previous sections it appears to be clear that there is space for research on new and better digital acquisition systems. However, it is worth pointing out some additional considerations on the current state of the art of electronic collimation, because of its important role in PET imaging, its tight integration with acquisition systems and its implications in scanners design.

Coincidences detection is usually the most sophisticated task of the whole acquisition process, and the one to which is dedicated most expensive and cutting edge hardware. This because of the tight timing constraints and the high complexity required to monitor in real-time each possible detector combination. Part of PET technology literature is committed to the research of new coincidence detection techniques, with the two main aims of reducing complexity and improving timing resolution [Wang02, Nakhostin09, Joly09, Park08]. Better timing resolution is researched in order to enhance image S/N ratio and NEC [3] rates. Sub-nanosecond timing resolutions have been showed to enable also time-of-flight (TOF) information, thus improving trans-axial spatial resolution [Karp08]. Lower complexity would allow instead more detectors, therefore a higher solid angle of view and higher sensitivity.

Table 2.5 shows the coincidence techniques and properties of discussed PEM scanners, together with some other clinical and preclinical PET systems.

---

[3] The Noise Equivalent Count rate is a factor that is used to estimate image noise. At high count rates it is limited by the random counts rates.

Name	Technique	Resolution	Independent Detectors
Dedicated breast PET scanners			
PEM-I	AND-gating	12 ns	2
PEM Flex	AND-gating	N/D	2
BPET	Sum threshold	8 ns	2
maxPET	AND-gating	8.1 ns	2
LBNL-PEM	TDC	6 ns	4
YAP-PEM	AND-gating	14 ns	2
ClearPEM	FPGA-TDC	16 ns	4
DbPET/CT	AND-gating	22.2 ns	2
MDA PEM	TDC	9 ns	2
PEM-MRI	FPGA-TDC	13.87 ns	12
Preclinical PET scanners			
RatCAP	FPGA-TDC	17.96 ns	12
MicroPET-II	TDC	6 ns	90
YAP-PET	AND-gating	14 ns	4 (*)
Clinical PET scanners			
HRRT	AND-gating	6 ns	8 (*)
MDA PET	AND-gating	12 ns	12 (*)
GE Discovery	AND-gating	12 ns	21288 (*)

(*) Parallel AND-gating networks are applied to different detector subsets. Not all detector combinations can be resolved.

Table 2.5: Coincidence properties for breast, preclinical and clinical PET scanners.

Current coincidence processors are mainly based on two different approaches: AND-gating and Time-to-Digital conversion (TDC). In AND-gating, for each received photon a digital pulse is generated, with a well-timed rising edge and fixed width W. Pulses from all detectors are fed to a combinatorial circuit that generates a coincidence trigger when two of them overlap. With this technique, two photons can be distinguished (resolved) if they are separated in time by $2W$. This value is what we refer to as *coincidence resolution*. The main advantage of AND-gating is its relatively simple architecture (which is purely combinatorial), and the availability of a prompt trigger that allows to acquire coincident events and skip single ones. With slight modifications, the same technique can be used to estimate also random counts [Brasse05]. Its main disadvantage is that it scales badly, being the combining complexity of the order of $O(n^2)$, where n is the number of detectors. This bad scalability has been overtaken in the past by grouping detectors in subsets and resolving coincidences only between n selected subsets. Another disadvantage is that it is difficult to imagine an AND-gating network with sub-nanosecond timing features, because of the limits of current silicon logic families.

TDC based processors are more recent and much more complex [Damiani02, Swann04, Conti05, McElroy05]. They consist in labeling each single event with a *timestamp*, either by sampling a digital timing signal or interpolating the analog energy pulse. Coincidence detection is then made by calculating time differences, and the obtained coincidence resolution is the same of the Time-to-Digital converter. Time conversion can be performed in parallel for each detector, and coincidence processing can be also performed off-line. This greatly improves scalability. Moreover, digital data processing can be used to improve timing resolution beyond the intrinsic hardware limits. However TDC techniques require very low skew clocking networks, a synchronization protocol, but most of all need the acquisition of all events, including single ones [Bento04, Park08]. Given that single events are usually more than coincident ones by two orders of magnitude, this requirement converts into dramatically higher storage and bandwidth demands, which in turn increase the system cost.

2.8 Conclusion

Detectors technology for both PET breast imaging or in-beam PET monitoring is mature. However, it can be perceived that there exists room for contributing in the field by working on a dedicated as well as flexible acquisition system, in order to exploit the promising features of such techniques. The need of a dedicated acquisition system is evident comparing existing systems, it has been expressed by Huber et al [Huber06], in a retrospective on their LBNL-PEM scanner at the end of the project life, but also it becomes essential in order to realize the detectors configuration proposed for DoPET2. Moreover electronic collimation, which represents a fundamental limit for the number of detectors, is still a challenging task that has not reached yet an optimal status in terms of flexibility, performance and cost.

Chapter 3

A new efficient and flexible PET acquisition system: the QPEM scanner

3.1 Conceptual proposal prior to this thesis

First studies aimed at the achievement of an improved dedicated PET scanner, produced a proposal for a brand new PET architecture, capable of acquiring data from two detector plates, each composed of four independent detector modules [Franchi08c]. Because of the quadruple module configuration, the system was called *QPEM*.

These studies and the QPEM proposal represent the starting point for this thesis. Being preliminary, a number of questioning points were still left unanswered as well as the overall feasibility. It has been part of this thesis to address these questions and to provide alternative solutions.

A schematic view of the original QPEM proposal is illustrated in Figure 3.1: in the architecture we can identify five main component blocks:

- The data streaming interface (USBIF)
- The Data Acquistion (DAQ) modules
- The Constant Fraction Discriminators (CFD)
- The photomultiplier assemblies (PMT)
- The coincidence unit (CU)

According to the proposed architecture, whenever the CU detects a coincidence from the the CFD signals, it generates two triggers and sends them

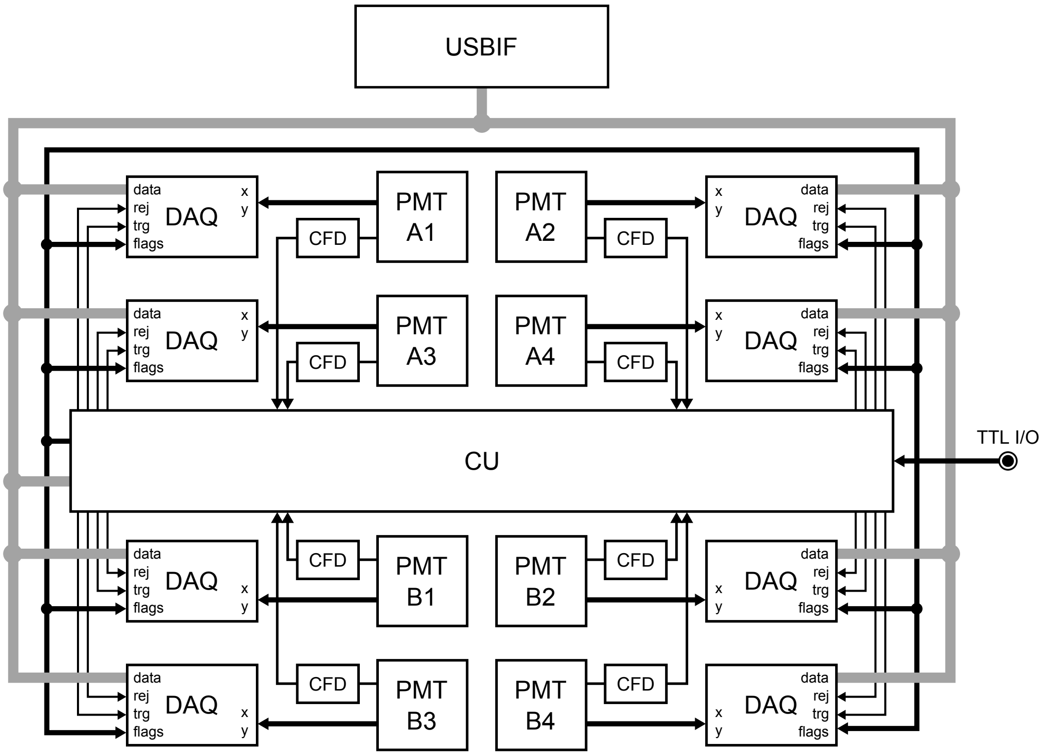

Figure 3.1: First QPEM architecture proposal [Franchi08c].

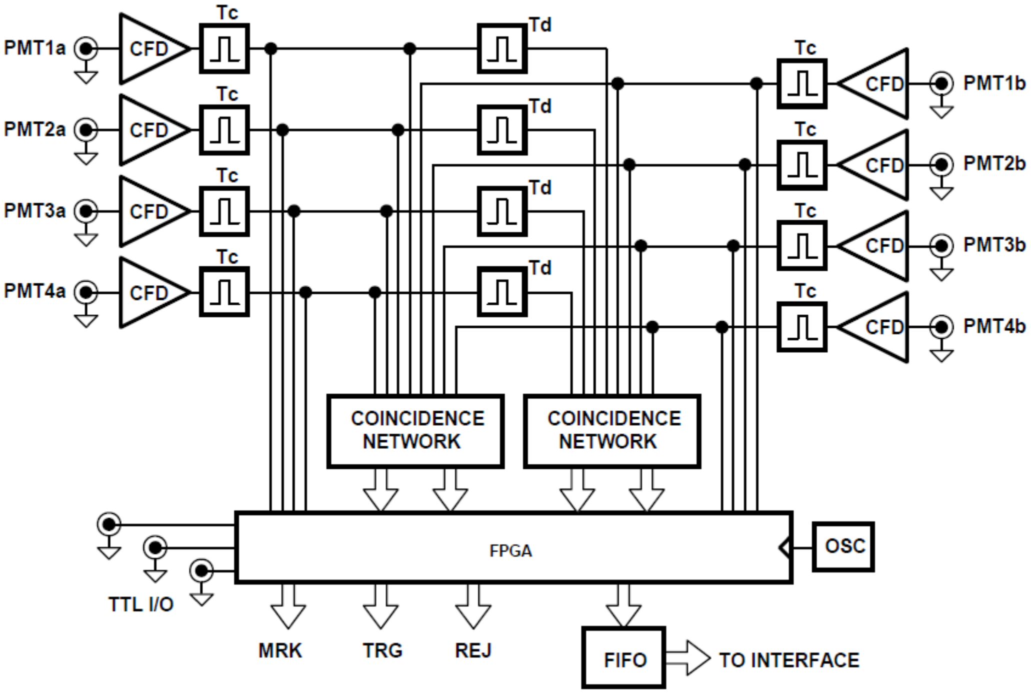

Figure 3.2: Schematic diagram of the first coincidence unit proposed for the QPEM.

to the DAQ boards, together with a set of event flags and sequential indices (markers). The flags could indicate additional informations, as if the event was a random coincidence or it was affected by pile-up. In case the CU detects some degrading conditions, such as multiple coincidences or pile-up, it generates a *reject* trigger that is routed to the DAQ boards to interrupt the event acquisition. All signals are transmitted asynchronously. When a DAQ is triggered it sends its data through a common bus to the USB interface, which forwards the data to the host computer and manages slow control transfers.

The idea behind the CU was to implement in the same board a combinatorial coincidence resolution network and a FPGA that would monitor the coincidence network and connect the DAQ boards to the USB interface Figure 3.2).

In this first conceptual architecture, the coincidence board receives the timing signals from the PMTs after the digital conversion performed by the CFD. The outputs from the CFD are shaped to have a time duration T_c and are routed to the FPGA with a series of flat twisted cables, driving the +5V, -5V, GND, and the differential Positive Emitter-Coupled Logic (PECL) outputs. CFD thresholds can be set with trimmers mounted onto the CFD boards while the signal time delays can be set with trimmers mounted onto the coincidence board.

As a result of this thesis, as it will be explained later, the USBIF and the CU had to be designed from scratch. The DAQ and CFD boards had to be re-factorized, i.e. the electronics design was the same as in previous systems [Guerra06, Vecchio09] but implemented, with minor modifications, on newer printed circuit boards having form factors compatible with the new modular detector assembly. The PMTs were replaced with exactly the same as used in DoPET [Belcari07], i.e. the H8500 (Hamamatsu Photonics K.K., Shizuoka Pref., Japan), 5×5 cm^2 wide.

3.2 Detector assembly

A mechanical support for the QPEM scanner has been already realized (Figure 3.3a). The aim of this structure is to provide a simple and adjustable planar geometry for demonstrating purposes. The support consists of two planar heads of 10 cm × 10 cm each mounted on a sliding column. Each head contains up to four detector modules, which are tightly assembled and optically coupled to the scintillator crystals (Figure 3.3b). The adopted scintillator is a LYSO matrix of 23×23 pixels (1.9×1.9 mm^2 each) 16 mm thick, with a 2 mm pitch. The crystal total area is thus 5 cm × 5 cm, as the PMT block.

3.3 Front-end signal conditioning

The H8500 tubes have 64 output signals, each one emitting a current proportional to the light received at its corresponding anode. These signals pass through a *signal conditioning stack*, made of a coding board, a preamplifier board and a timing board. Conditioning circuit boards have been realized with the same form factor of the scintillating crystal and the photomultiplier tube, in order to allow the whole module stack to be aligned with others to form the full detector block (Figure 3.4).

The coding board consists of a Symmetric Charge Division (SCD) [Olcott05] resistive network, which is particularly suitable for its simplicity and good performance. The SCD reduces the 8×8 anode signals of each PMT into $8 + 8$ signals, that codify separately the X and Y barycentre of PMT currents.

These 16 signals enter a passive resistive chain that further reduces the

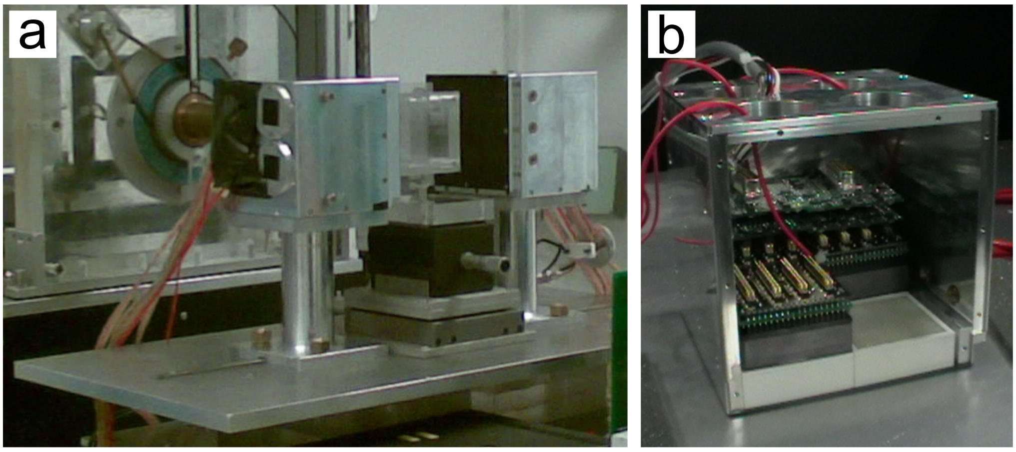

Figure 3.3: (a) Mechanical support for the QPEM detectors. Both detectors are positioned in front of a proton beam cannon for a dosimetry experiment. (b) A detector block. The four modules are tightly packed and pushed towards the crystal matrix by means of metallic springs.

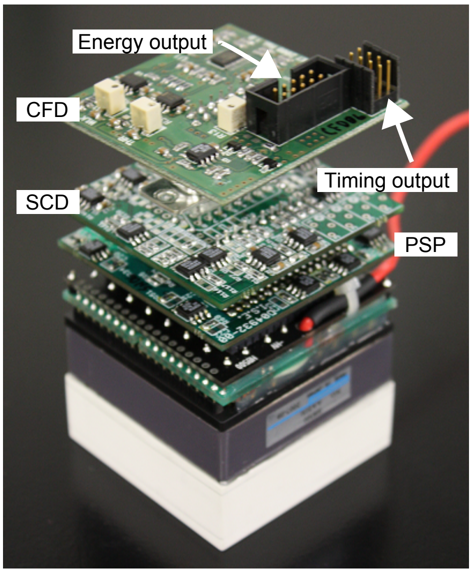

Figure 3.4: QPEM detector module. Stacked up to down are the CFD, the SCD, the PSP, the photomultiplier tube and the LYSO crystal.

number of signals to Anger-like 2 (x) + 2 (y) [Belcari07]. The digitized Anger value is the raw data that is streamed to the host. Energy signals are preamplified and smoothed in a separated board, the *pulse-shape preamplifier* (PSP), and routed to the DAQ board for digital conversion. The role of the PSP is two-fold: on one hand it amplifies the signal in order to improve the signal-to-noise ratio and adjust dynamic range at the digital conversion stage, on the other hand it slows down the pulse, in order to introduce a certain time margin to allow the digital processing unit to resolve coincidences and trigger the acquisition.

Given that processing delays are still being defined, and because the signal-to-noise ratio degrades with higher delays, a fine tuned RC constant for the PSP will be derived only after the acquisition system has been defined and characterized.

3.4 The constant fraction discriminator

The last dynode output of the PMT is forwarded directly to CFD, which is the last board of the conditioning stack. The CFD generates a differential PECL signal with a well defined, fixed delay after the dynode voltage passes a fraction λ of of its own peak [Jordanov94]. The fraction λ is usually chosen depending on the PMT output properties and, in our case, as a first estimation it has been set to 20%. Future works will be aimed at deriving the optimum value of λ.

A simplified scheme of the CFD is shown in Figure 3.5. The understanding of the way the CFD works is paramount for the fine tuning of front-end electronics. The CFD is one of the components that contributes most to the total system dead time, thus being a critical stage in the overall performance characteristics. Its dead time is of the blocking type, thus subject to paralysis at high count rates. Moreover, the timing precision of the generated trigger constitutes a mayor limiting factor for coincidence resolution and detection efficiency.

The signal discrimination is obtained employing two adjustable comparators, one for the minimum amplitude threshold and the other for the signal fraction threshold. The first is called *arm comparator*, the other *walk comparator*. The amplitude independent function that determines the digital trigger instant is the subtraction between the input signal $f(t)$, delayed by ΔT, and an attenuated copy αf. The timing diagram of involved signals is reported in Figure 3.6.

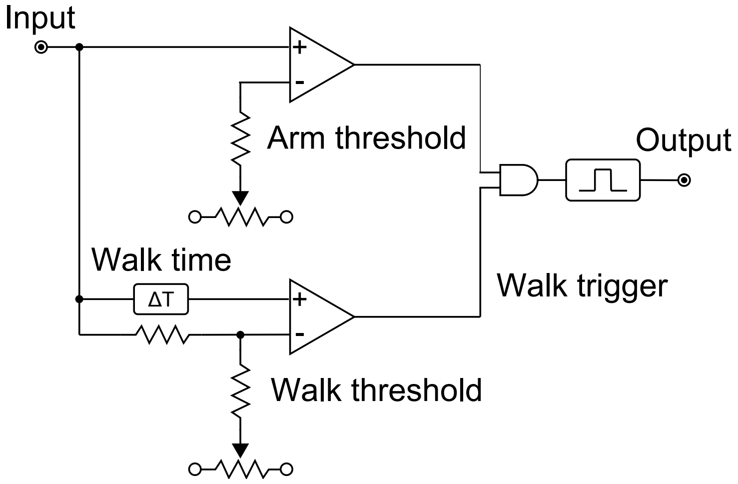

Figure 3.5: Simplified scheme of the constant fraction discriminator implemented in the QPEM scanner.

The timing signal will rise at the instant τ such that

$$f(\tau - \Delta T) = \alpha f(\tau) \tag{3.1}$$

If we substitute in the 3.1 $f(t) = kn(t)$, where n is the normalized signal of unitary amplitude, it is evident that the triggering instant does not change with the amplitude k. It can be also shown that best timing performances can be obtained setting $\alpha = \lambda$ and $\Delta T = \lambda t_r$, where t_r is the rising time of the last dynode signal [Franchi08a]. Moreover, it is worth mentioning that reducing ΔT to zero drives the walk signal always high, thus making the CFD work as a simple threshold comparator.

Finally, special attention must be paid to the arm comparator. In fact, the balance between low threshold values and high ones implies a critical trade off between detection efficiency and dead time. At higher thresholds correspond shorter timing outputs, hence shorter dead times. However, higher thresholds are not reached by smaller pulses, therefore detection efficiency is degraded.

As for the signal fraction λ, it will be possible to derive the optimum threshold value only from statistical analysis on large acquisitions, which will be available after a functional acquisition prototype has been completed. At the current status, measurements showed that the output pulse generated by the two comparators oscillates roughly from 200 ns to 700 ns, depending on the amplitude of the input pulse.

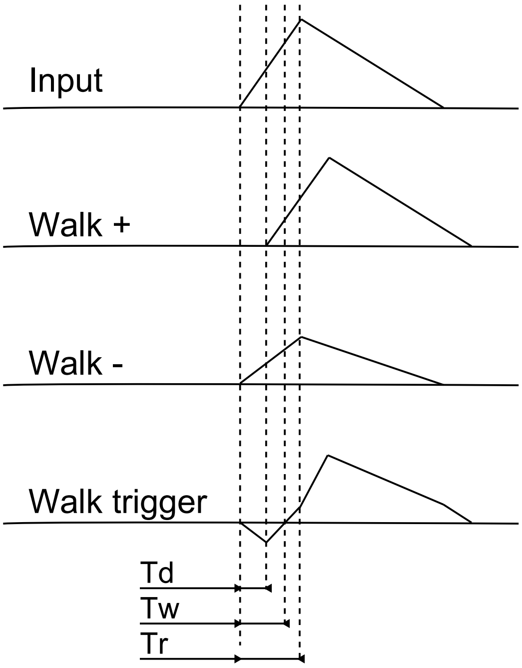

Figure 3.6: Timing diagram of the signals involved in the constant fraction discriminator.

3.5 Digital pulse shaping

Digital pulse shaping was realized in the QPEM based on monostable circuits as illustrated in Figure 3.7, and are necessary to accomplish the following four tasks in the coincidence board:

- Input equalization, to compensate for differences in cables propagation delays.
- Coincidence and random coincidence window, which represents half the coincidence resolution.
- Decorrelation delay, to generate random coincidences.
- Output shaping, to allow combinatorial outputs to be synchronized at frequencies compatibles with the adopted FPGA technology.

The range of the timing feature of each monostable is achieved changing the capacitance, while the fine value is achieved regulating the variable resistor. To perform the four listed tasks, the shapers are arranged as illustrated in Figure 3.8. A simplified schematic is provided in Figure 3.9.

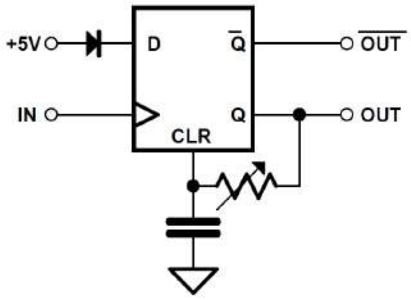

Figure 3.7: Monostable stage adopted for pulse shaping.

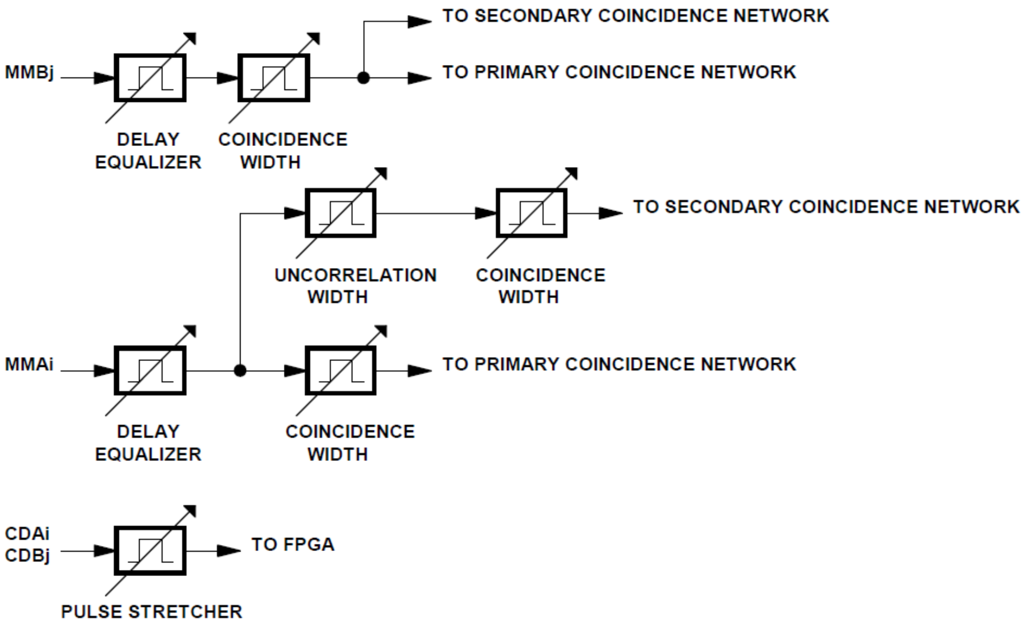

Figure 3.8: Schematic configuration of monostable circuits to implement the shaping functions.

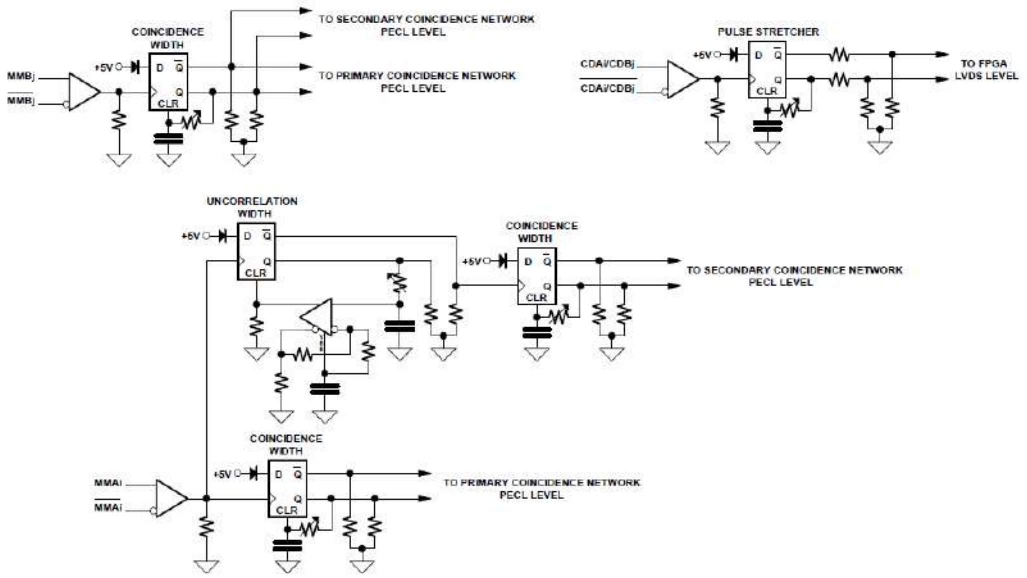

Figure 3.9: Schematic diagram of the signals shaping circuitry.

It is worth pointing out that the digital shapers aimed at delaying a digital signal are different from those that generate a signal with a specified width. Delaying shapers have been used in order to allow a fine tune of the delay interval, at the cost of a higher power consumption. In the final version, once all delays have been determined, the same will be achieved with fixed inductive components.

The used chip for monostables is a quad flip-flop MC100E131 which operates at +5 V and absorbs 58 mA. Each flip-flop is terminated with a couple of 180Ω resistors that drain 40 mA. Therefore, a single monostable drains about 55 mA at +5 V and consumes about 275 mW. The pulse shaping circuit was developed by AGE Scientific following the specifications derived during the work of this thesis.

3.6 The Coincidence network

The coincidence network resolves contemporary occurrences of two input shaped triggers, within a time window $2T_c$. The discrimination is achieved AND-gating the input signals of fixed length T_c from the 4 PMTs of head A with the signals from the 4 PMTs of head B. The resulting outputs, $CDAi$ and $CDBj$, indicate which of the 8 tubes were involved in the coincidence event. These signals are then directly routed to the DAQ boards to trigger the peak detection and A/D conversion. The triggers are also routed to the

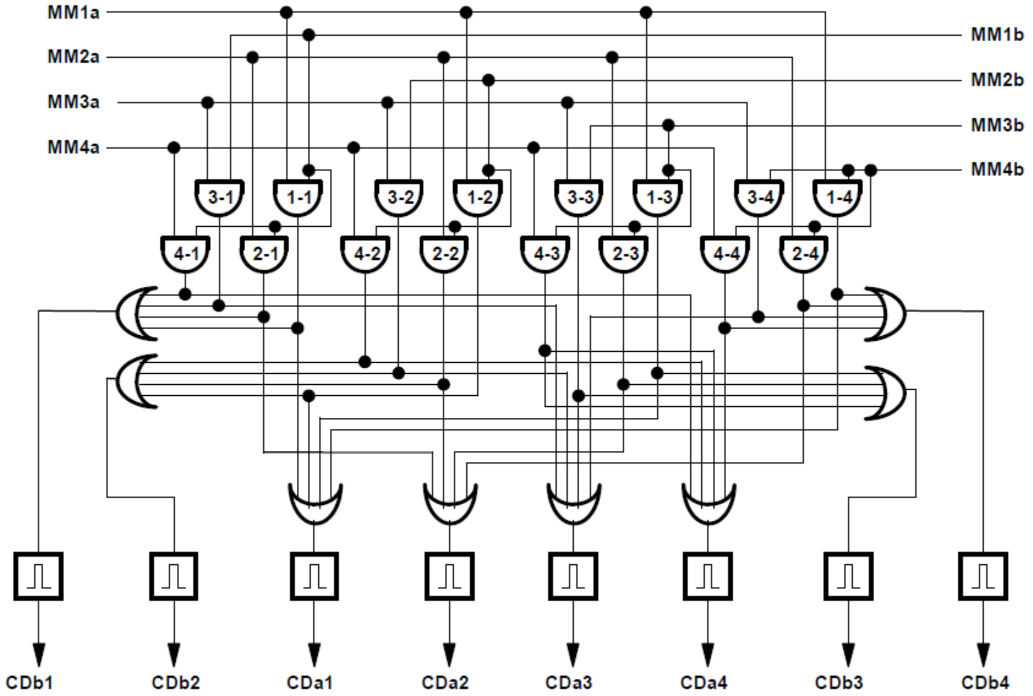

Figure 3.10: Coincidence network of the first QPEM proposed architecture

main processing unit to enable real-time activity analysis. An equivalent coincidence network is used for the random coincidence measurement. The schematic of the coincidence network is shown in Figure 3.10.

The boards are proposed with PECL components, MC100E series, chosen for its sub-nanosecond propagation and rising times. As it can be seen from the schematics in Figure 3.10, the number of required gates for pulse comparison of N PMT tubes is N^2 AND gates plus $2N$ OR gates. At the time of the first architecture proposal a concrete implementation was still not available, due to concerns regarding the high power consumption estimated that could have hampered the correct operation of the coincidence resolution [Franchi08c, Franchi09].

3.7 The DAQ boards

Each DAQ board mounts a Cyclone II FPGA (Altera Corp., San Jose CA), which manages buffering, data transfer and controls four on-board peak detectors. A picture of the DAQ board is showed in Figure 3.11 and its schematic architecture is reported in Figure 3.12.

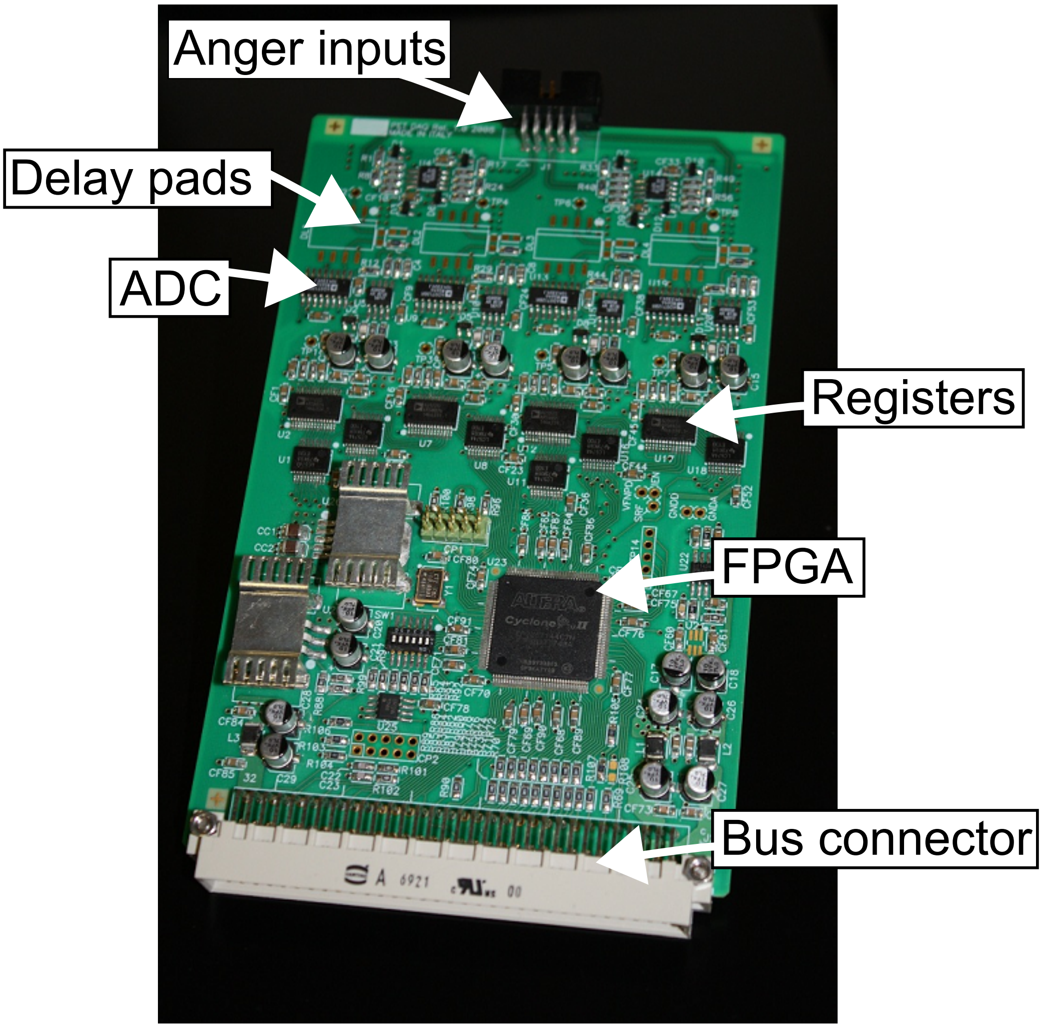

Figure 3.11: The DAQ module.

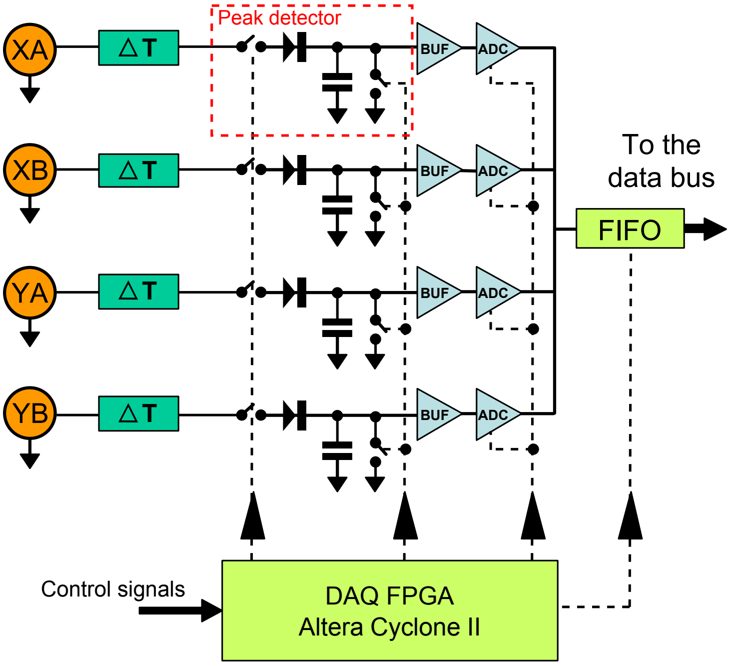

Figure 3.12: Schematic architecture of the DAQ baord. XA, XB, YA and YB are the Anger coded inputs coming from the SCD board.

The peak detector follows the value of incoming energy signals from the PMT with a 12 bit ADC and holds on the highest voltage. Peak hold and registration is enabled only after an acquisition trigger is received. This is because RC peak followers could not sustain charge-discharge cycles at typical single photon rates. Each DAQ board is provided with an input inductive delay stage, which is required to compensate coincidence processing delay. The implemented delay must be sufficiently long in order to turn on the peak detector before the actual energy signal peak has passed through.

The input stage of the board provides also pedestal levelling circuitry. In fact, a positive pedestal value is required in order to correctly convert the incoming signals. This depends on the fact that the ADC input stage has been configured having ground as lower dynamic range bound. The schematic of the AD9220 ADC polarization circuit on DAQ boards is reported in Figure 3.13. The dynamic range is set to ground by connecting the input VINB to VREF, as it is described in the AD9220 datasheet.

In this configuration, any negative analog voltage is clipped to zero. Therefore, in order to prevent negative pedestal values, an analog offset is added by means of a summing amplifier, as shown in Figure 3.14.

The method used for event transmission to the main control unit is an

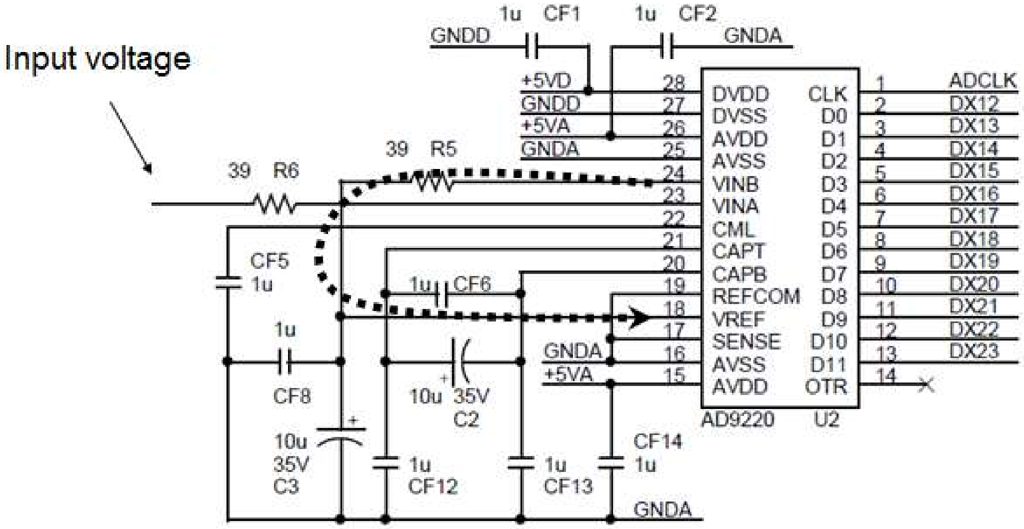

Figure 3.13: Schematic of the ADC polarization circuit.

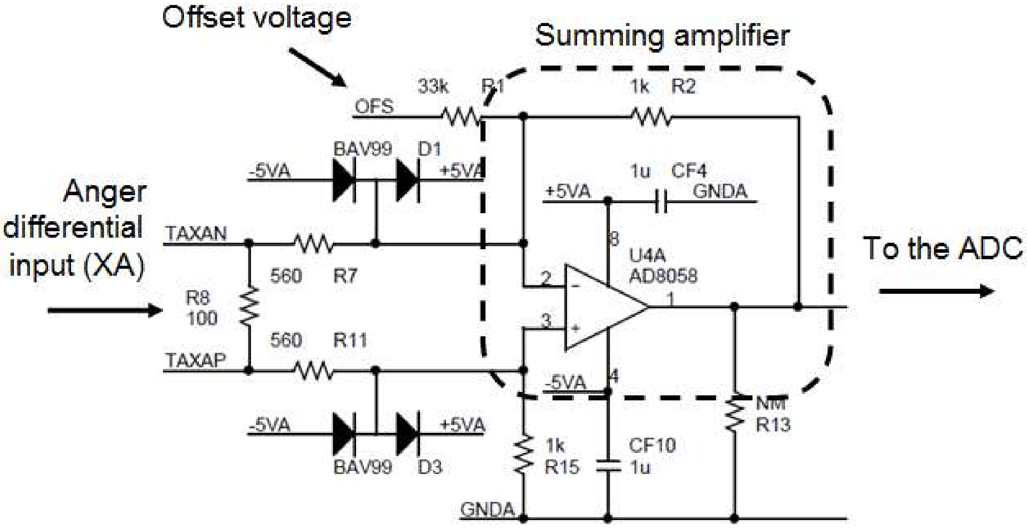

Figure 3.14: Schematic of the pedestal offset summing circuit.

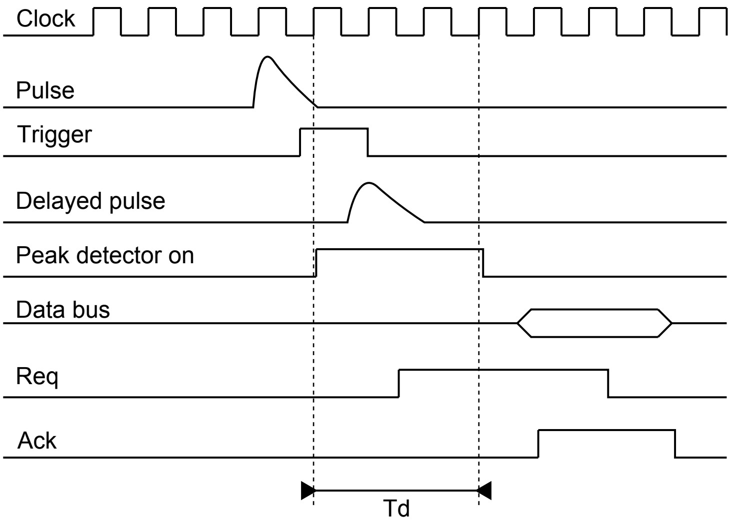

Figure 3.15: Timing diagram of pulse acquisition and data transmission protocol.

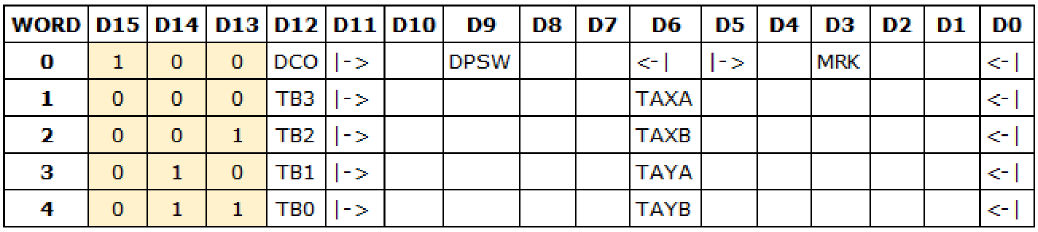

WORD	D15	D14	D13	D12	D11	D10	D9	D8	D7	D6	D5	D4	D3	D2	D1	D0
0	1	0	0	DCO	|->		DPSW			<-|	|->		MRK			<-|
1	0	0	0	TB3	|->					TAXA						<-|
2	0	0	1	TB2	|->					TAXB						<-|
3	0	1	0	TB1	|->					TAYA						<-|
4	0	1	1	TB0	|->					TAYB						<-|

Figure 3.16: Data structure of a single event.

asynchronous req/ack protocol. The pulse acquisition timing diagram is reported in Figure 3.15. The data packet that is transmitted consists of five 2-bytes wide words, thus making the coincidence event size as big as 20 bytes. The single event packet content is showed in Figure 3.16.

In the timing diagram of Figure 3.15, T_d is the time during which the capacitor of the detector is keeping the pulse peak, thus constituting a sort of dead time. While the detector is on, the DAQ board does not accept further triggers, thus behaving as a non-blocking component. However, overlapping pulses might produce pile-up conditions that must be tracked and processed properly.

The estimated bandwidth of the asynchronous protocol, as specificated by AGE Scientific, is 16 MB/s which corresponds to a coincidence rate of 800 KHz [Franchi08b]. In the same specification it is observed that this is a maximum bandwidth that could not be sufficient. However, being the DAQ board FPGA-based, some firmware modifications are proposed in order to enhance current performances. These modifications will be discussed in Section 4.2.1 after an experimental assessment of the current transfer speed.

3.8 Summary of the available technologies and needed contributions

As it emerges from the previous sections, there is an already thriving technological framework, to which this thesis intends to contribute. Our work will provide respectively answers and concrete implementations to the questions and incomplete blocks of the conceptual architecture proposed prior to this thesis.

A table follows, in which the actual development status is summarized as a reference for next sections:

Sub-system	Development status	Needed contribution
Overall architecture	Conceptual design	Design validation and implementation
Host interface	Not started	Design, validation and implementation
Coincidence processor	Conceptual design	Design, validation and implementation
Front end electronics	Developed	Test and characterization
DAQ modules	Developed	Test and characterization
Detector assembly	Developed	Test and characterization

Table 3.1: Status of current PEM systems development.

Although complete testing and validation for the detector front-end is still needed, its development is already finished and based on a mature know how. Conversely, the QPEM acquisition architecture, the host PC subsystem and the coincidence detection technology are still based on conceptual plans. In other words, a detailed implementation is not available yet.

The following chapter will describe the strategies, the reasons, the solutions and the designs that, after a careful analysis of the current status, have been proposed for the completion of the QPEM scanner.

Chapter 4

Contributions to the design and development of the QPEM scanner

4.1 Analysis of the conceptual proposal prior to this thesis

There is a series of aspects that in the first proposal have been left undetermined, and that required detailed studies in order to guarantee the correct operation of the system. While the detector technology is well mature and robust, as demonstrated in previous publications [Belcari07, Vecchio08], the most questioning part is the acquisition sub-system and inter-boards communications. Some of these questions could be answered by delving into published materials and analytic considerations, some others had to be dealt by means of sub-functional prototypes able to reproduce the subsystem under research. In the following sections, the different approaches will be analysed and discussed.

Special attention will be paid to timing performances, power consumption, flexibility and complexity on the following aspects:

- Modularity. The real necessity and benefits of a modular approach have to be proved. System modularity is expected to increase overall hardware and software complexity, thus requiring the study of the cost/benefit ratio.

- Acquisition bandwidth. One of the characteristics of the proposed scanner is high sensitivity. This requires not only good detectors design, but also an efficient acquisition platform.

- Events timing and coincidence resolution. In order to achieve a high S/N ratio, the modular scanner must have a coincidence processor with excellent timing properties.

In Section 4.2 we will then propose alternative solutions to those critical parts that could hamper the achievement of the desired system performances.

4.1.1 The modular approach as a strategy to reduce dead time

One of the main figures of merit of a PET acquisition system is dead time. This is specially true for clinical systems, in which the radiation dose and scanning interval have to be minimized, thus making of paramount importance to minimize events losses. For breast imaging, in a realistic scenario the imaged breast is injected with roughly 100 μCi [Weinberg05b], the isotope disintegration rate would be around 3.7 MHz. Given that the detector scintillators of choice are 16 mm thick pixellated LYSO blocks, we can calculate the absorption probability, which is $\alpha = e^{-d/\mu} = 0.75$. Where d is the scintillator depth and $\mu = 12$ mm is the attenuation length of LYSO [Humm03]. If we scale the disintegration rate by the absorption efficiency and the solid angle seen from the centre to 15 cm × 15 cm detector plates separated by 8 cm, which is 54% (derived with the formulas obtained in Appendix A), we obtain a single photon rate of approximately 1.5 MHz per detector, without taking into account the single photons coming from the torso and the intrinsic radioactivity of scintillating crystals.

At this rate, and given that front-end electronics behave as paralysable counting devices with dead time τ, we can derive the losses vs dead time characteristic, illustrated in Figure 4.1, with the following [Cherry03]:

$$\text{Losses [\%]} \approx 100 \times 1.5\ \text{MHz} \times \tau \tag{4.1}$$

It is evident from the plot that if we want event losses to be below 10% we must keep the dead time below 700 ns. But if we consider that the dead time of the CFD varies from 200 ns to 700 ns, it results that our constraint is hardly achievable with a single processing module per detector plate. Reducing CFD dead time by fine-tuning of comparators thresholds and dynode pulse amplification is not expected to change considerably these values. Deeper technological changes, such as replacing the pulse discriminating technique could solve the problem, but would imply a significant development effort. Conversely, by adopting the modular approach, the total detector dead time it is expected to be reduced by a maximum factor

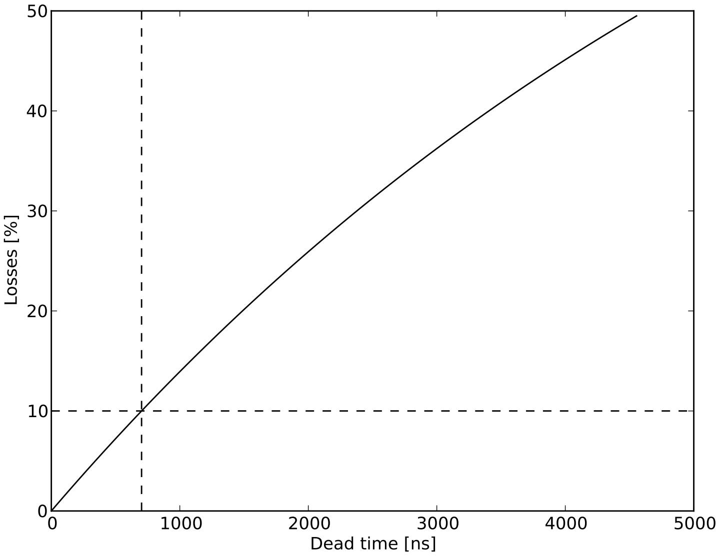

Figure 4.1: Loss versus dead time characteristic for a dual 15 cm × 15 cm PET system with a detector separation of 8 cm with an incoming activity rate of 1.5 MHz.

$f = n^2/(n^2 - (n-1)^2)$, where n is the number of modules per detector. This factor is calculated considering the probability that two subsequent photons hit different modules, thus being both accepted even if the first pair is still busy. A summary of expected dead time for different module configurations is reported in Table 4.1.

Modules	Detector area	f	Expected mean dead time	Area × Dead T. product
1	25 cm^2	1	450 ns	1.1 $\text{cm}^2 \cdot \text{ns}$
2	50 cm^2	1.3	337 ns	1.7 $\text{cm}^2 \cdot \text{ns}$
4	100 cm^2	2.3	197 ns	2.0 $\text{cm}^2 \cdot \text{ns}$
9	225 cm^2	4.8	94 ns	2.1 $\text{cm}^2 \cdot \text{ns}$

Table 4.1: Dead time reduction expected by modularizing detector plates.

Table 4.1 shows how the modular approach conveniently reduces the dead time while increasing detector area in a way that the Area × Dead time figure of merit increases, thus enhancing the actual detection efficiency.

Modularization appears therefore a correct approach for achieving a wide-area, efficient PET scanner. However, the reduction in dead time has been roughly estimated, and an experimental validation is required to assess the real performance enhancements. Moreover, the development effort is expected to be low, given that most of detector technology is reused from previous systems. The real technological challenge consists in providing a convenient coincidence processing technique, as it will be discussed in Section 4.1.5.

4.1.2 Bandwidth measurements and design modifications

The next questions that come to mind are: how many valid events are expected to be acquired? How are they distributed in time? And, how many of them can we accept to lose? Although it is hard to answer to these questions for the new quad system, because of the great number of unexplored variables, we could try to define a first estimation based on known scenarios. For example, we know that state of the art acquisition systems (Section 2.5) with geometries similar to our own hardly exceed coincidence acquisition rates of 700 kHz. Moreover, the acquisition systems of the YAP-PET and DoPET scanner from which the detector technology has been borrowed, could sustain acquisition rates up to 50 kHz still giving good imaging results. We also know that in-beam scans see count rates that are significantly higher in the first minutes of the acquisition, which are at the same time the most important for isotope separation studies.

It would then be safe to set a target data throughput bandwidth of 1 MHz that, being the event size 20 bytes, translates to a data streaming bandwidth to the host of 20 MB/s. This bandwidth is compatible with the proposed host interface, i.e. the USB, being its maximum bandwidth 60 MB/s. However the achievable bandwidth also depends on the acquisition protocol, and the software implementation, so that it is proper to do a test on-the-road in order to assess the real accessible capabilities. In order to execute the required characterization, an FPGA-based test system with a USB interface has been developed (Figure 4.2), and a series of acquisition scenarios have been tried. We refer to this prototype as *DAQTB1*. The results of the trials are reported in Table 4.2.

The acquisitions showed that as long as the transfer frame size, i.e. the size of a single USB transfer issue, was kept over 200 kB, a bandwidth of 1 MHz was easily achievable over the USB channel. Moreover, it has been shown that also the DAQ board could sustain coincidence rates up to 1 MHz. The maximum data rate has been explored by reducing the length of the REQ/ACK pulses to the minimum interval that allowed stable data transfers.

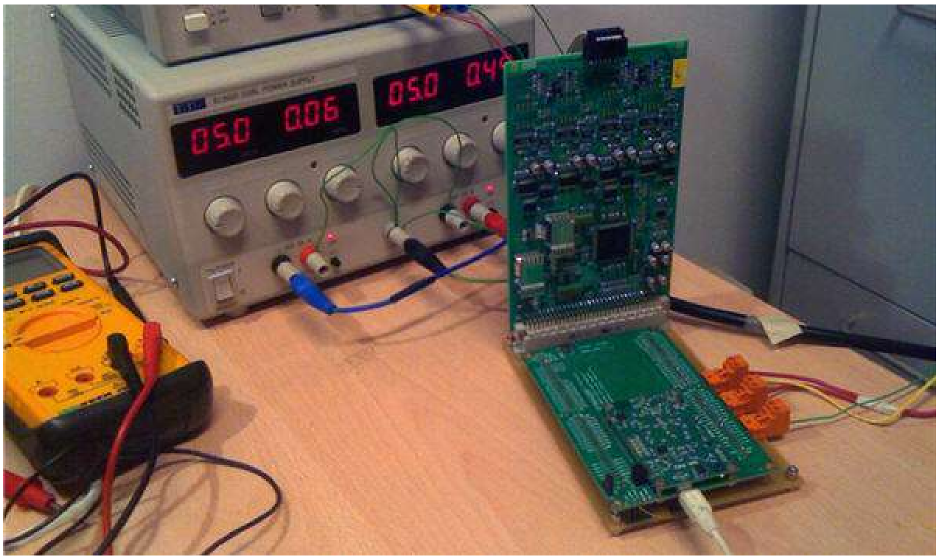

Figure 4.2: The DAQ test board DAQTB1. The board mounts an USB 2.0 controller and a Xilinx Spartan-3E FPGA.

However, the maximum rate tightly fitted the imposed constraint and left no safety margin for possible future modifications. In fact, it must be noted that the maximum coincidence rate strongly depends on the size of the event packet, which is currently 20 bytes, and does not include optional space for information we are not acquiring, but that could be interesting in the future, such as depth of interaction information, error control redundancy or timing information. Therefore, we can assert that a single bus could be sufficient for the proposed system, but it is highly encouraged to settle a path for further enhancements.

4.1.3 Considerations on the constant fraction discriminator

A series of preliminary tests have been done in order to achieve reliable timing triggers to be used in PET acquisitions. As indicated in section 3.4, the two main degrees of freedom are the signal attenuation α and the delay ΔT. We experienced that stable triggers can be achieved with $\alpha = 20\%$ and $\Delta T = 9$ ns. Moreover, given that the last dynode signal is received without any pre-amplification, or smoothing, the used comparators had to work in Schmidt mode with the highest hysteresis possible (30 mV), in order to prevent noise re-triggering effects.

As a result the CFD digital timing output showed to vary between 400

Frame size [Bytes]	Stream size [Bytes]	RW [ns]	RI [ns]	Transfer Speed [events/s]	Failure
20 K	204 K	21	21	N/A	Yes
2 K	2 M	210	1050	82 k	No
2 K	2 M	105	105	97 k	No
2 K	2 M	63	63	97 k	No
2 K	2 M	63	21	97 k	No
2 K	2 M	42	21	97 k	No
200 K	20.1 M	210	1050	148 k	No
200 K	20.1 M	210	210	369 k	No
200 K	20.1 M	105	105	634 k	No
200 K	20.1 M	63	63	877 k	No
200 K	20.1 M	63	21	965 k	No
200 K	20.1 M	42	21	1.1 M	No
1.1 M	11.7 M	210	1050	149 k	No
1.1 M	11.7 M	210	210	391 k	No
1.1 M	11.7 M	105	105	629 k	No
1.1 M	11.7 M	63	63	915 k	No
1.1 M	11.7 M	63	21	1.0 M	No
1.1 M	11.7 M	42	21	1.1 M	No
10 M	191 M	105	105	614 k	No
10 M	191 M	63	63	910 k	No
10 M	191 M	63	21	959 k	No
10 M	191 M	42	21	1.1 M	No

Table 4.2: Early tests made in order to determine DAQ bandwidth capabilities. RW is the length of the REQ pulse, RI is the time the REQ signal is kept low in order to make sure the DAQ senses the falling edge. In the transfer speed column an event corresponds to two singles, i.e. a true or random coincidence.

and 900 ns, depending on the amplitude of the incoming pulse. These values represent the first contribute to overall system dead time, and perhaps the most important, given that it is subject to paralysis, thus quickly degrading at high count rates. Therefore it appears to be critical to work on optimizing the CFD to reduce these intervals. Further studies will be aimed at detecting if the constant fraction discrimination actually improves system timing properties over threshold discrimination, or it can be safely replaced by the latter, simpler one.

However, given that the modular approach allows to reduce the virtual dead time of the whole detector to a fraction of the mean dead time of each module, we can conclude that the adopted CFD technology is compatible with the performances discussed in Section 4.1.1.

4.1.4 Timing considerations and design constraints for digital pulse generators

Although the final value of generated triggers has to be tuned after the acquisition device is ready, a series of considerations must be done in order to specify preliminary values for the lengths of the generated pulses and delays.

In order to find the required parameters for digital pulse generators, a dual coincidence network sub-prototype has been developed. The principal aim was to experiment the power consumption and timing features of a PECL combinatorial circuit. The prototype is showed in Figure 4.3 and a schematic view of its circuitry is showed in Figure 4.4.

The first important parameter that needed to be determined was the minimum pulse width achievable with the used technology. We found that the rising time 10%-90% was of 1.5ns. This means that the minimum achievable pulse width was of 4ns, and the minimum coincidence resolution 8 ns.

Moreover, we found that the equalization delays introduce a jitter comparable with the delay they were supposed to compensate. In the final version we propose to replace these delays with short leads. Being passive components, the leads would introduce no jitter and would allow to delay the signals with an accuracy of hundreds of picoseconds.

By studying the properties of the *uncorrelation* delays Tu, i.e. the additional delays applied to resolve random coincidences (Section 2.4.2), we noticed a fundamental constraint, and limitation, of the proposed coincidence network. If we call Tt_i the interval between the photon arrival on PMT i and the triggering of its corresponding DAQ, in the case it is a coincidence, Te the propagation delay of the energy signals from the same PMT to the peak detector, and Tw the width of the gating trigger, it must be

$$Tu + \min_i(Tt_i) + Tw < Te \tag{4.2}$$

In fact, if we want to perform localized random distribution estimations, we have to acquire both randomly coincident photons. Of them, one arrived in advance of Tu before the other, i.e. before the random coincidence has been detected. Therefore, the energy peak that is propagating towards the DAQ must arrive after a time Te which is greater than the total time required to turn on the peak detector. Note that Tt is small for truly coincident and delayed photons, but it is $\backsimeq Tu$ for non delayed photons detected as random coincidences.

If we implement relatively large delay lines Tl in the DAQ boards, between the anger inputs and the peak detectors, we can approximate $Te \backsimeq Tl$, if we

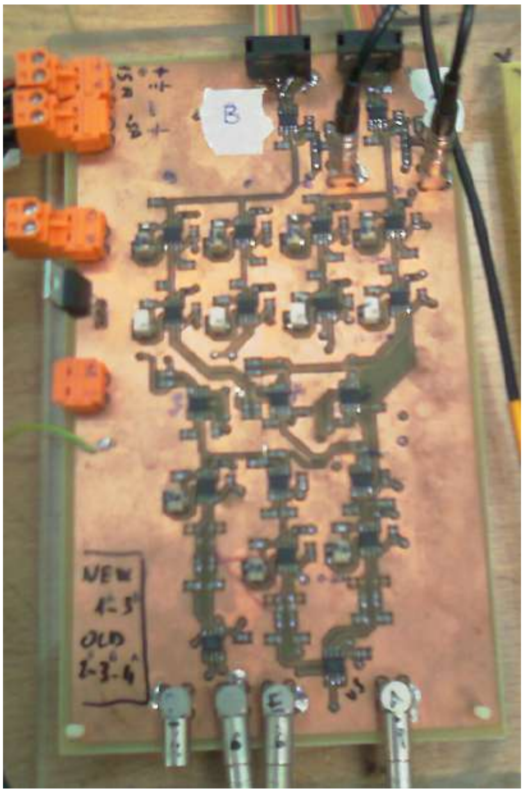

Figure 4.3: The dual coincidence network prototype for timing and power studies with PECL logic.

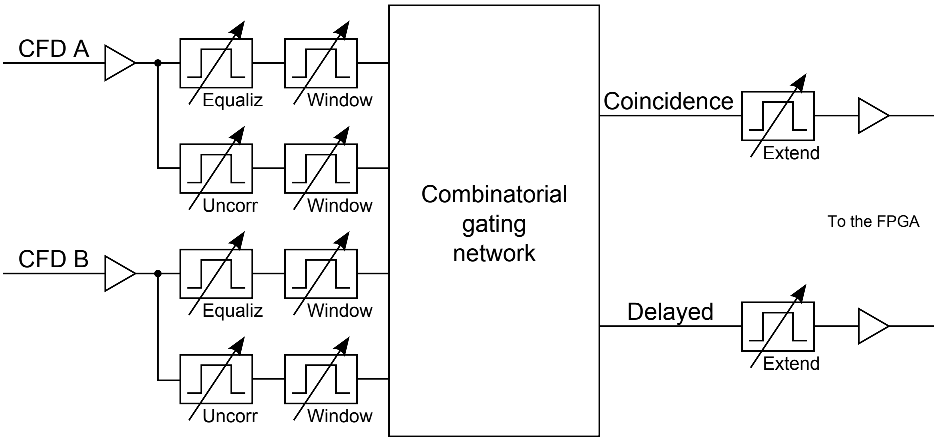

Figure 4.4: Simplified schematic of the digital pulse generators in the coincidence network prototype.

also neglect Tt_i with respect to Tu in the delayed trigger path, we can derive the following design constraint:

$$Tu \lesssim Tl \tag{4.3}$$

i.e. uncorrelation delays must be shorter than the delay lines on the DAQ boards. The meaning of each time variable is depicted in Figure 4.5.

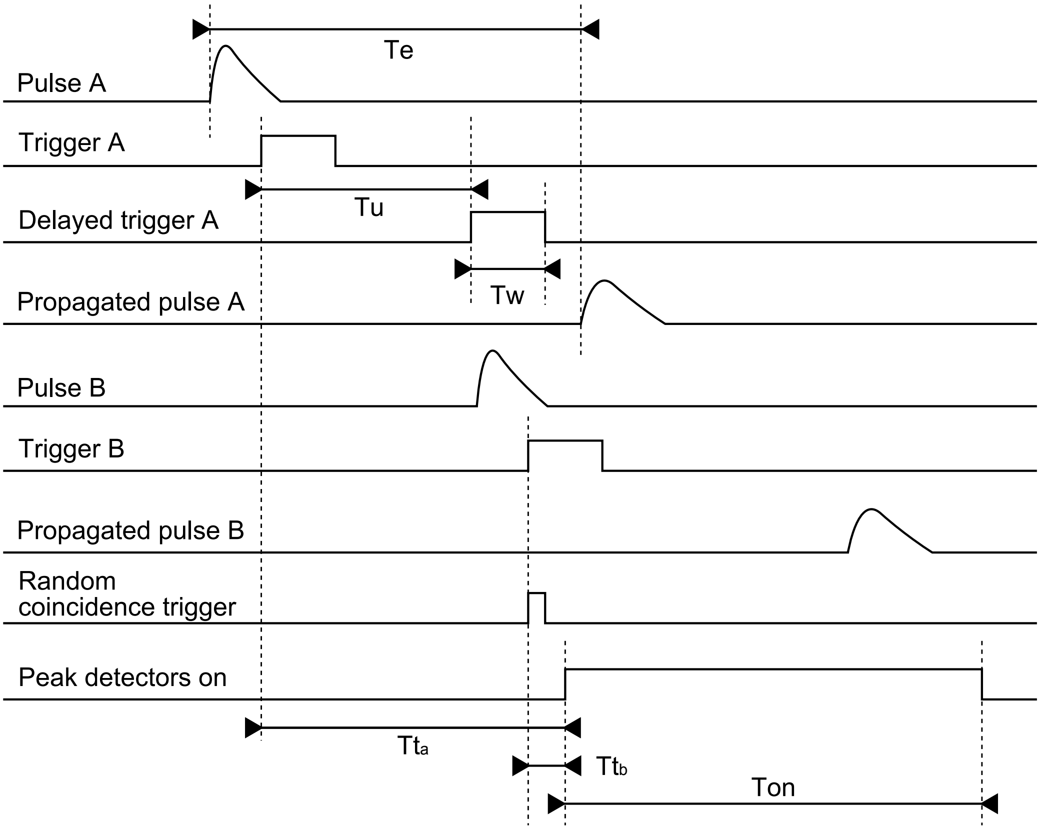

Figure 4.5: Timing diagram of the delayed coincidences triggering. Pulse widths are not in scale. Here it is represented a delayed coincidence detected in the corner case the two coincident pulses are barely overlapped. The small overlap serves to best show the sequence of involved delays.

The constraint found is specially inconvenient because of two reasons. On one hand the higher the Tl, the more is the flattening effect on the energy signal, thus the higher is the noise. On the other hand Tu is bound to be high in order to avoid estimation biases on random counts, more precisely it needs to be higher than the the dead time Tc of the CFD. To better understand the randoms biasing effect let's make an example (Figure 4.6). Counting random coincidences means counting all those photon pairs that are separated by a fixed time distance Tu. If at the instant t_1 a random coincidence occurs, the first photon must have arrived at the time

$$t_0 = t_1 - Tu + Ts \tag{4.4}$$

where $Ts \in (0, Tw)$. However, if that photon belonged to a true coincidence, and the dead time Td is longer than Tu, the second photon will arrive while its corresponding CFD is still busy, therefore it will not be detected, and the randoms final count will be systematically inferior to the actual value.

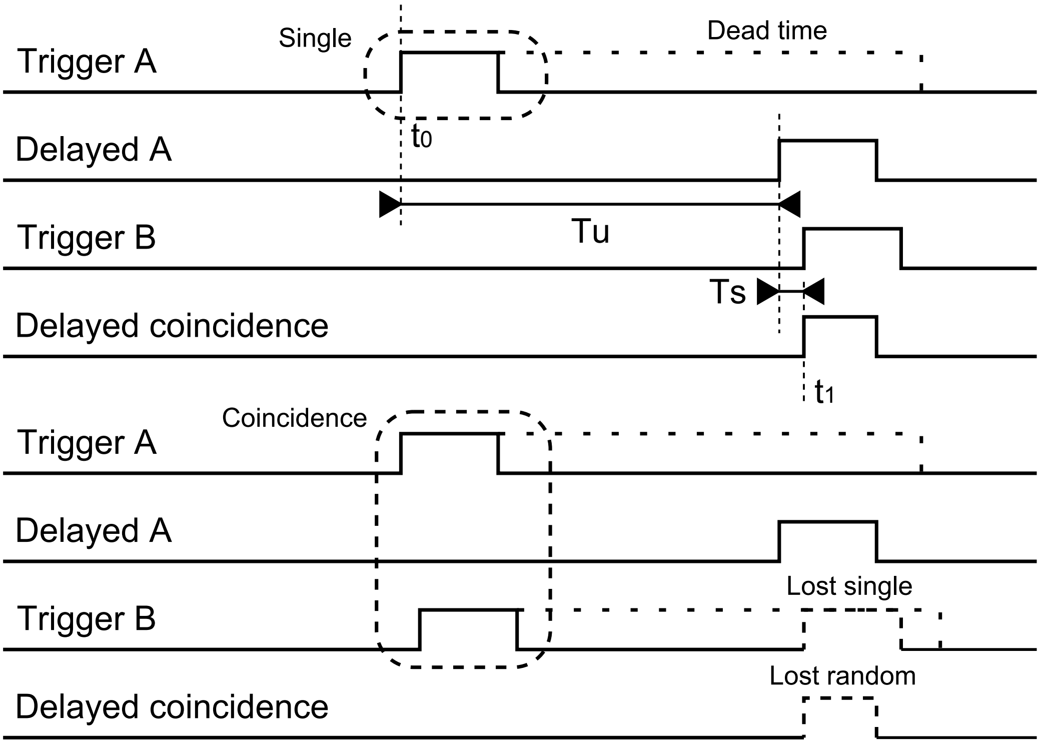

Figure 4.6: Example of biasing condition in randoms count estimation for $Tu < Td$.

A further, important constraint relates to the time Ton during which the peak detector must be kept on to be sure the pulse peak passed through. As it appears clearly in Figure 4.5, it must be

$$Ton > Te + \max_j(Tp_j) - \min_i(Tt_i) - T_{CFD} \tag{4.5}$$

Where Tp_j are the widths of the incoming analog pulses and T_{CFD} is the delay between the analog pulse and its corresponding trigger. Given that Te

is the dominant term of the second expression of inequality 4.5, we can state that

$$Ton \gtrsim Te \tag{4.6}$$

All the considerations above constrain the three degrees of freedom available, i.e.

1. Uncorrelation delay Tu
2. Analog energy pulses delay Tl
3. Peak detecting interval Ton

to the dead time Td of the CFD, and can be resumed as follows:

$$Td < Tu < Tl < Ton \tag{4.7}$$

Unfortunately, the obtained constraint appears to be quite problematic to satisfy for Tl given that Td is of the order of hundreds of nanoseconds, and such long delays would require either very long cables or inductive delaying chips that currently are scarcely available in commerce. Moreover, even if Tu can be done as long as needed with a digital pulse shaper, we must remember that pulse shapers are blocking components, and long delays would severely affect the counting properties of the system. In a more mature implementation, where Tu will be also achieved with passive delays, it will encounter the same problems as reported for Tl.

Therefore, the trigger based approach appears to be simple, but the constraints on the uncorrelation delay Tu and analog delay lines Tl, force a lower limit for the acquisition dead time, and could be a cause for the degradation on the energy resolution.

4.1.5 Problems of the coincidence network version

A main consideration that must be done in realizing the coincidence network is about the signal quality at the input of each logic gate: we require that the input signal to the AND gates must be as clean as possible, while the AND outputs can be subject to small delays. This is because the actual width τ of input signals, i.e. the width of the signal above the PECL high-level input threshold, is directly related to the coincidence resolution window, which is 2τ, and affects the coincidence detection efficiency and the random counts. On the other hand the output signal is a pulse that will be reshaped and synchronized into a processing unit.

This consideration imposes special care in the evaluation of routing delays in the PCB and eventually to implement equalization mechanisms.

By using the MC100E PECL series logic, with multi-gate chips, a first power study including only the gating logic for the 9 vs 9 version, without pulse shaping, level translation and equalization blocks, estimated a total consumption power of about 34 W [Franchi09].

Considering the additional power required by peripheral logic, the power dissipation capabilities of the board, and the fact that two coincidence network must be mounted, one for prompt coincidences and one for randoms estimation, this value seems to be too high and hardly reasonable. Moreover, the routing effort in equalizing board tracks for $2N$ gating blocks appears prohibitive.

4.2 The proposed alternative strategies

4.2.1 Enhancements to the DAQ transfer protocol

In order to improve the above performances we have examined three distinct approaches. The first one is the same proposed by AGE Scientific [Franchi08b], i.e. increasing the sampling clock of the FPGA on the DAQ would allow narrower REQ/ACK pulses thus higher transfer frequencies. This approach would be poorly invasive, because it would require only changes at firmware level, but it would lead to poor performance improvements, because of the limited variation range of the clock frequency and the relatively low impact of such a variation on transfer speed. The second approach would have been to change the transfer protocol to a synchronous one. Synchronous transfers can have bandwidths higher than asynchronous ones by orders of magnitude. Nonetheless, a synchronous protocol would require a dedicated clocking network and thus a partial re-design of the DAQ boards and a strong development effort. Given that coincident events come always in pairs, each coming from one of the two detector plates, the most convincing idea has been to parallelize DAQ accesses by implementing two asynchronous buses, one per detector head.

Such a modification requires no changes in the DAQ design and only requires 16 additional I/O lines on the mainboard and the Control FPGA. Moreover, the transfer bandwidth results doubled and efficiently distributed.

A test prototype with the dual bus version has been also developed, named DAQTB2 (Figure 4.7), that equips the same FPGA testing platform used for the previous experiment. With this prototype, tests showed that the implemented USB driver and Application Programming Interface (API)

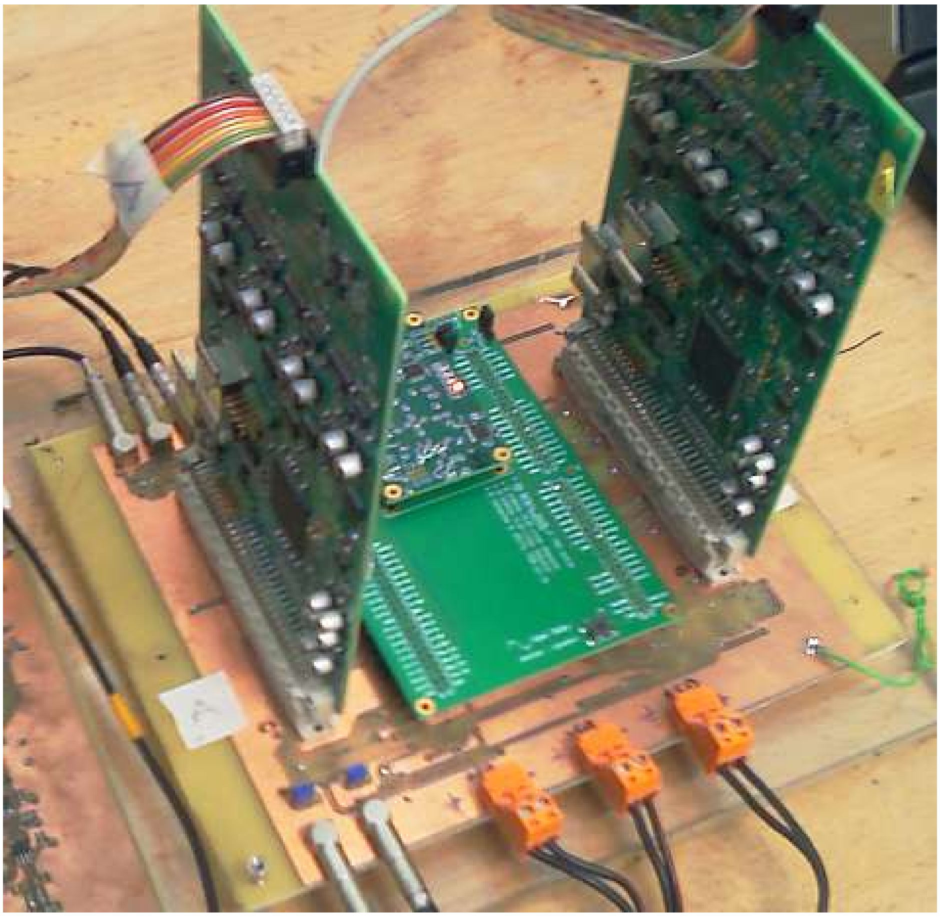

Figure 4.7: The dual DAQ test board DAQTB2. The FPGA platform is the same as in the DAQTB1, with an additional data bus and two connected DAQ boards.

set could sustain a maximum bandwidth of 30 MB/s, i.e. a coincidence rate of 1.5 MHz.

From the point of view of the host computer we also noticed that the protocol used for data transfer could have important effects on the overall acquisition bandwidth. The first implemented protocol was a sequential, repeated succession of the configuration, streaming and storage steps, as illustrated in Figure 4.8. We refer to each piece of data acquired in one repetition as a *frame*.

This protocol introduces two non-blocking dead time intervals. The first, T_1, is the time the host requires to write data to disk. The second, T_2, is the time required to setup a new streaming operation. Although modern computers can reach high writing speeds, at high acquisition rates, the time

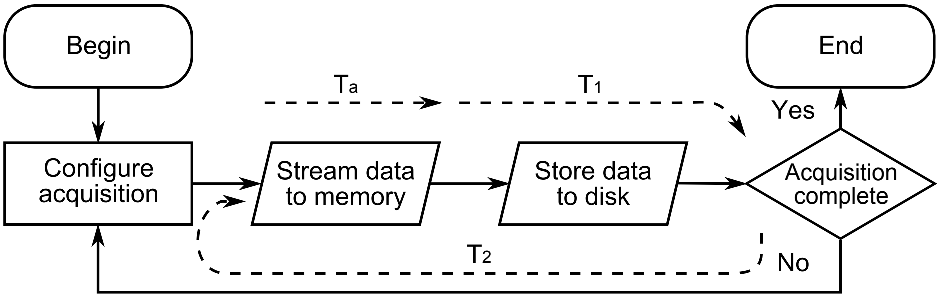

Figure 4.8: First implemented streaming protocol from the host side point of view.

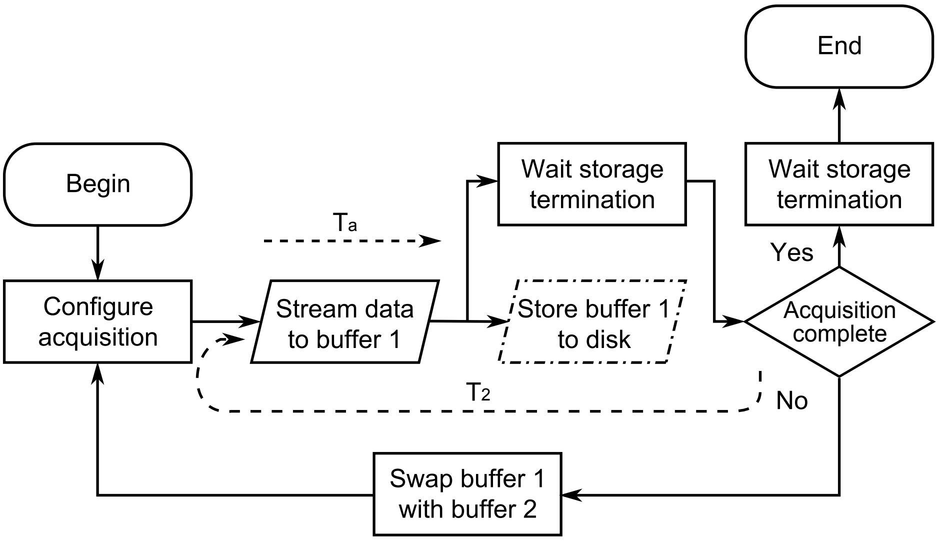

Figure 4.9: Dual buffered version of the streaming protocol.

T_a spent to acquire a fixed amount of coincidences becomes small and, at the limit of 20 MB/s it is comparable with the writing time T_1, thus introducing a duty cycle considerably lower than 100%.

In order to prevent losses due to disk storage dead time, a multi-threaded, double buffered streaming technique has been adopted (Figure 4.9). The storage operation is launched in a separated thread so that the system is free to start promptly a new read call on a second memory buffer. If the disk write speed is equal or higher than the read speed this method almost nullify the disk bandwidth overhead.

When the radioactivity is relatively low, it becomes necessary to reduce the frame size, in order to prevent operating system halts due to the long wait for frame completion. If the time T_a becomes too high, the USB driver could even respond with a time-out error thus demanding a recovery procedure.

When the frame size decreases with respect to the whole acquisition stream, the time T_a also reduces, thus becoming potentially comparable with the dead time T_2. In order to prevent losses introduced by this situation, the main FPGA is instructed to continue acquiring and buffering data into its internal registers, even when the frame acquisition has been completed. If the acquisition size is specified as a total desired number of coincidences, this number can be directly programmed into the FPGA. If it is specified as an acquisition time, the FPGA is instructed to acquire indefinitely until being stopped by the host computer. It is relevant to add that an internal buffer is anyway required to allow proper USB communication, that at the kernel happens as a series of buffered transfers of maximum 1024 bytes. Moreover, as described in the previous section, each DAQ has an internal FIFO that can buffer incoming events during the host reconfiguration step. As a result, if the activity rate is sufficiently low and the FPGA buffers sufficiently big, all losses by T_2 can be prevented with small changes in the firmware.

4.2.2 An alternative combinatorial gating tree

In order to reduce the power burden of the first proposed coincidence network, we proposed a simplified alternative implementation. The new alternative is based on the fact that the logic function of the network in Figure 3.2 can be derived following the logic paths and expressed as:

$$CDb1 = (MM1a \cdot MM1b) + (MM2a \cdot MM1b) + \cdots + (MMNa \cdot MM1b)$$

$$CDb2 = (MM1a \cdot MM2b) + (MM2a \cdot MM2b) + \cdots + (MMNa \cdot MM2b)$$

$$\cdots$$

$$CDa1 = (MM1b \cdot MM1a) + (MM2b \cdot MM1a) + \cdots + (MMNb \cdot MM1a)$$

$$CDa2 = (MM1b \cdot MM2a) + (MM2b \cdot MM2a) + \cdots + (MMNb \cdot MM2a)$$

$$\cdots$$

However, grouping the common multiples, the same boolean equations can be refactorized as

$$CDb1 = MM1b \cdot (MM1a + MM2a + \cdots + MMNa)$$

$$CDb2 = MM2b \cdot (MM1a + MM2a + \cdots + MMNa)$$

$$\cdots$$

$$CDa1 = MM1a \cdot (MM1b + MM2b + \cdots + MMNb)$$

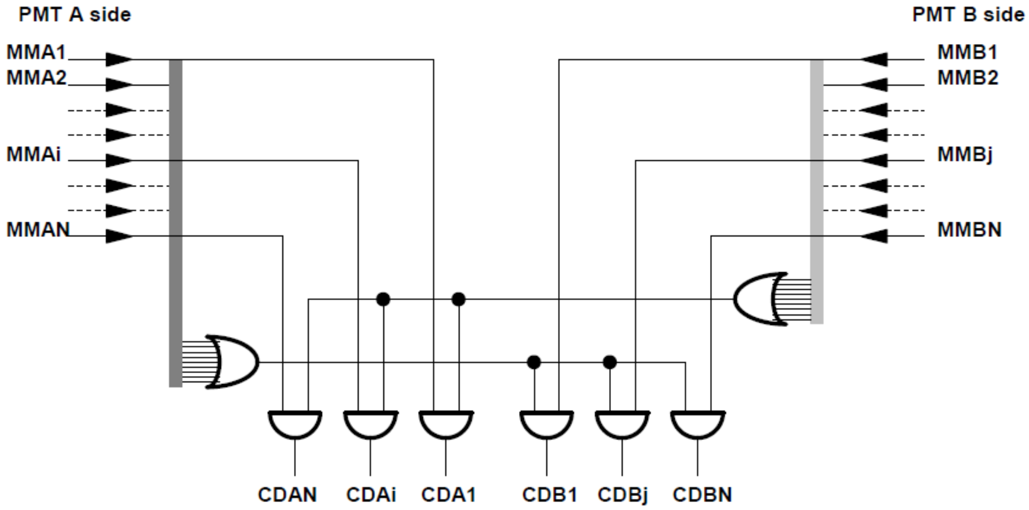

Figure 4.10: Optimized coincidence network.

$$CDa2 = MM2a \cdot (MM1b + MM2b + \cdots + MMNb)$$

$$\dots$$

This kind of refactorization is actually a common procedure in digital design [Mano01], and leads to the minimized implementation illustrated in Figure 4.10.

With this implementation the number of total logic gates is $N + M$, where N is the number of PMTs and M the number of detector plates. The payback is the introduction of a gate level before the AND-gating level, which could decrease coincident input pulses. Moreover in principle the OR-gate level should be doubled because there are no commercial OR chips available with a fan-in equal to 9. However PECL logic offers wired-OR capabilities, and therefore if we change the OR-gates for current buffers we obtain a clear AND-gating with $2N$ gates. The final schematic then results as in Figure 4.11. Table 4.3 shows the used chips and their power consumption.

Chip	Gate	Core [mW]	Terminations [mW]	Gates/chip	N. Chips	Total [W]
MC100E104	AND	190	1200	5.56	4	5.56
MC100E122	Buffer	205	1012	4.87	4	4.87

Table 4.3: Logic gates used in the final version of the coincidence network.

The total dissipated power is then about 10 W, which is about 30% of the power dissipation of the original design.

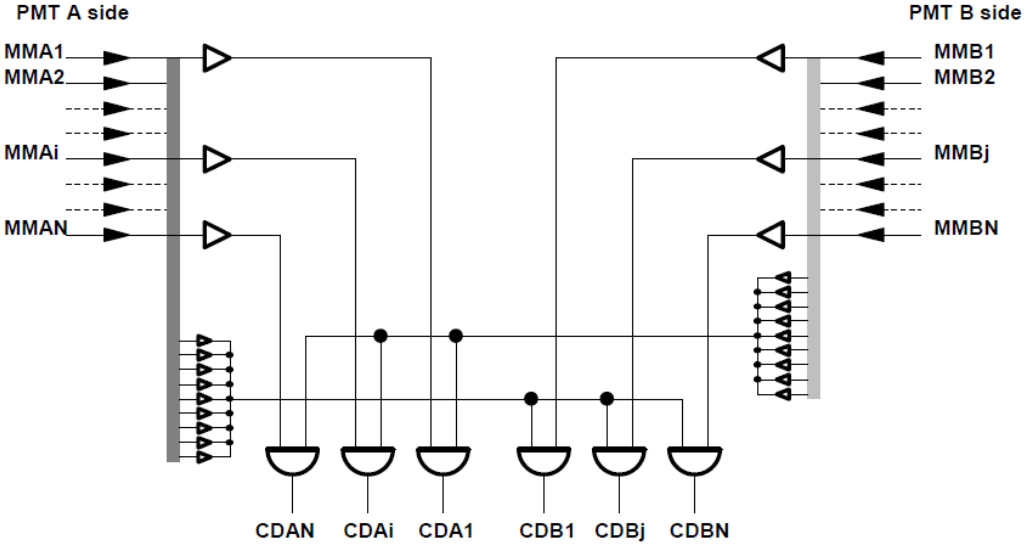

Figure 4.11: Optimized coincidence network with wired OR.

4.2.3 The innovative random detection technique

Any random count correction technique consists in estimating the background activity generated by random coincidences [Brasse05]. The technique usually implemented for random correction is based on the delayed window technique. Alternatively, the random coincidences are estimated from singles count rate. The estimated random distribution may be subtracted from the prompt signal on-line, or stored as a separate sinogram or planogram for later processing. For example this distribution can be either subtracted from the measured data or used to extract statistical information in a Maximum-Likelihood Expectation-Maximization (MLEM) algorithm [Moehrs08].

In the standard delayed window technique, both signals from the detectors involved in the "random" event are acquired. In systems where an event is acquired only when a coincidence is detected (singles are not acquired), a series of timing constraint must be applied to the energy signals path. In section 4.1.4 we revised these constraints and found that some of them are quite problematic to accomplish.

- To acquire the signals from the modules involved in a prompt coincidence a time delay Tl should be applied to the position signals to wait for the system to be ready for the coincidence trigger.

- The time delay Tu should be longer than the dead time Td of the constant fraction discriminator to avoid statistical biases on the delayed event distribution (e.g. if $Tu < Td$ no random. coincidences can occur after a prompt coincidence).

- To acquire the signals from the "delayed" side, an additional the applied delay Tl must be longer than the uncorrelation delay, i.e. $Tl > Tu$.

With the delayed window technique, timing signals from one detector are delayed by a time significantly greater than the coincidence resolving time $\tau = 2Tw$ of the circuitry.

A random LOR is measured when a delayed coincidence is detected, i.e. a delayed time signal in one detector is in time coincidence with a non delayed signal in a second detector. This technique has the advantage of a low systematic error (the random counts are measured by the same acquisition chain of the coincidence events with the same dead time) but the random distribution is usually affected by strong noise due to the relatively low statistics [Badawi99]. This noise also affects the reconstructed image.

In the singles-based technique the random count rate in each LOR connecting element i on head A and element $j$on head B is given by [Cherry95]:

$$r_{ij} = c_i \cdot c_j \cdot 2\tau \tag{4.8}$$

Where c_i and c_j are the singles count rate in elements i on head A and j on head B, respectively and τ is the width of the coincidence time window. Due to the high count rate statistics for the singles, this method is usually characterized by a lower noise but it can be subjected to a systematic error due to the a priori estimation of τ.

With the delayed window method, the determination of random LOR consists in measuring both endpoints, i.e. the points of interaction of the single events in both the delayed and non-delayed side. In this case the two detectors involved in the delayed coincidence are triggered to acquire the position signals, when a delayed coincidence is detected.

In principle, the correlation between the single events generating the delayed coincidence and those used for the random LOR is not required. Any randomly chosen single counts can be used for the generation of a random LOR. The only limitation is given by the fact that the random count rate for each LOR should be measured on-line in the exact conditions due to the time dependency of the random rate distribution. With this assumption, to avoid the problem of acquiring the signals produced by the event in the delayed side, we have followed a different approach for estimating a random LOR.

The implementation of the new method has been specifically designed for the dual head modular PET system under development. However, the proposed technique can be also applied in more general cases. Figures 4.12

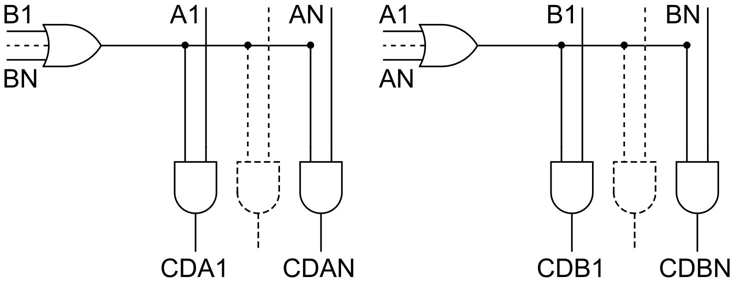

Figure 4.12: Branch of the coincidence network dedicated to true coincidences detection.

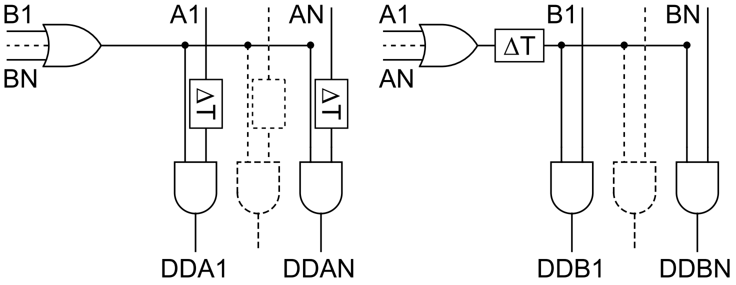

Figure 4.13: Branch of the coincidence network dedicated to random coincidences detection configured in conservative mode. In this configuration triggers incoming from the A side are delayed, and two acquisition triggers are generated whenever B coincides with A delayed.

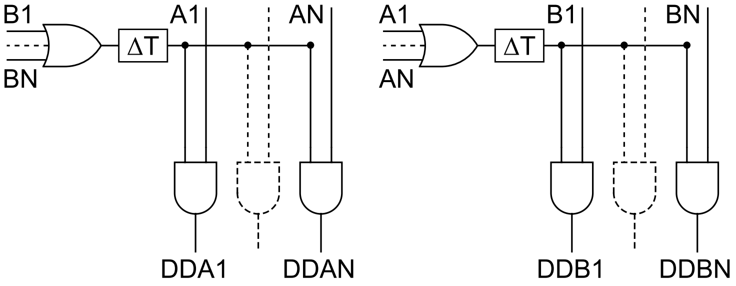

Figure 4.14: Branch of the coincidence network dedicated to random coincidences detection configured in innovative mode. In this configuration triggers incoming from both sides are delayed, and only one acquisition trigger is generated whenever A coincides with B delayed or B coincides with A delayed. The number of acquired pulses per random coincidence is only one, but the number of random coincidences doubles.

to 4.14 show the coincidence schemes for prompt coincidences and delayed coincidences in both the standard and the new approach. In the new scheme, to measure the random counts, we have symmetrized the system by generating a delayed timing signal on both sides (Figure 4.14). The logic OR of the delayed signals on one side is in coincidence with the non-delayed signal of the other side and vice versa. Once a delayed coincidence is detected, only the signal on the non delayed side is acquired. In this way only a single vertex of the LOR is measured. We call this event a ”random single”. Since the system is completely symmetric we can assume to measure an equal number of ”random singles” on both sides. The rate of these ”random singles” will be equal to the actual system random count rate. The fluctuation of the numbers of random singles on both sides will be only related to the count statistics. Once the single random events are acquired, a random LOR can be generated by the coordinates of the first random singles available on each side.

The new technique introduces two remarkable advantages. Firstly, the constraint on Tl is removed. Long analog delay lines are undesired because degrade the signal-noise ratio and are even scarcely available in commerce. Furthermore, is removed the constraint on Ton, which in turn reduces dead time in DAQ boards.

4.2.4 An integrated synchronous coincidence processor alternative

From the timing considerations on Section 4.1.4 it results that the best coincidence resolution achievable with the implemented coincidence network is 8 ns. This coincidence processor is realized with a dedicated printed circuit board whose power consumption has been reduced, with the optimizations discussed above, to a total amount of 130 W [Franchi09], which accounts for both gating logic and peripheral circuitry, such as level translation and pulse shaping.

Although the system optimizations kept the system complexity and power consumption reasonably low, they imposed a series of trade-offs and drawbacks:

- The detectors geometry is bound to be dual planar
- The combinatorial coincidence network implements large wired-OR buses that require extremely precise impedance control and terminating resistances in order to avoid signal reflections and spurious triggers, and the PCB routing is particularly complex

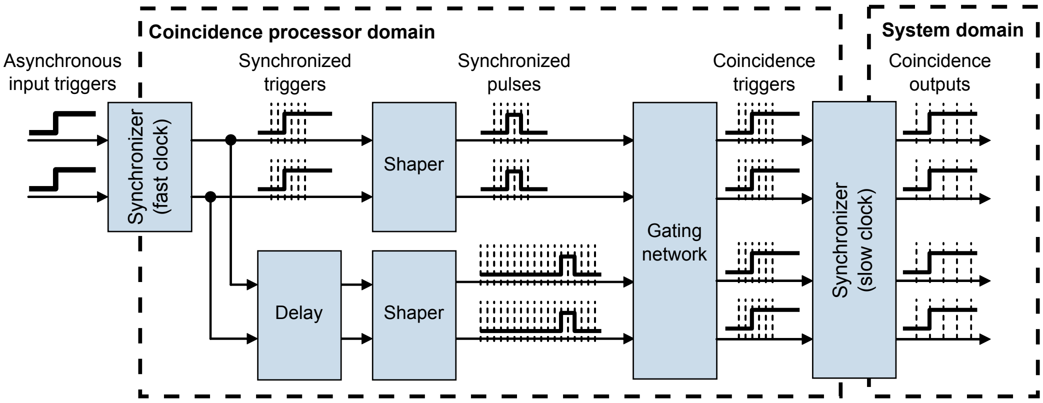

Figure 4.15: Architecture of the synchronous coincidence processor.

- Digital delay lines introduce a dead time of the blocking type

We propose an alternative, FPGA-based method for coincidence resolution that requires low device resources and no specific peripherals in order to resolve digital pulses within a time window comparable or even lower than the one achieved with the current coincidence board. The method has been developed specifically to be applied for both PEM and in-beam PET, but it is generalizable to any detector geometry.

The method consists in synchronizing the input triggers inside the FPGA, into pulses of width $W = 2\tau_{clk}$, where τ_{clk} is the clock period. The synchronization is achieved by a de-metastabilization process followed by a pulse synchronous shaping.

The goodness of the method comes from a local clock boosting that allows reducing τ_{clk} to the technological limits of the target FPGA, thus reducing the timing feature on which depends the coincidence resolution. The outputs of the boosted clock domain are then resynchronized with the slower global system clock in order to be processed. A simplified schematic of the synchronous coincidence processor is showed in Figure 4.15 and the gating timing diagram is shown in Figure 4.16.

Having narrow synchronous pulses, timely related with the incoming triggers, allows for a more effective combinatorial gating in terms of both device power dissipation and design cost. The delayed window technique for random counts estimation can be implemented by means of shift registers, and the FPGA-compatible implementation allows the architecture to be automatically synthesized from VHDL source code (VHSIC Hardware Description Language, Standard IEEE 1076). In this case, resolving coincidences by selecting those pulses that overlap at least in one clock cycle results in a coincidence resolution of $3\tau_{clk}$.

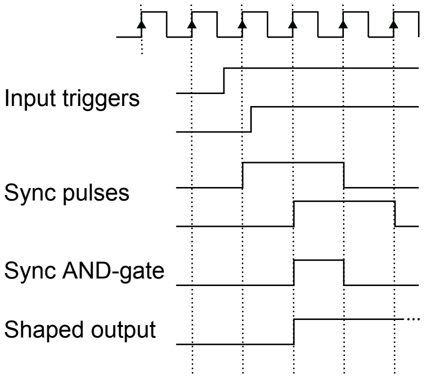

Figure 4.16: Timing diagram of the coincidence detection by synchronous AND-gating.

Being the minimum clock period τ a characteristic value of the target FPGA, the achievable maximum coincidence resolution is technology dependant. Low-end FPGAs typically support maximum clock rates up to 320 MHz, which corresponds to a minimum resolution of $\tau = 3$ ns. This means that even with these FPGA it is possible to achieve coincidence resolutions of 9 ns. With new generation FPGAs, like the Stratix III (Altera Corp., San Jose, CA, U.S.A.) mounted on the QPEM main board, we expect to achieve even better resolutions. In fact the maximum clock rate for new devices already exceeds 600 MHz, and we might expect coincidence resolutions in the range of 5 ns, with this simple technique.

In fact, a big advantage of this approach is that it is fully compatible with the QPEM architecture. By only disconnecting the coincidence and randoms triggers, we are capable of resolving coincidence using only the CFD inputs. Moreover, the time required to resolved coincidences is reduced to a few clock cycles, thus allowing for shorter, or even no analog delay lines to be mounted on the DAQ boards.

Finally, modern FPGAs include internal analog delays that can be used to equalize trigger paths, thus removing timing bias in the coincidence window.

4.2.5 Improving the timing resolution of the synchronous coincidence processor

The coincidence detection technique proposed in the previous section allows to achieve a coincidence resolution of $3\tau_{clk}$, where τ_{clk} is the minimum clock period available in the target FPGA. The multiplicative factor 3 is a direct consequence of the fact that a finite fraction of coincident event pairs, that trigger with even infinitely short delays, are due to be registered within two

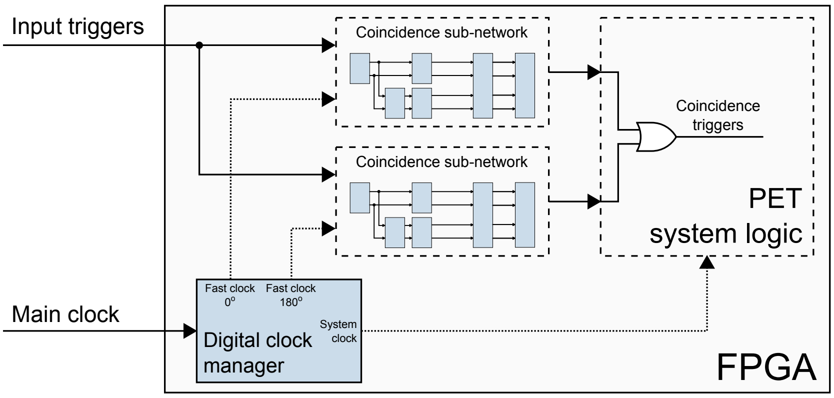

Figure 4.17: Schematic diagram of the dual synchronous coincidence network.

subsequent clock periods. In fact, if we resolved as coincident events only those events that were registered within the same clock cycle, we would obtain a coincidence resolution τ_{clk}, but we would lose a significant fraction of the events. However, it is possible to recover the loss fraction with an alternative approach. In fact it is possible to replicate the coincidence network inside the FPGA, and feed the second one with a phase shifted clock. If the phase shift is 180°, we can assert that two events separated by a delay $d < \tau_{clk}/2$, fall always within the same clock cycle at least in either one of the two networks. A variable fraction of events with separation $d \in (\tau_{clk}/2, \tau_{clk})$ will also be detected as a coincidence. Therefore, we could imagine this kind of *dual-coincidence processor* as the OR-combination of two sub-networks, as in Figure 4.17. This method is particularly convenient considering that modern FPGAs, even low-end ones, have internal resources that allow to produce a 180° phase shifted clock. However, internal phase shifting circuitry usually can handle clock frequencies lower than the one adopted by direct clock buffers. For example, Xilinx Spartan3E allow a maximum clock frequency of 320 MHz, but only 200 MHz are supported by the phase shifting components. As a result, the maximum obtainable coincidence resolution within this device is $\tau = 1/200$ MHz $= 5$ ns.

At this point, if we want to reduce the coincidence detection uncertainty for those events separated by $d \in (\tau_{clk}/2, \tau_{clk})$, we can double once again the number of coincidence network, and feed each one with four different phases, i.e. 0°, 90°, 180° and 270°. If we then take the AND combination of contiguous phases, i.e. $0° - 90°$, $90° - 180°$, $180° - 270°$, $270° - 0°$, we will have a series of outputs, at least one of them triggering whenever two events are separated by $d < 3\tau/4$, while the number of detected coincidences

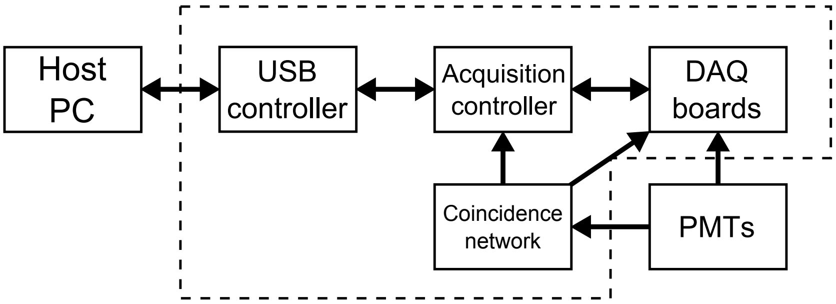

Figure 4.18: QPEM acquisition architecture diagram.

is variable only for those with $d \in (3\tau_{clk}/4, \tau_{clk})$. As a result the bell-shaped detection efficiency characteristic will have a slightly higher Full-Width Half-Maximum (FWHM), but steeper edges. We refer to this kind of component as a *quad-coincidence processor*. Unfortunately Spartan3E based prototypes have no sufficiently flexible digital clock managers that allow four phases at high clock speeds. However, the quad-processing concept it is expected to be applicable to the final, StratixIII based prototype.

4.3 The control unit architecture

In the execution of the thesis, a significant portion of the time has been devoted to the actual implementation of the complete system. This includes a clear specification document, that allowed starting peripherals development, while still designing the device architecture.

The main aim was to obtain a communication architecture diagram, and the definition of required board I/O channels and standards, power voltages and on-board devices. The initial conceptual diagram is shown in Figure 4.18.

In the communication architecture diagram the main components are the *Host PC*, *Acquisition Controller* and the *Coincidence network*, each one initially representing an independent electronics sub-system. Due to the use of a FPGA for the Acquisition Controller and the introduction of the synchronous coincidence processing approach, both have been later integrated into a single *Control FPGA*. However, this affects only the first stage of coincidence detection and does not change the overall streaming operation concept.

The Host controls every action and acts as Master device: it configures the boards, sends requests and records acquired data to disk. The USB controller serves as gateway between the mainboard and the Host. A custom device driver allows the communication between the Host Operating System and the controller chip. From the Control FPGA, the USB controller is seen as a set of FIFO memories. An OUT FIFO will is used to send control data from Host to FPGA, and two IN FIFOs are used to read acquired and status data from FPGA to Host. The Control FPGA acts as Master device in the mainboard, controlling the DAQ boards, the generic I/O and inputs from the coincidence board.

The USB controller of choice is a CY68013A FX2LP (Cypress Semiconductor, San Jose, CA, U.S.A.) particularly convenient for its ease of configuration and common diffusion in custom USB based devices. In fact, the FX2LP is provided with generic drivers and a convenient Host-side API to quickly start up a communication procedure, and a slave synchronous FIFO interface to the FPGA-side. A scheme of the USB/FPGA communication interface is shown in Figure 4.19. Being configured the EZ-USB controller as a slave fifo, from the FPGA it can be seen simply as a I/O conduit towards the host.

The EZ-USB controller must be configured to have three double buffered 512 bytes-deep endpoints. One with OUT direction and two with IN direction. The three corresponding FIFOs are be addressed by the FIFOADR[1:0] lines and controlled with the programmable FLAGx signals. A full control of the EZ-USB slave FIFOs in both read and write directions requires 27 pins.

The Control FPGA is responsible for controlling all onboard devices and routing data from the DAQ boards to the USB. Due to considerations on speed, memory, logic constraints and general experience, we chose a Stratix III FPGA (Altera Corp., San Jose, CA, U.S.A.).

4.3.1 Operation concept

Each PMT is connected to a corresponding CFD (Section 3.4), which is in charge of generating a digital pulse with a well defined delay after a gamma arrival and light scintillation in the detector. The digital pulses (PMTxA and PMTxB) are routed through an OR-AND network to generate the CDxA,B signals (shortly CDx) which are asserted every time two light pulses arrive in coincidence, and the DDxA,B which are asserted when two light pulses arrive with a fixed separation delay, thus being counted as random coincidences. CDx signals are the designed triggers to start voltage sampling in the data acquisition boards. In the first version with an external coincidence network, they were routed to the Control FPGA (CF), together with DDx and PMTx, to let it keep track of DAQ boards status and compute activity and detection statistics. With the embedded synchronous coincidence processor, they are generated within the FPGA directly from the PMTx inputs.

A set of rules can be defined to allow coincidence acquisition, pile-up, and

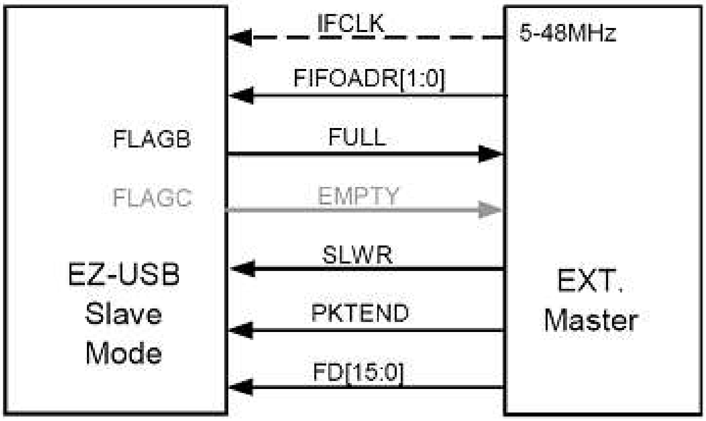

Synchronous FIFO writes

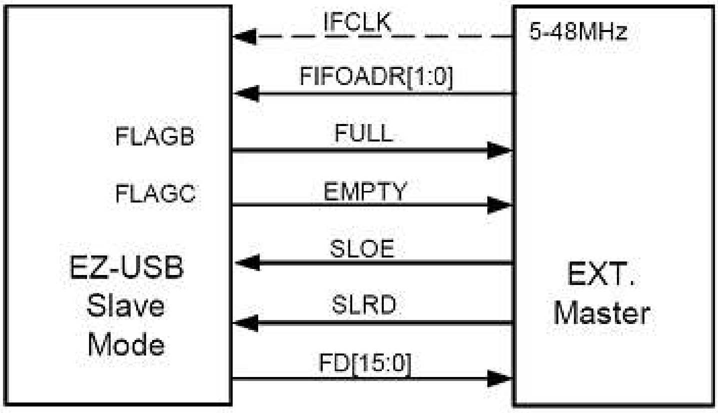

Synchronous FIFO reads

Figure 4.19: Scheme of the USB/FPGA communication interface.

multiple coincidence correction and event labelling. These rules are coded in proper finite state machines inside the CF. If predefined rules determine that the event has to be acquired, the acquisition triggers are forwarded to the corresponding DAQs. Every time a DAQ acquires an event, it stores its data into a built-in FIFO, and waits for another trigger. The CF continuously empties DAQ-FIFOs and transmits their contents to the Host multiplexing at specified rates statistics and status data.

By properly changing the control rules and the combinatorial circuit of the coincidence network is possible to operate in SPECT mode, i.e. to acquire every single events. These modifications can be programmed into the FPGA together with the PET logic, thus making possible to switch between modalities at run-time.

4.3.2 Architecture of the processing core

Main processing tasks consist of data transfer management, event tracking, configuration and status control. A simplified scheme of main FPGA firmware is reproduced in Figure 4.21. Event processing has been divided into two main stages in pipeline: the traffic controller (TC) and the acquisition processor (AP). This kind of pipelining maximizes the efficiency of data retrieval from the DAQ boards, and allows for more complexity in the digital processing part of the AP. The AP consist of a common container interface, in which different dedicated controllers, i.e. PET, SPECT, calibration and debug acquisition controllers, can be switched in run-time. In this way we can exploit at best the timing budget for each acquisition modality, at the cost of mayor logic resources usage. An event journal (EJ) is the only interface between the AP and the TC. The AP, according to a set of programmable rules, processes incoming triggers from the coincidence network, generates the outputs that trigger interested DAQs, and writes event records into the EJ. Each record contains information on pile-ups, scattered and random coincidences. The TC reads these records, retrieves acquired data from DAQ buses and merges the event record information. This kind of real-time data manipulation implies various advantages. Acquisition policies can be implemented in the firmware in a modular manner that minimizes the dead time in terms of clock cycles per event. Moreover, new conditions and experimental behaviours can be easily ”plugged” in the current state machines. Digital filters can also be inserted, in the TC-AP path, in order to alleviate off-line processing, without affecting dead time or data throughput. For example, energy calibration and pixel identification can be done on-line.

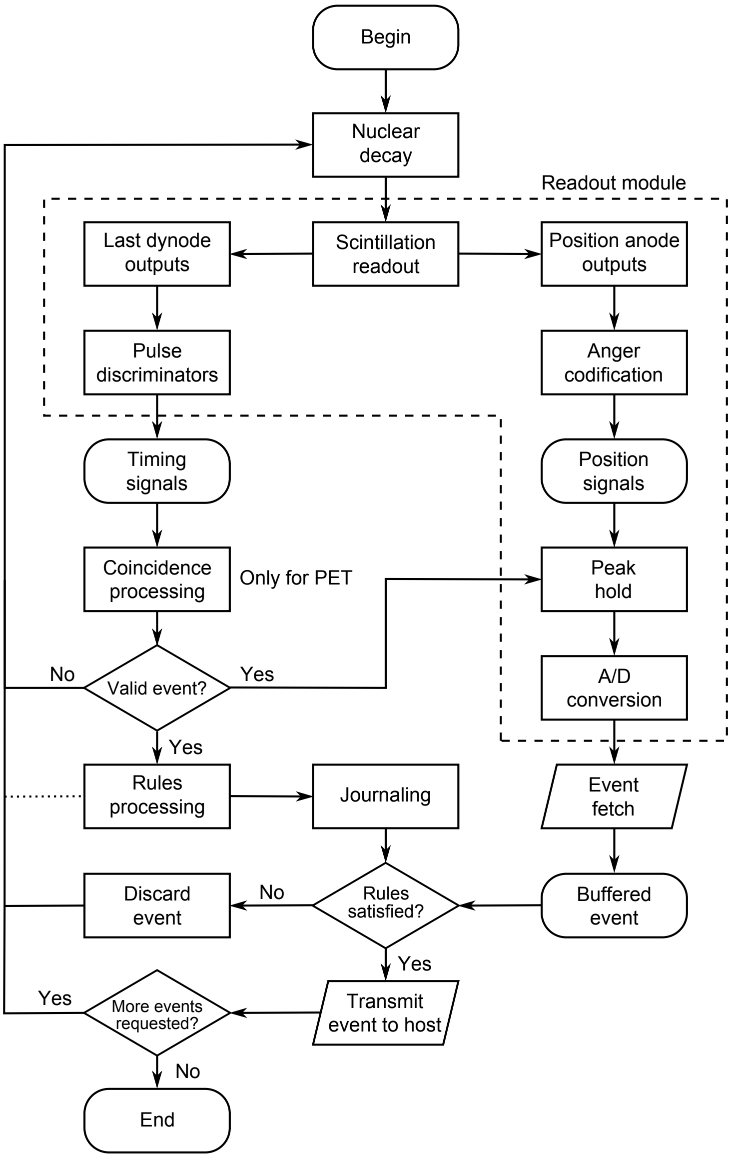

Figure 4.20: Flow diagram of the acquisition protocol. The fetching process is buffered and synchronized by the journaling system.

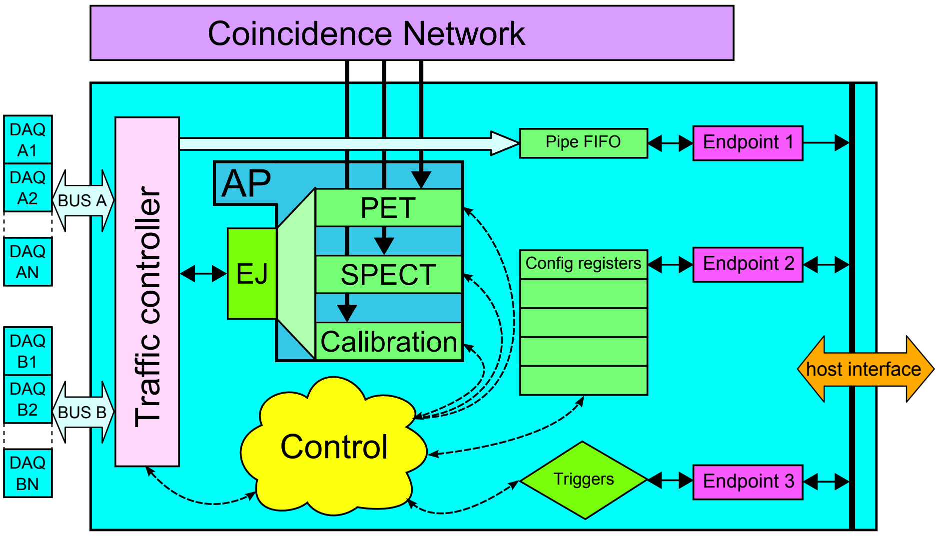

Figure 4.21: Simplified scheme of the firmware architecture.

4.3.3 Acquisition rules

Whenever a DAQ receives a trigger, it starts an event acquisition entering in a dead time interval, which corresponds to the time needed by the DAQ board to sample pulse voltage and reset. After the DAQ resets, it informs the CF that it is ready again with a falling-edge of the busy signal. Whenever the CF sends a trigger to the DAQ, it registers that the corresponding DAQ is currently busy. In order to to guarantee a correct and clean execution, the following set of rules must be respected.

1. Event acquisition permission: a DAQ can acquire only if the corresponding enable signal is asserted.

2. Pile-up rejection: if a coincidence trigger applies to a free DAQ, but also to a busy one, the CF must reject the acquisition of both DAQs. This condition can be called *post-pileup*, because the pileup condition happens *after* the coincidence acquisition has started. Moreover, a timing counter must be kept in for every incoming single in order to guarantee that a coincident pair does not overlap on a previous pulse. If that happens, the coincidence acquisition must be inhibited. The timing counter must be parametrizable. In analogy with the previous condition, we refer to this one as *pre-pileup*.

3. Multiple coincidence correction: if three or more PMTs are coincident th CF must decide depending on current configuration, whether to reject or acquire all events.

4. Spare coincidence rejection: it may happen, due to race conditions, that the coincidence network outputs a single coincidence trigger. This is an unavoidable behaviour and must be rejected when it happens, or recovered using single triggers information.

5. Event labelling: every time a new event triggers, increment a 6-bits event identifier that DAQ read and associate to recorded data. The identifier is used to counter-check DAQ-FIFOs with CF trace. This kind of event checking has been important in the development phase in order to control buffer overruns and generally a correct data streaming.

Apart from degrading physical conditions, a flow control protocol has been implemented in order to timely detect and prevent acquisition errors. The flow control is applied at two levels: single event integrity control and coincidence integrity control. The single event integrity is guaranteed by 3-bits wide signature prefixes in each asynchronously transmitted word, the coincidence integrity is monitored using a 6-bits marker in each single event packet (Figure 3.16). Whenever two DAQ boards are triggered, they receive a common event marker, that is later counter-checked to guarantee that the two single events where correctly paired. Error control is performed in real-time by the internal logic of the Control FPGA, which can be programmed to automatically recover any synchronization loss by resetting DAQ state-machines within a interval of a few milliseconds.

4.3.4 Events data streaming

Whenever a coincidence is detected, two DAQs are triggered to acquire the two coincident photons. We define a *single event* as the data associated to one of those photons. A *double event* is the data associated to the coincidence and is obtained just coupling two single events. When a DAQ is triggered, it enables four peak detectors (Figure 3.12) and starts the digital conversion of voltage peaks received from the analog frontend within a predefined, programmable, timing window. The four digital values are then packed and labelled with the DAQ id (DPSW), the event id (MRK), the delayed coincidence flag (DCO), four event flags for future use and redundant information for stream flow control. The single event packet structure is shown in Figure 3.16.

It is task of the traffic controller to fetch single events, pair and write them into the streaming FIFOs.

The events streaming mechanism has been implemented introducing the concepts of *block* and *frame* (Figure 4.22). A stream is made of several

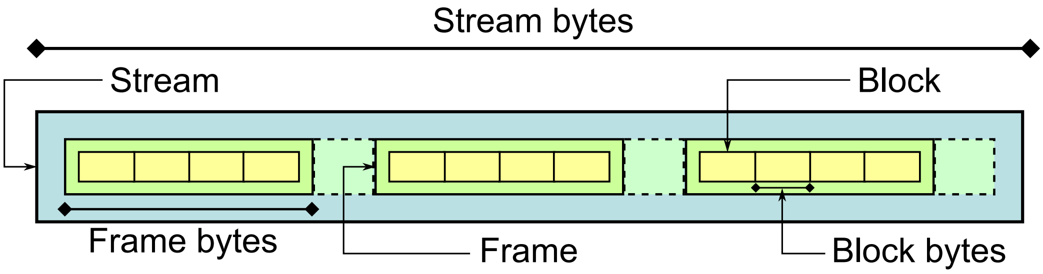

Figure 4.22: Data stream structure. A stream is made of an unlimited number of frames, which in turn are made of blocks. The frame and block maximum sizes are 16.776.192 and 1024 bytes, respectively.

frames. The number of frames has theoretically no limits. A frame corresponds to an API read call to the USB driver. Its maximum size is dictated by driver memory limitations and in the current implementation corresponds to 16.776.192 bytes. Each frame is composed of an integer number of blocks. Block size must be even and its maximum is 1024 bytes. A block corresponds to the data packet that the USB chip can handle in an efficient atomic way. Finally, a block is composed of an integer number of double events, of 20 bytes each.

From the host point of view, the only required parameters to stream data are the total stream size and the frame size. From the device point of view, the only required parameters are the total stream size and the block size. The block size must correspond to the minimum amount of acquired bytes ready in an internal FIFO, that allow to start a synchronous uninterrupted data transfer.

A time-driven acquisition, in which the acquisition length is defined in units of seconds instead of bytes has not been implemented yet.

4.3.5 Statistics data acquisition

In order to provide the statistical information required by the MLEM based reconstruction algorithm, part of the instrumentation must be dedicated to event counting on real-time. Coincidence, delayed, pile-up rates and losses tracking are useful information that can be used to enhance the reconstructed image. The idea is to use the internal FPGA resources in order to implement digital counters triggered by a set of more or less complex rules controlled during the acquisition. The counters values will be then streamed through a parallel data channel. The non-blocking multi-threaded acquisition protocol discussed in Section 4.1.2 is particularly suitable for this kind of stream multiplexing and the circuitry required to implement event counters is easily integrable within FPGA processing modules. In the next section, the required data analysis and correction procedures will be explored in order to define a comprehensive set of the statistical information that have to be collected during PET acquisitions.

4.4 Acquisition output

The software to be used for the final version of the QPEM scanner it is an extended version of the same used for the DAQTB prototypes. It has been designed to allow multi-threading operation to support the reading protocol in Figure 4.9.

Depending on the performed acquisition modality, the software application can produce different output files. In the calibration acquisition, the only result is a binary file containing a set of fake-triggered events acquired with photomultipliers turned off. In this way, the Anger voltages acquired by the peak detectors are always pedestal voltages. The application can extract mean values from the file thus deriving pedestal values, as described in the following chapter. In PET acquisition mode, two files are produced: an event file and a statistics file. The event file is a list of double events with the same binary format illustrated in Figure 3.16. The statistics output is a file containing per-frame information required for data analysis and image reconstruction. In the current version the following statistics are collected:

- Frame start and end time from the beginning of the acquisition in ms.
- Single rates on each detector module
- Coincidence rates on each detector module pair
- Delayed coincidence rates on each detector module pair
- Single delayed rates for innovative random mode
- Multiple coincidence rates
- Loss rates and counters separated for loss cause
    - DAQ dead time
    - Host traffic dead time
    - AP Finite State Machines (FSM) dead time
- Overflow flags for each count and rate value

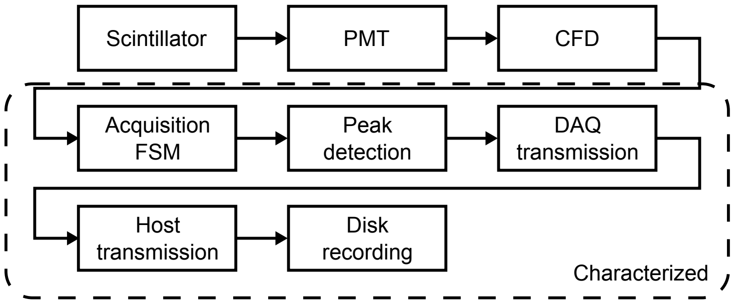

Figure 4.23: Block scheme of components involved in events acquisition that are affected by distinct causes of loss. The components rounded with a dashed line are self characterized during the acquisition process.

Statistic activity rates and loss counts are generated from the input triggers. Their value is collected to quantify the acquisition efficiency and estimate the dead time. The estimation is done by comparing the measured rates with data that has been actually recorded to the Host. With this regard, it is important to note that the comparison between the input and output rates of the model we derive to estimate our losses, can only be used to characterize the efficiency of the synchronous digital acquisition system, which indeed is designed and expected to be very low. The total dead time of the acquisition system, however, will be strongly affected by the contribution of the constant fraction discriminators, which must be characterized and optimized separately. A scheme of the blocks involved in the acquisition that introduce dead time losses is reported in Figure 4.23

Chapter 5

Data analysis and correction

The result of a complete PET/SPECT acquisition is a calibration, a statistics and a list-mode events file. Starting from these files, a series of data manipulations and corrections must be done in order to obtain the planograms required by the reconstruction algorithm. The whole process is illustrated in the flow chart in Figure 5.1.

5.1 Calibration process

5.1.1 Pedestal calculation and position decoding

The first step is the pedestal calculation. This operation is done by the host application, which takes as input the calibration file and outputs a XML (Extended Markup Language) pedestals file. Pedestal values for each ADC channels are necessary to decode Anger signals into module spatial coordinates. This is because it is necessary to remove the baseline in order to maintain the linear relationship between the four Anger coordinates converted by the DAQ board (see Section 3.7). Given that the modular geometry is intended to be kept flexible, pedestal information per channel must be flexible as well, therefore the XML structure. The effect of a wrong pedestal restoration leads to crystal identification errors, as it may be understood from the flood maps of Figures 5.2 and 5.3.

Once the pedestal value has been calculated, the event hit coordinates within the detector module can be decoded from the four Anger signals (XA,XB,YA and YB), with the following equations:

$$XA = TAXA - PDXA$$

$$XB = TAXB - PDXB$$

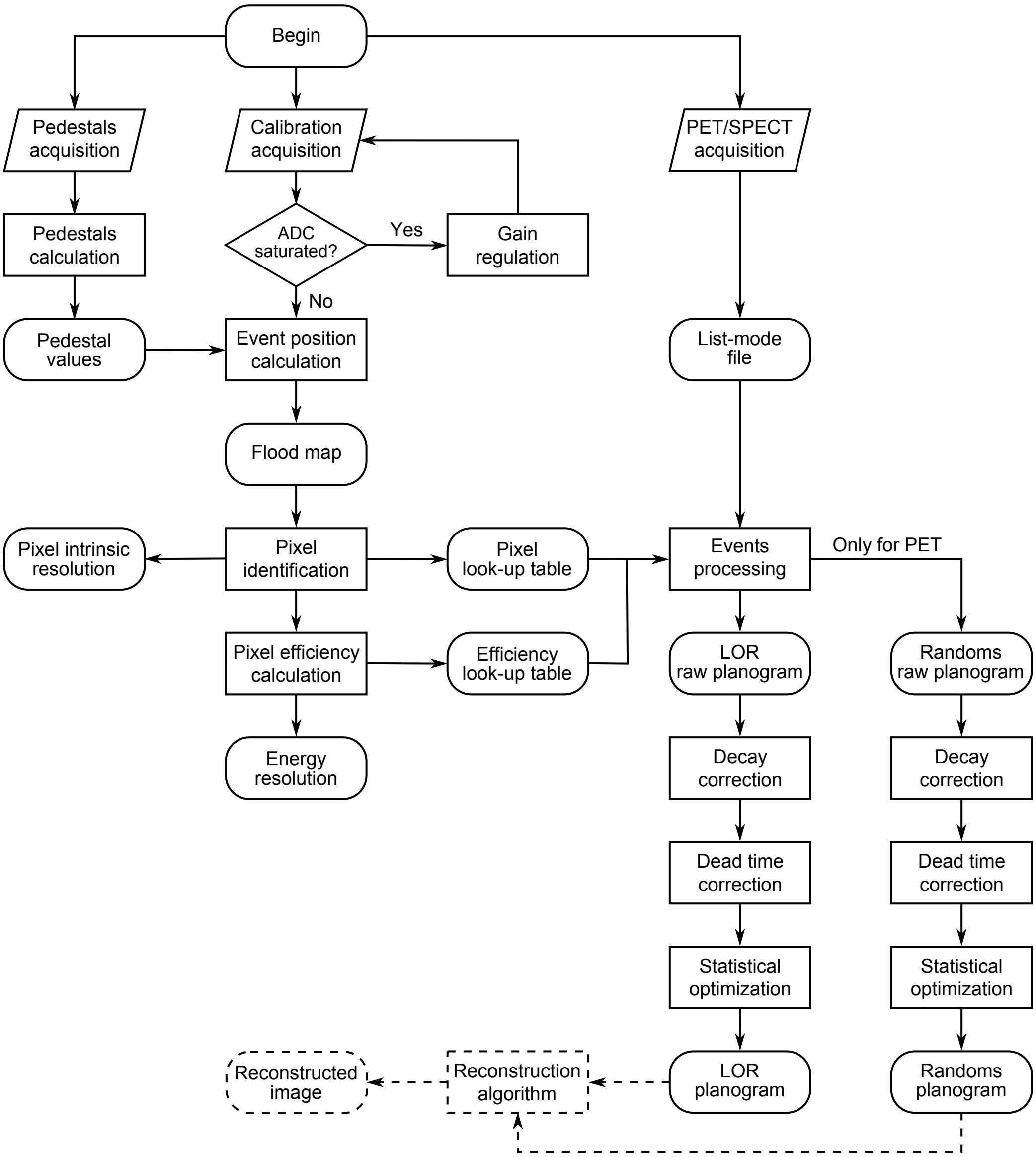

Figure 5.1: Flow chart of the PET/SPECT calibration and acquisition process. Rounded boxes represent deliverable or intermediate data structures.

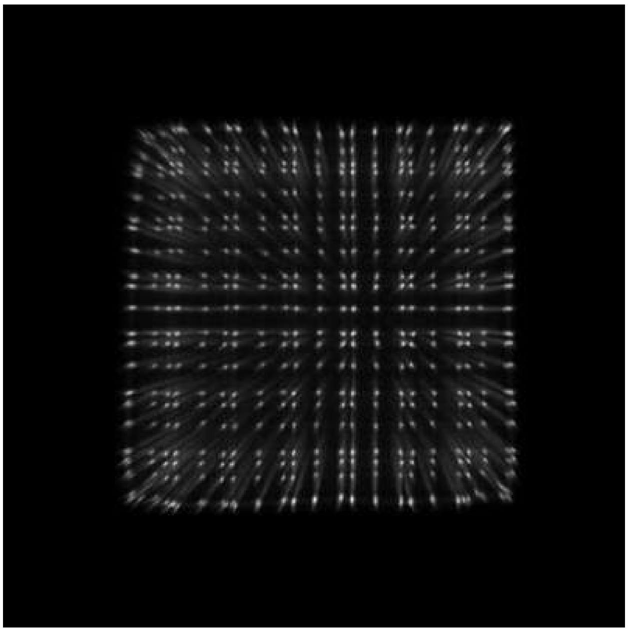

Figure 5.2: Effects of a wrong pedestal restoration on flood maps.

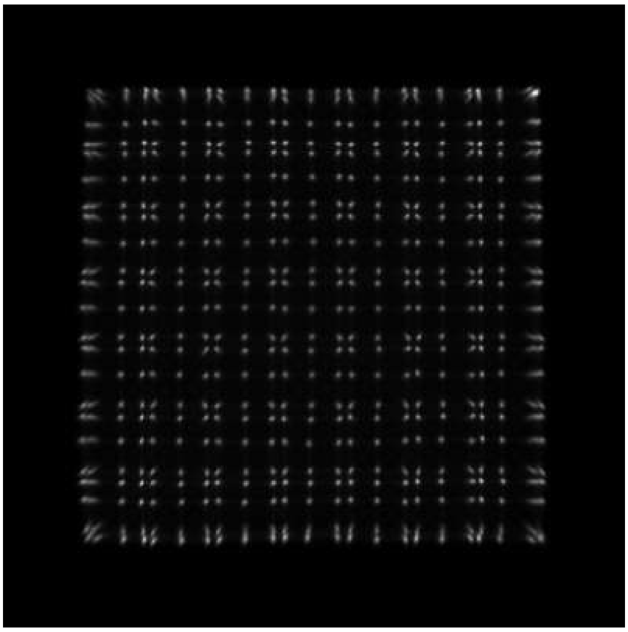

Figure 5.3: The same flood map as in Figure 5.2 with a correct pedestal restoration.

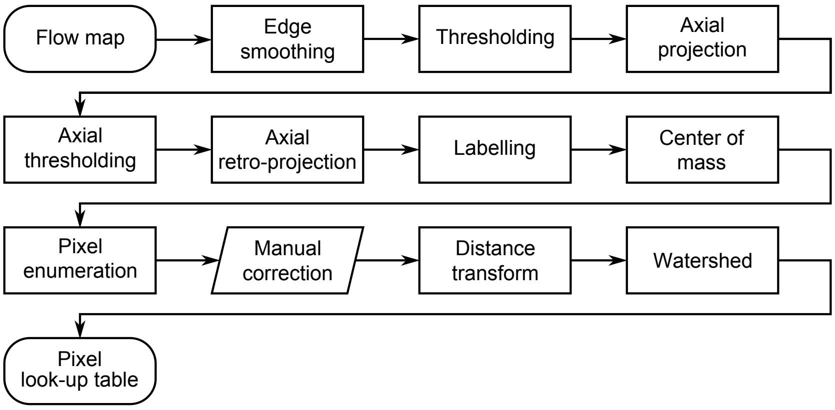

Figure 5.4: Flow chart of the pixel identification semi-automatic process.

$$YA = TAYA - PDYA$$

$$YB = TAYB - PDYB$$

$$X = \frac{XA - XB}{XA + XB}$$

$$Y = \frac{YA - YB}{YA + YB}$$

where $TA\{**\}$ are the digitized values stored in double events and retrieved by the front end, $PD\{**\}$ are the calculated pedestal values, $X\{*\}$ and $Y\{*\}$ are the Anger values, and X and Y are the hit point coordinates within a detector module.

5.1.2 Point discretization and pixel identification

The common practice in reconstructing tomographic images with pixellated scintillators is to group acquired events into two-dimensional bins that correspond to crystal elements. In order to identify pixel location of individual pixels, a preliminary calibration PET acquisition must be done with a planar source. From this acquisition a flood map is generated, as in Figure 5.3. The map is then segmented with a semi-automatic process, diagrammed in Figure 5.4, based on image centroids detection and watershed algorithms. The result of map segmentation is shown in Figure 5.5.

The segmented flood map is then used as look-up table to rebin acquired events, as shown in Figure 5.6.

The pixel map has no direct correlation with image reconstruction, apart from its use for the generation of a pixel look-up table, and for this reason it is not stored in the hard disk. However, it is useful in order to detect possible

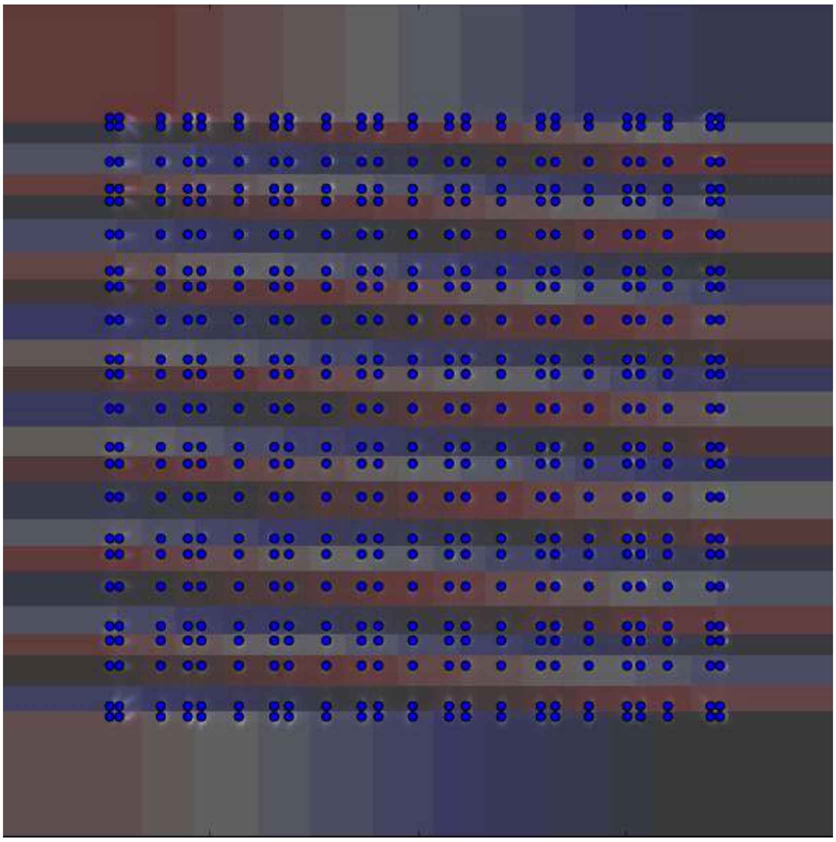

Figure 5.5: Segmented flood map.

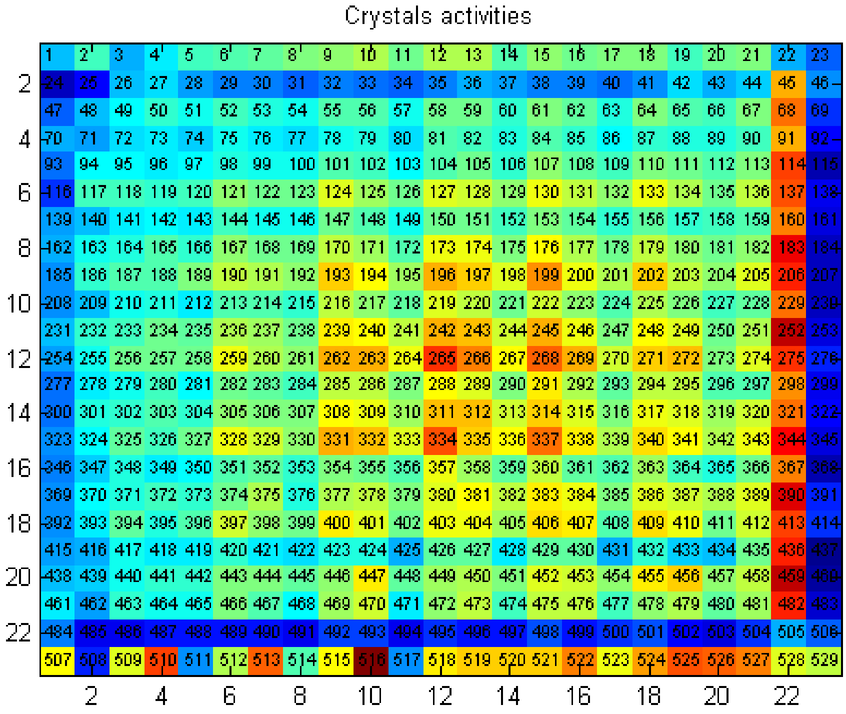

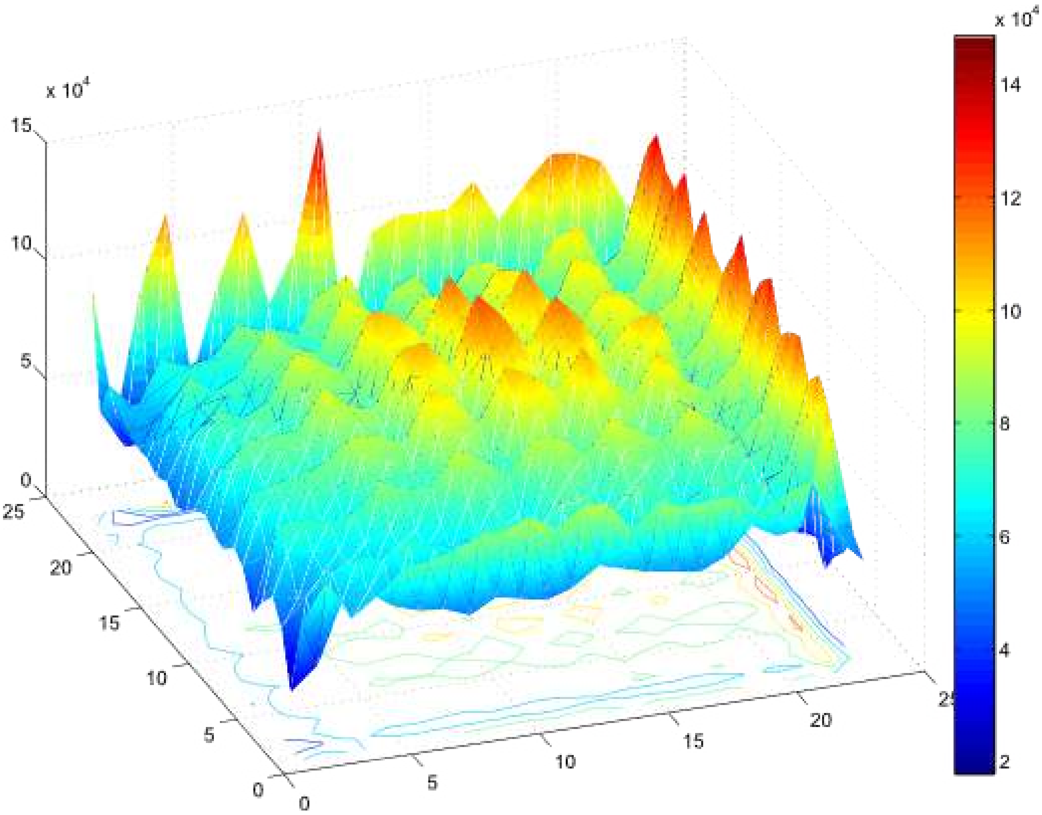

Figure 5.6: Rebinned flood map of a 23 × 23 LYSO crystal array. The image shows how pixel identification at borders works badly because of higher encoding noise.

problems, as for example in pixel identification algorithm. Moreover, the same process used for pixel map calculation is used for energy correction process and planograms generation, as discussed in next sections.

5.2 Energy correction

With energy correction we refer to the process of transforming acquired values to energy-related values. Energy correction is applied in order to discard those low-energy events that probably suffered scattering or that were not product of a positron annihilation. Typically used energy windows are $350 \div 700$ keV. Generally speaking a wider energy window can improve system sensitivity, while narrower windows would improve spatial resolution. For this reason the energy window is left as a degree of freedom to be tuned during image reconstruction.

In order to filter events depending on their energy, the raw ADC output range must be referred to the real energy range of acquired photons. For any deposited energy the resulting Anger voltages can change slightly between different crystal pixels, therefore it is important to establish the conversion factor on a per-pixel basis. We call this conversion factor *pixel efficiency* χ and the conversion formula is the following:

$$E_i = E_{ADC} \cdot \chi(i) \tag{5.1}$$

where i is the index of the interested pixel element, E_i is the energy in keV and E_{ADC} is the integer ADC output.

Calculating pixel efficiencies is a process that requires two steps. The first step consists in deriving energy histograms on each pixel i, the second is a Gaussian fitting by which we identify the ADC channel $k(i)$ corresponding to the 511 keV peak. The pixel efficiency is

$$\chi(i) = \frac{511}{k(i)}\,[keV] \tag{5.2}$$

Once the pixel efficiency has been calculated, it is possible to determine the global energy histogram and resolution by summing energies of all acquired events. Figure 5.7 and 5.8 show the raw and converted energy histograms for a pixel at the centre of the flood map. A long tail can be appreciated in the obtained histogram, that we address as an effect of the optical absorption on the scintillating crystal. This effect has been previously studied an simulated for the used detector modules [Bonifacio09].

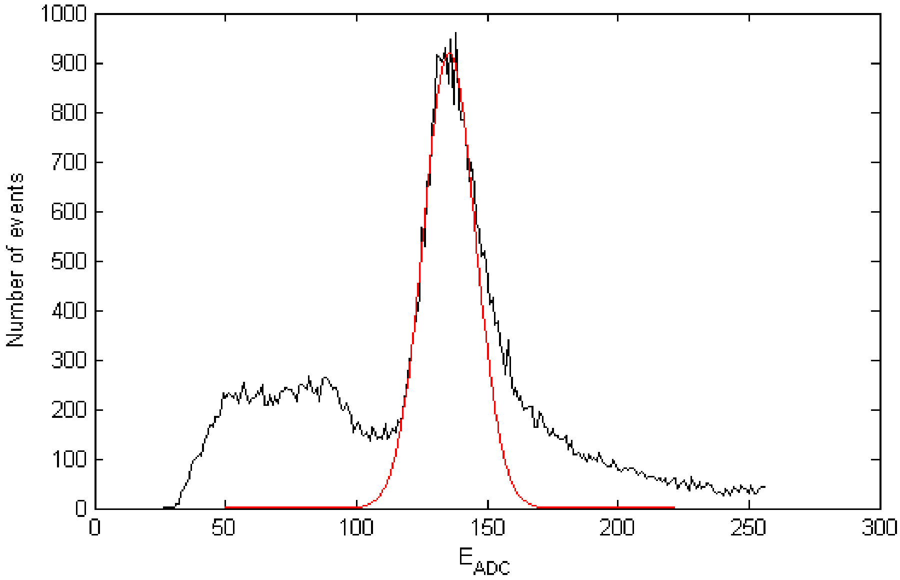

Figure 5.7: ADC channels histogram of a pixel element for a FDG source. The long tail is addressed as an effect of the optical absorption in the scintillator [Bonifacio09].

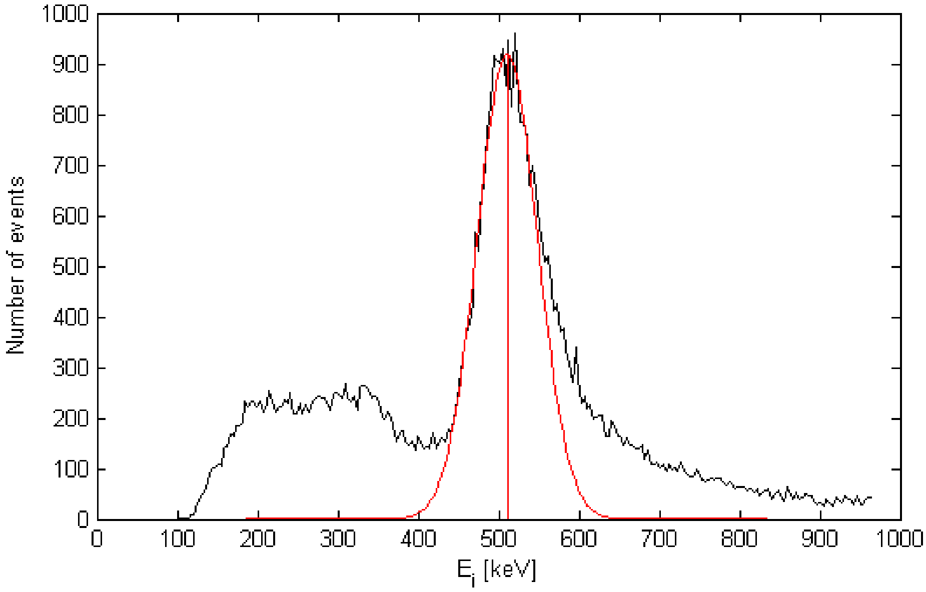

Figure 5.8: Energy histogram of a pixel element for a FDG source. The abscissa conversion has been done by dividing the ADC channels by the value of the channel under the peak mean μ and multiplying by 511 keV

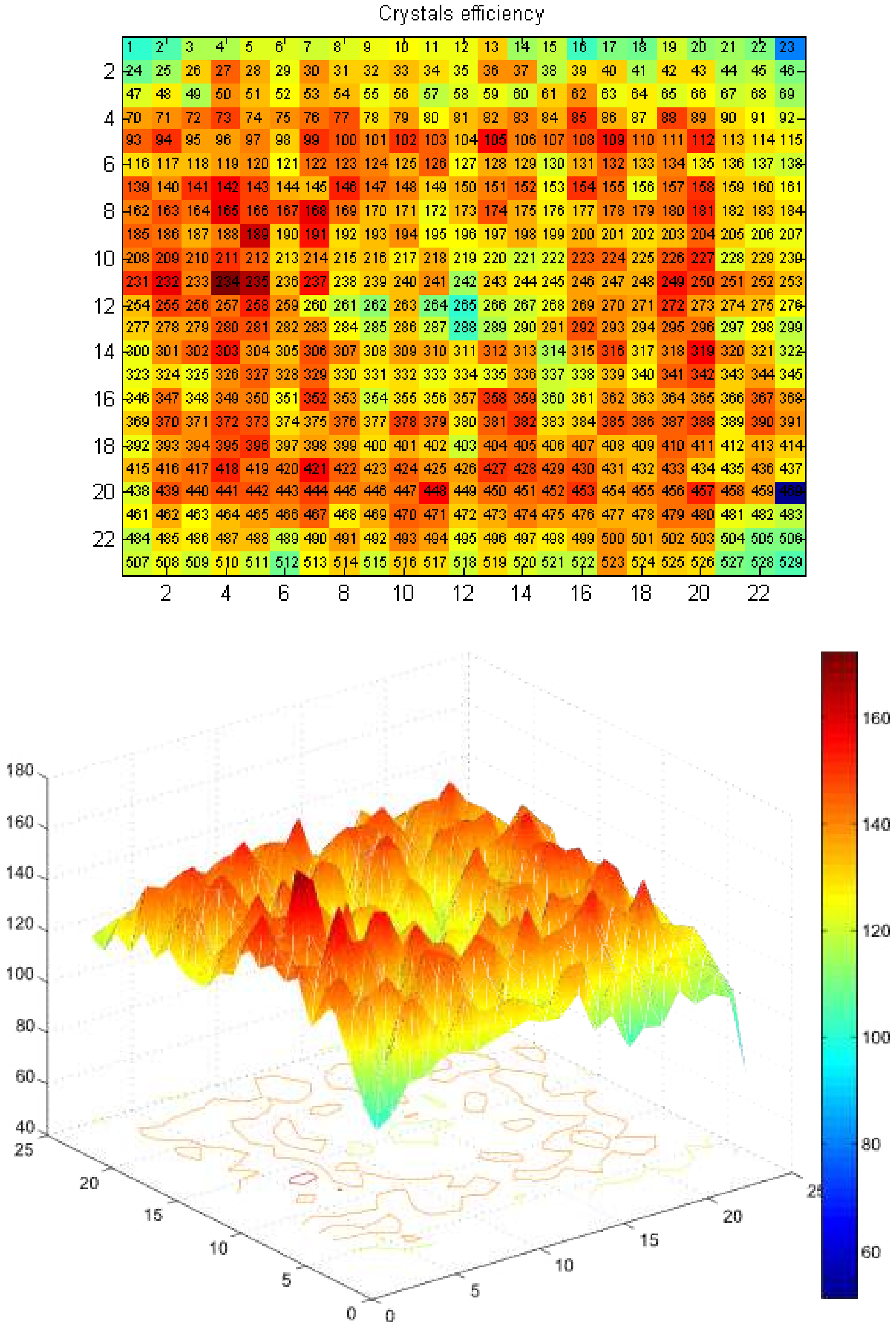

Figure 5.9: Pixel efficiency map of a detector module.

5.3 Event rate correction

As introduced in Chapter 2, the typical input to a reconstruction algorithm is a planogram. Each planogram element must correspond to the line integral of the positron decay radioactivity thorough one of the possible lines of response (LORs). Coincidence rates are the used approximation to such line integrals. In order to derive coincidence rates over all the possible crystal pairs we perform a per-frame conversion of integral data into activity rates. The conversion is achieved dividing the event counts by the time interval registered in the statistics file:

$$c_{lm,pq} = \frac{n_{lm,pq}}{\Delta t} \tag{5.3}$$

where $n_{lm,pq}$ is the number of coincidences acquired in the interval Δt between the crystal element p of module l on one side and the element q of module m on the other side, and $c_{lm,pq}$ is the activity rate between the same elements.

However, a series of corrections must be worked out in order to guarantee a correct reconstruction in the most general case. Inaccurate or missing correction of non-linearities and non-uniformities present in PET can lead to artefacts in reconstructed images and are undesirable for comparisons of activity levels in different organs or in diseased versus normal tissues. Correction is also essential for dynamic studies, such as those conducted in dosimetry. In the following sections the correction procedures that are applied to raw rates prior to the planograms generation will described.

5.3.1 Decay correction

Under the assumption that the frame duration is much smaller than the decay time we can approximate the decay corrected counts within a frame with the following formula:

$$n'_{lm,pq} = n_{lm,pq} \cdot e^{\frac{t_i}{\tau}} \tag{5.4}$$

where t_i is the end time of the frame i and τ is the decay time of the radioisotope.

In typical conditions, a frame does not last more than few seconds, thus making the approximation usually valid. However, in the more general case the decay correction formula is as follows:

$$n'_{i,lm,pq} = n_{i,lm,pq} \cdot \frac{t_i - t_{i-1}}{\tau \cdot \left(e^{\frac{-t_{i-1}}{\tau}} - e^{\frac{-t_i}{\tau}}\right)} \tag{5.5}$$

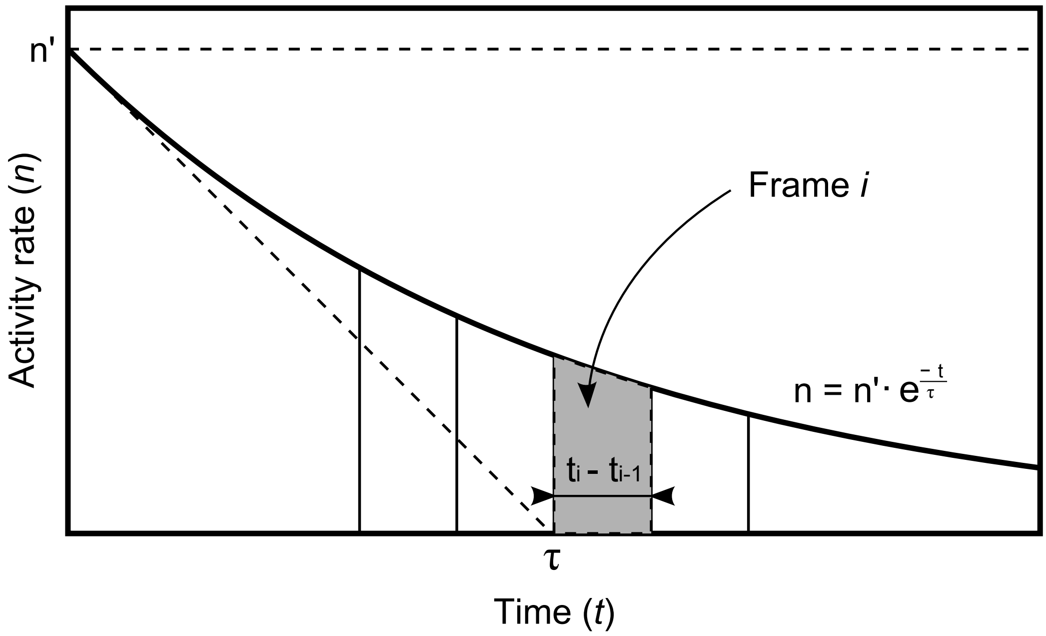

Figure 5.10: Activity rate versus time. If the frame interval $t_i - t_{i-1}$ is much smaller than the isotope half-life, the decay corrected counts n' can be approximated as $n \cdot e^{\frac{t_i}{\tau}}$.

which can be derived solving the integral expression of isotope exponential decay (Figure 5.10):

$$n_{i,lm,pq} = \frac{\int_{t_{i-1}}^{t_i} n'_{i,lm,pq} \cdot e^{\frac{-t}{\tau}}\, dt}{t_i - t_{i-1}} \tag{5.6}$$

This formula can be useful when imaging low radioactivity profiles coming from fast decaying isotopes, such as ^{15}O.

5.3.2 Dead time correction

There are at least three different dead time sources, each one introducing its contribution to events losses:

- Dead time of the core processor
- Dead time of the CFD
- Dead time of the peak detectors

In order to correct for the dead time, the introduced losses must be quantified. We can start considering that processor dead time is negligible with respect to peak detectors, because the most of processor's time is spent waiting for the DAQ boards to finish peaks acquisition.

An evaluation of CFD losses could be then done with the two-source method [Evans55,Cherry03]. This method is a simple but satisfactory method for measuring the resolving time of single-channel counting devices. It consists in comparing the response of the device to the radiation to two approximately equal sources, taken separately and then taken simultaneously. The counting rate for source 1 is determined, R_1. Without disturbing the position of source 1, source 2 is placed in position for counting and the counting rate for the two sources together is determined, R_{12}. Then source 1 is removed, without disturbing source 2, and the counting rate for source 2 alone is determined, R_2.

If the system is non-paralysable, as is the case for CFDs, the dead time τ_n is given by

$$\tau_n \approx (R_1 + R_2 - R_{12})/(R_{12}^2 - R_1^2 - R_2^2) \tag{5.7}$$

If the system is paralysable then

$$\tau_p \approx [2R_{12}/(R_1 + R_2)^2] \ln [(R_1 + R_2)/R_{12}] \tag{5.8}$$

Given that CFD's dead time is of the order of few hundreds of nanoseconds, we expect related losses to be low at currently used radioactivity rates. In order to estimate losses due to peak detectors, i.e. those events that could not be acquired because one or both DAQs corresponding to the interested modules were busy, we compare the trigger rates R_t stored in the statistics file, which are a lossless count of CFD outputs, with the actual acquired events $n'_{l,p}$. The dead time can be calculated from the expression of non-blocking losses [Wicks77, Hasegawa04]:

$$\tau_n = \frac{R_t - \sum\limits_{l,p} n'_{l,p}}{R_t \sum\limits_{l,p} n'_{l,p}} \tag{5.9}$$

The formula used to obtain the corrected activity rate is derived by simply multiplying the acquired rate by the inverse of the loss fraction:

$$n''_{l,p} = n'_{l,p} \cdot \frac{\sum\limits_{l,p} n'_{l,p}}{R_t} \tag{5.10}$$

5.3.3 Random events correction

In the current implementation, the actual random events correction is left to the reconstruction algorithm. However it is duty of the acquisition system to produce the required data structures to be passed to the algorithm. The simplest and most efficient way to provide such data is to generate a *random coincidences planogram.*

As described in the previous chapter, the QPEM scanner can acquire random events either in conservative or innovative mode. When collecting randoms in conservative mode, the machine stores in the listmode file random events as if they were true coincidences, but with a delayed flag turned on. The analysis application can then filter such events and generate a planogram of randoms rates $r_{lm,pq}$ in the same way it generates a planogram of true events $c_{lm,pq}$.

When using the innovative mode, a straight randoms planogram generation is not possible, because random events are composed of a single photon. In order to obtain an event list formally equivalent to a conservative acquisition, we could then combine orderly events coming from both detector sides. In principle, being the detection technique the same and given that in both cases the information relative to the event as a pair is fictitious, the resulting distribution should be statistically equivalent. Therefore this process would produce an equivalent randoms planogram.

However, a more elegant approach can be taken to demonstrate the equivalence between the two techniques and at the same time enhance the randoms planogram generation. The idea is to apply a recently published variance reduction technique to the sampled randoms counts [Watson09, Byars10]. Randoms variance reduction techniques are based on the theoretical relation between the random coincidence rate in a detector pair r_{ij}, and the single event rates in those detectors c_i and c_j:

$$r_{ij} = c_i \cdot c_j \cdot 2\tau \tag{5.11}$$

where 2τ is the coincidence time window. When all of the elements i on head A are in coincidence with all of the elements j on head B we can define

$$\begin{aligned} R_j &= \sum_i r_{ij} = \sum_i c_i \cdot c_j \cdot 2\tau = C_A \cdot c_j \cdot 2\tau \\ R_i &= \sum_j r_{ij} = \sum_j c_i \cdot c_j \cdot 2\tau = C_B \cdot c_i \cdot 2\tau \end{aligned} \tag{5.12}$$

Where R_j and R_i are the *double blind random distributions*, i.e., the spatial distribution of the single counts involved in a delayed coincidence (random single) on heads B and A, respectively, while C_A and C_B are the total singles count rate on head A and B, respectively. The above quantities have been defined in [Watson09] for conventional delayed window techniques. However, they are specially suitable to be applied to the innovative delayed technique, because in fact each one is function only of the event counts on a single detector side.

Following the mathematical development we find that

$$\begin{aligned} R_i \cdot R_j &= C_B \cdot c_i \cdot 2\tau \cdot C_A \cdot c_j \cdot 2\tau \\ &= (c_i \cdot c_j \cdot 2\tau) \cdot (C_A \cdot C_B \cdot 2\tau) \\ &= r_{ij} \cdot R \end{aligned} \qquad (5.13)$$

Hence,

$$r_{ij} = \frac{R_i \cdot R_j}{R} \qquad (5.14)$$

being Equation 5.14 the expression for the generation of variance reduced randoms planogram for both conservative and innovative techniques. The only difference between the two cases is that for conservative randoms we discard the pairing information, while for innovative randoms we directly count independent delayed rates at both detector sides.

In order to visualize the effects of the variance reduction and to compare conservative and innovative randoms distributions we realized the experimental setup illustrated in Figure 5.11. In the setup two FDG phantoms were used, a small one between the detectors and a bigger one outside the FOV, as a randoms-only source. The obtained images are shown in Figure 5.12.

As shown in Figure 5.12, the delayed coincidence distribution is very similar to that obtained with the new method. To numerically validate the equivalence of the two planograms an image correlation plot has been produced. The Pearson product-moment coefficient of the plot is equal to 0.94, which indicates good correlation [Rodgers88].

To evaluate the effectiveness of the proposed noise reduction technique we have performed an additional measurement where the source distribution shown in Figure 5.11 is replaced with a planar phantom (6 cm × 6 cm, 3 mm thick) filled with FDG and placed in the mid plane between the two detectors, parallel to the detectors surface, thus occupying all of the possible LOR. For this measurement only the new random estimation technique is implemented. Figure 5.13, left, shows the planogram obtained from the delayed window coincidences, where the number of counts in each LOR is obtained as usual. Equation 5.14 was applied to the R_i and R_j distribution directly obtained by

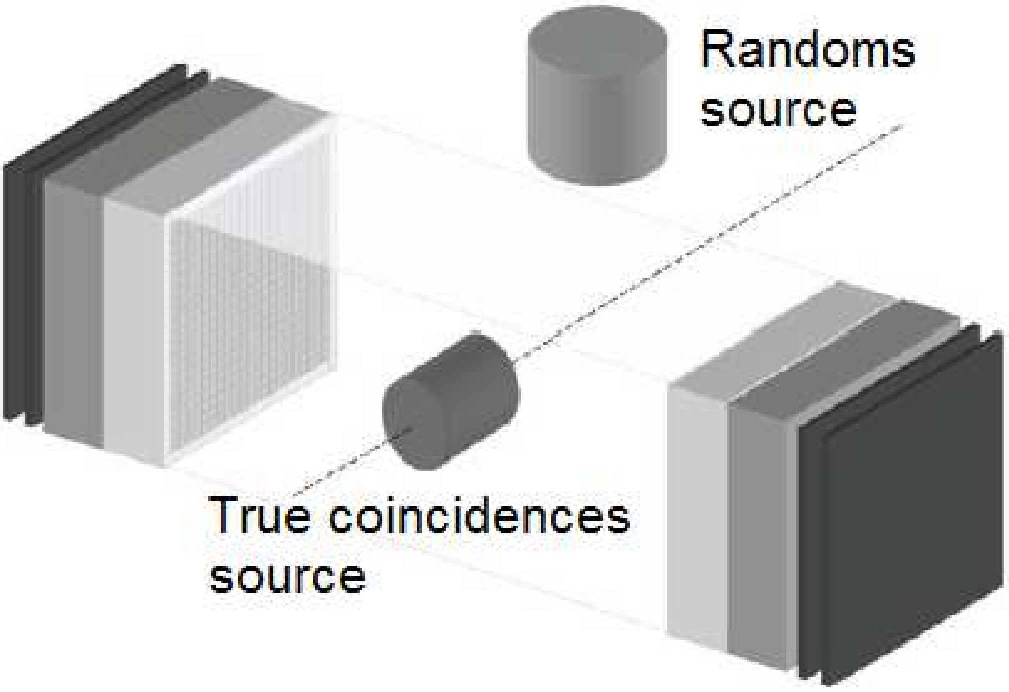

Figure 5.11: Arrangement of the detector heads and the distribution of the sources in the FOV. Head-to-head distance is 14 cm. A cylinder approximately 2.5 cm × 2.5 cm$\oslash$ filled with a FDG solution is positioned along the scanner axis in the first half of the FOV. Total activity in this cylinder is approximately 100 μCi. A larger cylinder mimicking an external background source is positioned outside the FOV. slightly off-axis. The total activity in the background is about 1 mCi.

analyzing the two heads separately. In this way, the noise reduced random distribution planogram was obtained (Figure 5.13, right).

Considering $\sigma N/N$ as the estimation of the noise in the planogram, where N is the value in each LOR and the σN is the standard deviation of the same value estimated in an uniform region of the same planogram, we have measured a noise reduction factor of 12.5.

5.3.4 Other corrections

There are other corrections that could be applied but were not studied yet for QPEM. Among those we could mention pair normalization, correction for scatter and for pile-up. Attenuation correction is a major task that is left to the reconstruction algorithm.

The general procedure to accomplish data correction will be to detect the sensible information, record it during acquisitions, and apply during planograms generation. For this purpose, the statistics data collection mechanism has been kept as much flexible as possible. But the development and research studies have been left for future works.

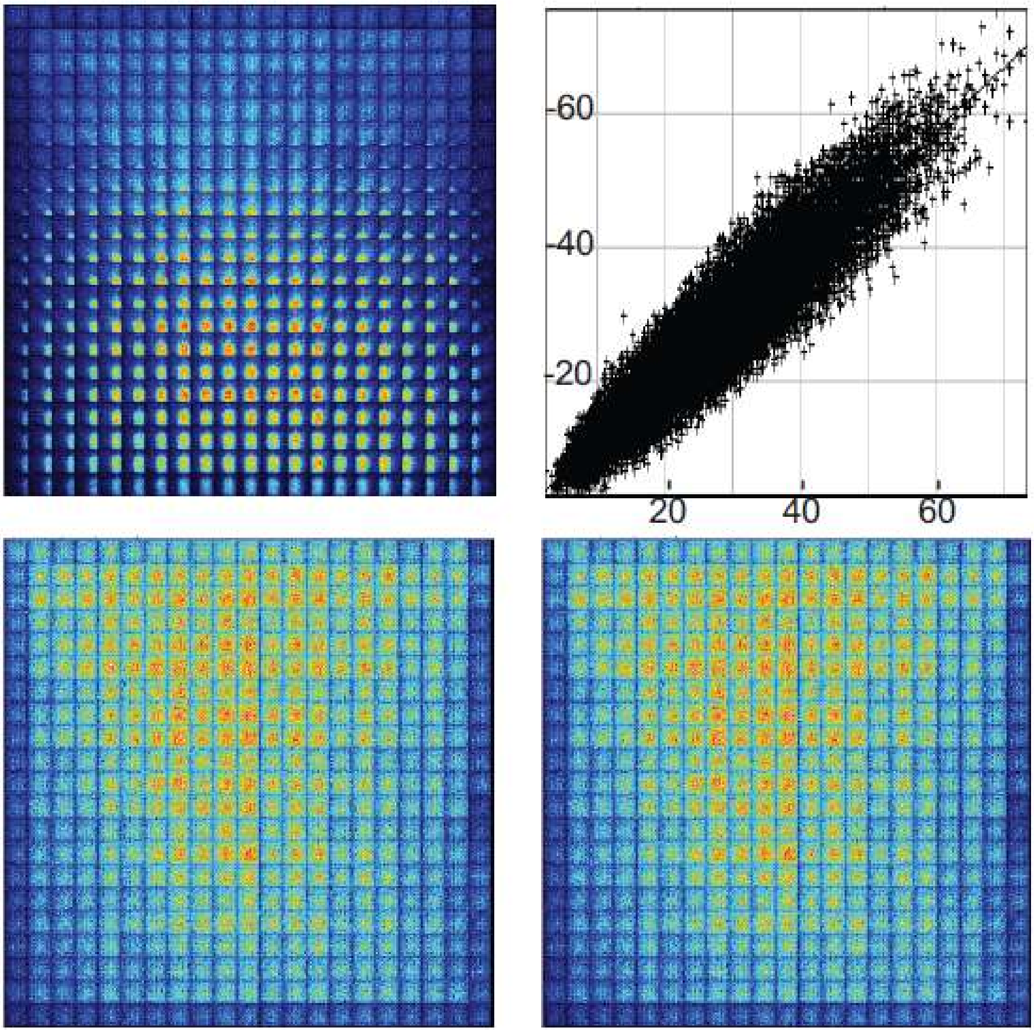

Figure 5.12: Top left: full planogram of prompt coincidence data obtained with the dual head system with the source distribution described in figure 4. Energy window is $350 \div 850 keV$. Planograms are not normalized for crystal efficiency. Bottom row: planograms of delayed coincidence data for the standard (left) and new (right) methods. Top right: scatter plot composed of the LOR values of the new (x) and the standard (y) delayed coincidence planograms showing the correlation between the two planograms.

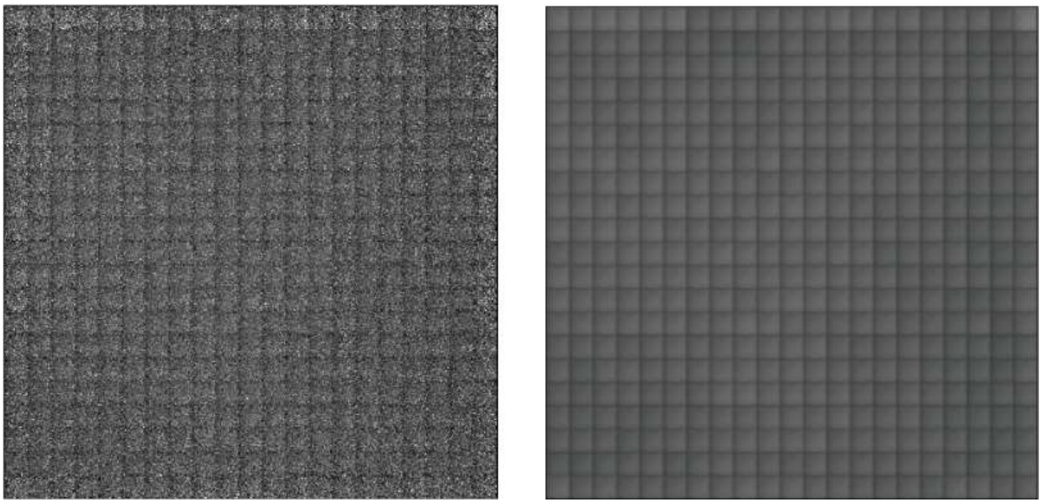

Figure 5.13: Comparison of the delayed coincidence planograms obtained as directly measured (left) and by applying equation 5.14 (right). Planograms are not normalized for LOR efficiency.

Chapter 6

Results and discussion

This chapter collects and discusses the main results obtained during this thesis. The flow of the discussion will follow the steps proposed in order to achieve our objective of designing a state of the art, flexible and cost efficient dedicated PET scanner. The first result consists in the complete design of the scanner, which is later validated. Most of the validation results have been obtained experimentally, with the exception of the coincidence processor that has been validated partially with ModelSim (Mentor Graphics, San Jose, CA, U.S.A.) Register Transfer Level (RTL)/structural simulations and ISE 10.1i (Xilinx Inc., San Jose, CA, U.S.A.) synthesis chains.

6.1 Acquisition system conceptual design

The first achievement in the design process has been the definitive diagram of the acquisition architecture, shown in Figure 6.1. The diagram allowed to early start up the development of the main board, the coincidence board, the FPGA firmware and Host software. However, with the introduction on the synchronous coincidence processor, described in Section 4.2.4, the final design has been further optimized, given that the discrete coincidence board is no more necessary. Moreover, thanks to the I/O compatibility between the two coincidence processing approaches, and given that the discrete coincidence board was already available, it has been left the possibility to switch between the two methods. The final design results as in Figure 6.2.

In this architecture DAQ boards communicate with the Master FPGA through a set of independent I/O signals plus an input data bus per detector plate. Each front-end module outputs four Anger-like signals that are digitized by the DAQ boards and a timing signal that can be processed for coincidence by either the discrete (Figure 6.1) or integrated (Figure 6.2)

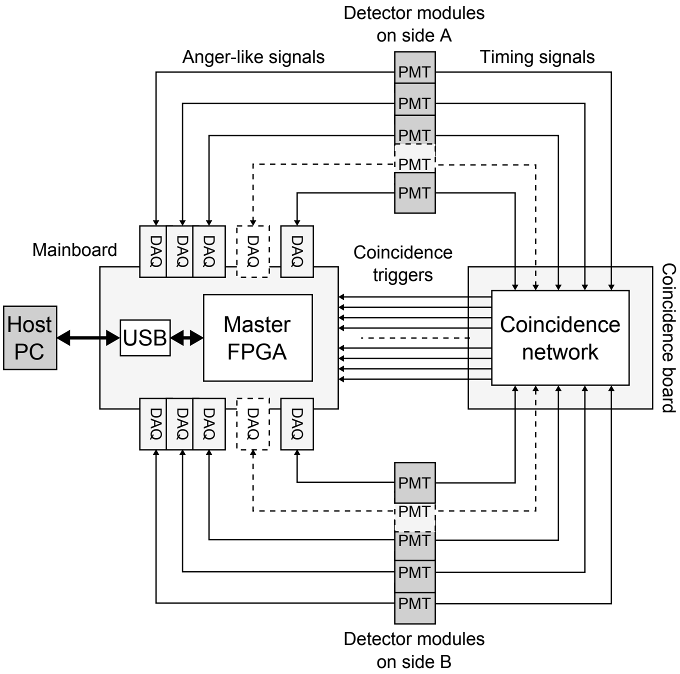

Figure 6.1: QPEM communication architecture diagram with the discrete coincidence network.

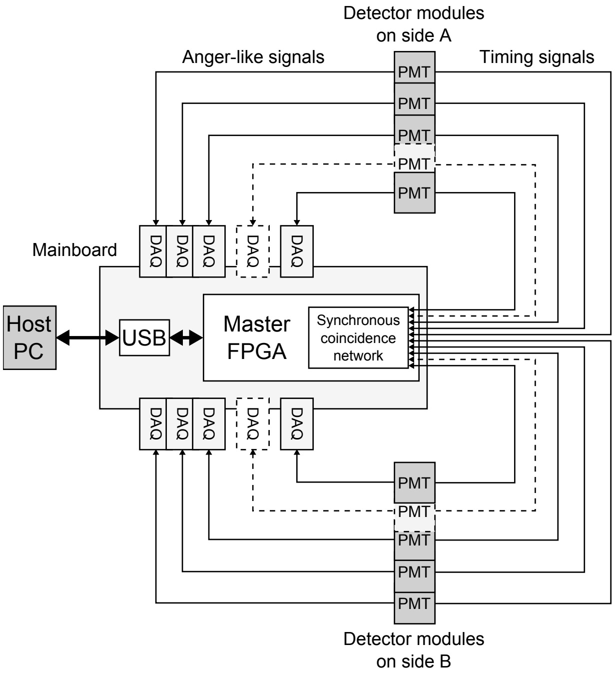

Figure 6.2: QPEM communication architecture diagram with the integrated synchronous coincidence network.

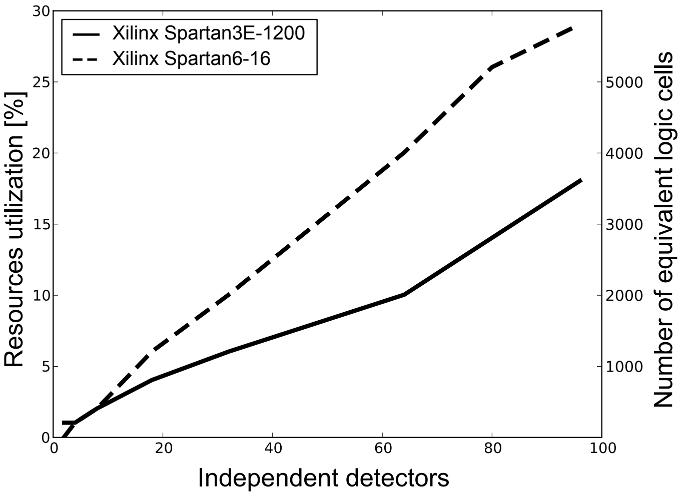

Figure 6.3: FPGA resources utilization vs modules number for two Xilinx low-end target devices.

coincidence network, although the discrete coincidence board will be used mainly for technological comparatives. Real time acquisition control happens at firmware level into the FPGA, while acquisition configuration and data streaming is controlled by the Host PC.

6.2 Cost efficient coincidence processor architecture

The contribution of coincidence processing to both system cost and power consumption is eliminated by fully integrating the synchronous coincidence processor into the Master FPGA. If compared with the discrete coincidence board, the power saved is about 130 W, as estimated in Section 4.2.2, for the nine-module version.

The synchronous gating network has been simulated for 1 to 48 total modules per detector on Xilinx Spartan-3E and Spartan-6 devices in order to assess the resource utilization.

Simulations have been carried out in VHDL testbench and executed within ModelSim (Mentor Graphics, San Jose, CA, U.S.A.), with a simulation granularity of 1 ps. All the simulated components were designed in pure RTL VHDL standard, with the notable exception of the Digital Clock Manager, whose structural simulation model has been obtained with Coregen 10.1i (Xilinx Inc., San Jose, CA, U.S.A.). Results are showed in Figure 6.3.

The resource utilization is below 30% for 96 total modules even on low-end target devices, which makes it easily integrable in any FPGA family. An interesting fact is that the coincidence processor shows to have a logic complexity almost linear with the number of detectors, this is probably an effect of the low complexity of the OR-AND gating reproduced from the discrete coincidence architecture.

Synthesis simulations were performed in order to assess the minimum number of pipeline stages required in order to work at a clock frequency of 288 MHz. The required stages are reported in Table 6.1 for a total number of 2 to 96 modules. It is noteworthy that being the technique synchronous, the real impact of network complexity is only on FPGA resources, which have been demonstrated to be relatively low even on small Spartan devices. The number n of pipeline stages has the only negative effect of adding n/f_{clk} to the total processing latency, where f_{clk} is the adopted clock frequency. For the proposed 4 vs 4 and 9 vs 9 PET implementations, no pipeline stages are required.

Detectors		2	4	8	18	32	64	80	96
Pipeline stages	Spartan3E	0	0	0	0	1	2	3	4
	Spartan6	0	0	0	0	0	2	3	3

Table 6.1: Pipeline stages required to perform synchronous AND-gating of all trigger pulses without affecting the processor clock frequency.

Timing resolution has been simulated and experimentally measured for the reference clock frequency of 288 MHz.

A simplified diagram of the used testbench is shown in Figure 6.4. The *systematic delay* is introduced between the two generated triggers, in order to explore any delay possibility. For each delay the trigger is repeated a parametrizable, generally high, number of times with an applied uniform random jitter to prevent any kind of phase-to-clock biasing effect. The number of coincidences detected per generated triggers is counted and plotted. In the reported plots 100 jittering repetitions were used.

An experimental measurement has been done in a very similar way with respect to the simulation. A generic function synthesizer has been used in order to generate a train of pulses at a specific frequency. The generated pulses were used to emulate CFD outputs and fed to the FPGA pins corresponding to the coincidence processor inputs. The detection efficiency has been then derived by relating the coincidence rate reported by the control software with the singles rate and the imposed pulse frequency. Single rate counters well agreed with the expected frequency and the coincidence to single ratio has been used to calculate the efficiency.

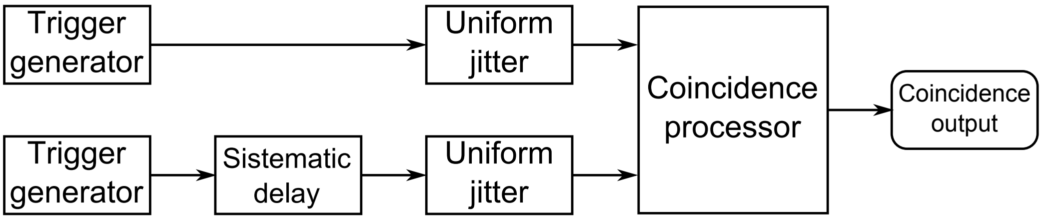

Figure 6.4: Simplified diagram of the HDL testbench used to simulate the coincidence detection efficiency of the synchronous coincidence processor.

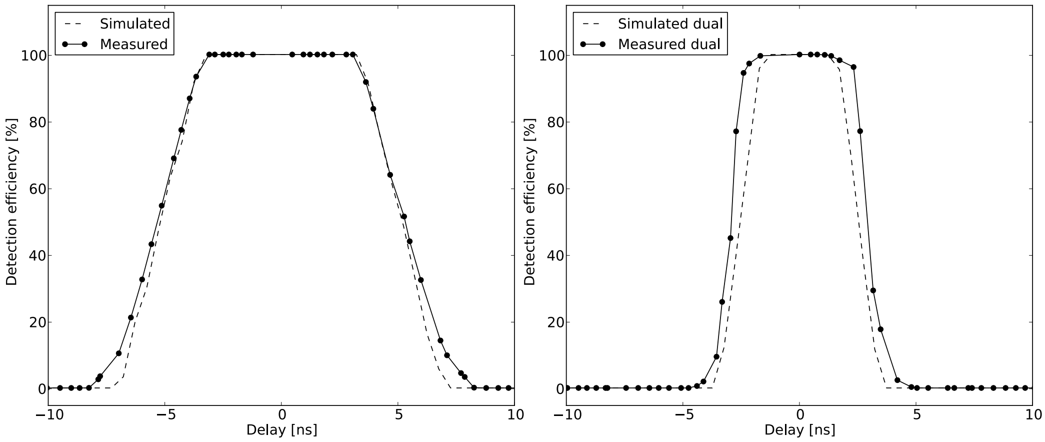

(a) Synchronous coincidence processor.

(b) Dual phase processor.

Figure 6.5: Detection efficiency for the different synchronous coincidence processing techniques.

The measurements results are showed in Figure 6.5a. The FWHM for the simulated case is 10.4 ns, which is exactly $3\tau = 3/f$, where $f = 288$ MHz is the applied clock frequency. In the experimental measurements it can be appreciated the same coincidence resolution.

Measurements have been done with the same method also for the dual-phase technique, resulting in a coincidence resolution of 5.3 ns FWHM (Figure 6.5b). The obtained resolution corresponds to $3/2f$, as expected by previous simulations.

Preliminary experiments with a four-phase coincidence processor have been also carried out, with the maximum clock frequency $f = 200$ MHz. The chosen frequency is the maximum allowed for four-phase clock generation in Spartan-3E devices. In this case, measurements showed that a coincidence resolution of 3.7 ns FWHM can be achieved in the used Spartan-3E device (Figure 6.6), i.e. $3/4f$. However, the behaviour of demetastabilization flip-

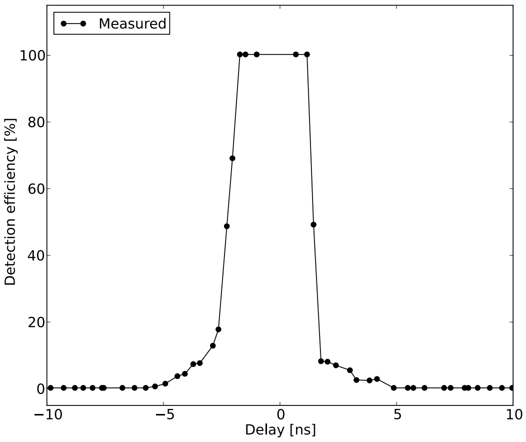

Figure 6.6: Measured coincidence resolution for the quad-phase coincidence processor.

flops for the narrow phase shifts between the four clocks was unpredictable with the available simulation models.

6.3 Architecture implementation

The different architectural choices explored during this thesis have been experimentally characterised through three sub-prototypes with incremental features, each re-designed taking advantage of the previously achieved experience. The final prototype has been also implemented, although at the current state it has not been characterised yet.

All the three sub-prototypes consist of one or more DAQ boards plus an acquisition board based on a XEM3005 (Opal Kelly Inc., Portland, Oregon, U.S.A.). The XEM3005 board equips a CY68013A FX2LP (Cypress Semiconductor, San Jose, CA, U.S.A.) USB controller and a Spartan3E-1200 (Xilinx Inc., San Jose, CA, U.S.A.) FPGA. The final prototype is instead based on a custom designed board, produced by AGE Scientific s.r.l., Capezzano Pianore, LU, Italy. The final prototype equips the same CY68013A USB controller, a StratixIII-SL150 (Altera Corp., San Jose, CA, U.S.A.) and up to 18 DAQ modules. As anticipated in Section 4.3 and as it will be described in Section 6.3.3, the need for a high-end FPGA is mainly due to the higher resources an I/O requirements than the ones provided by the Spartan3E.

The characteristics of each device are summarized in Table 6.2, and the relative pictures are showed in Figure 6.7.

Name	Modules	Area	Capabilities	Coinc. res.
DAQTB1	1	25 cm^2	Calibration, SPECT, DAQ characterization and debug	*N/A*
DAQTB2	2	50 cm^2	PET 1x1, discrete coincidence network, conservative and innovative random estimation, compatible with DoPET software, radioactivity statistics generation	10 ns
PlugNPET	4	100 cm^2	PET 2x2, discrete and synchronous coincidence network, dead time statistics generation, brand-new data analysis software	5 ns
QPEM	18	450 cm^2	PET 9x9, specific USB interface, SiPM compatible	2 ns (*)

(*) The value is expected and based on datasheet characteristics of the Stratix III FPGA.

Table 6.2: Main characteristics of the prototypes realized during this thesis.

6.3.1 The DAQTB1 prototype

The DAQTB1 system was realized as an initial design attempt, in order to characterize the DAQs board and to assess the performance of the asynchronous bus developed prior to this thesis. It was realized by connecting the generic I/O of the XEM3005 platform to a single DAQ. This first prototype contributed to the debug and customization of DAQ firmware, as well as to settle the basis for software acquisition and control instrumentation. It also allowed to define and experiment calibration procedures, such as pedestal acquisition and asynchronous bandwidth tuning. The choice of a dual asynchronous bus is a direct consequence of tests conducted with the DAQTB1.

6.3.2 The DAQTB2 prototype

The DAQTB2 was the first actual proof of concept prototype, being able to resolve and acquire coincidences, thus allowing for first image reconstruction attempts. A suite of interfacing software was realized in order to analyse and reconstruct tomographic images with previously developed DoPET software. The coincidence resolution technique was a simplified version of the final 9 vs 9 discrete network featuring both conservative and innovative delayed window techniques for random estimation. The main aim of this prototype was to have a working platform and a starting point with characteristics equal to that of the DoPET system, but obtained with the new architecture

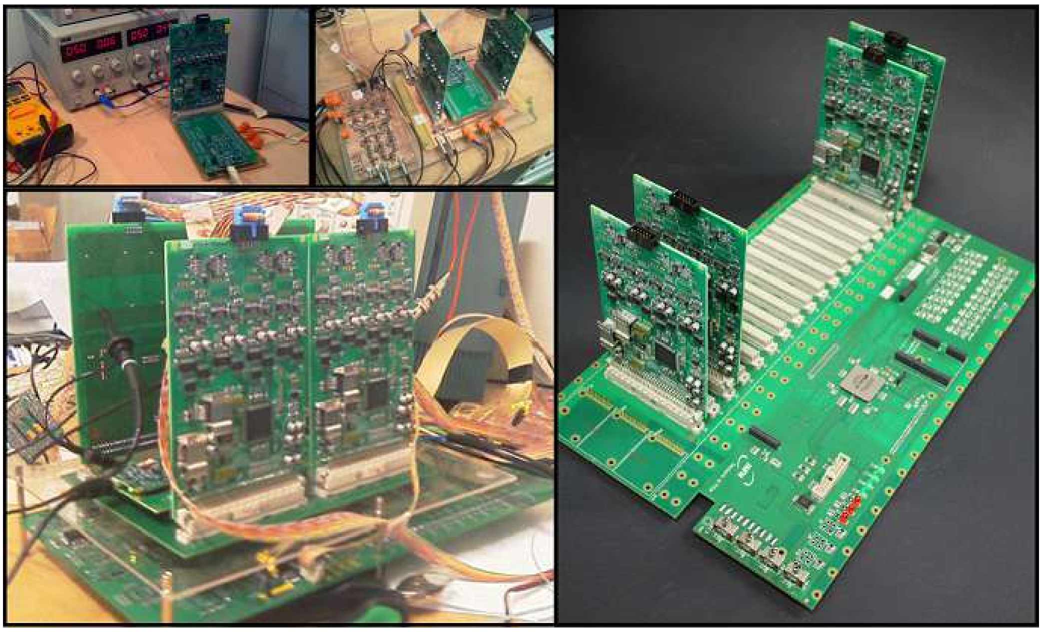

Figure 6.7: Mosaic of the four acquisition system prototypes realized during this thesis.

concept. With this prototype it has been studied the statistical equality of both conservative and innovative delayed window techniques, discussed in Section 4.2.3.

6.3.3 The PlugNPET prototype

The PlugNPET prototype is the first one that exceeded DoPET performances, in terms of data bandwidth, dead time and coincidence resolution. In fact, it is the first with multiple module detectors and the synchronous coincidence network. It also provided the first modular data structures that are being used for the development of a new reconstruction software, that contributes to the list of future works. A relevant result of this implementation, is the proof that the final system requires a higher end FPGA than the Spartan3E. In fact, the current implementation already accounts for 95% of total internal FPGA resources and 100% of total I/O buffers, thus making impossible in practice any further enhancement.

6.3.4 The QPEM prototype

The QPEM system is the complete prototype in which all previous studies and works converged in order to make a state of the art PEM scanner. The board assembly has been already realized, and its software and firmware will be the same as in PlugNPET. However, its host communication interface is still being developed at FIIG and it is expected to be fully operational in the next few months. However, being the architecture concept, the software, firmware and front-end electronics the same in QPEM as in smaller prototypes, a preliminary characterization of the features that constitute the object of this thesis has been possible. The main focus in testing system properties has been, as said in Section 1.2, on the coincidence processing technique and the acquisition efficiency in terms of acquisition rate and dead time. The experiments carried out for this purpose and their results are reported in the following sections.

6.4 System validation and performance characterization

6.4.1 Energy and intrinsic spatial resolution

A series of tests with a ^{18}F-FDG source have been conducted in order to assess the proper function of position encoding logic and energy resolution.

In order to obtain a flood map of each detector module a planar source of 15 cm × 15 cm filled with ^{18}F-FDG has been interposed between two detector plates of 2×2 modules each. The planar source was utilized in order to have an homogeneous activity thus allowing to compare also pixels efficiency, as discussed in Section 5.2. Only two detector modules per plate were connected to the PlugNPET prototype, because the available planar was not large enough to irradiate uniformly all the detector assembly. The obtained flood map and energy histogram are reported in Figure 6.8, with a cross section plot in which the pixel separation can be appreciated. As discussed in Section 5.1.2, pixels at the borders are badly separated because of the characteristics of the symmetric charge division network adopted in the front-end.

The energy histogram has been obtained by correcting each event by the efficiency of its own related pixel. The achieved energy resolution is 20% FWHM, with a minimum energy resolution per single pixel of 15% FWHM.

This results confirm measurements obtained in previous published experiments with the DoPET scanner [Belcari07, Vecchio09]. Any improvements in this figure are related to the detector technology and front-end electronics, most notably the scintillating material and the Anger coding network.

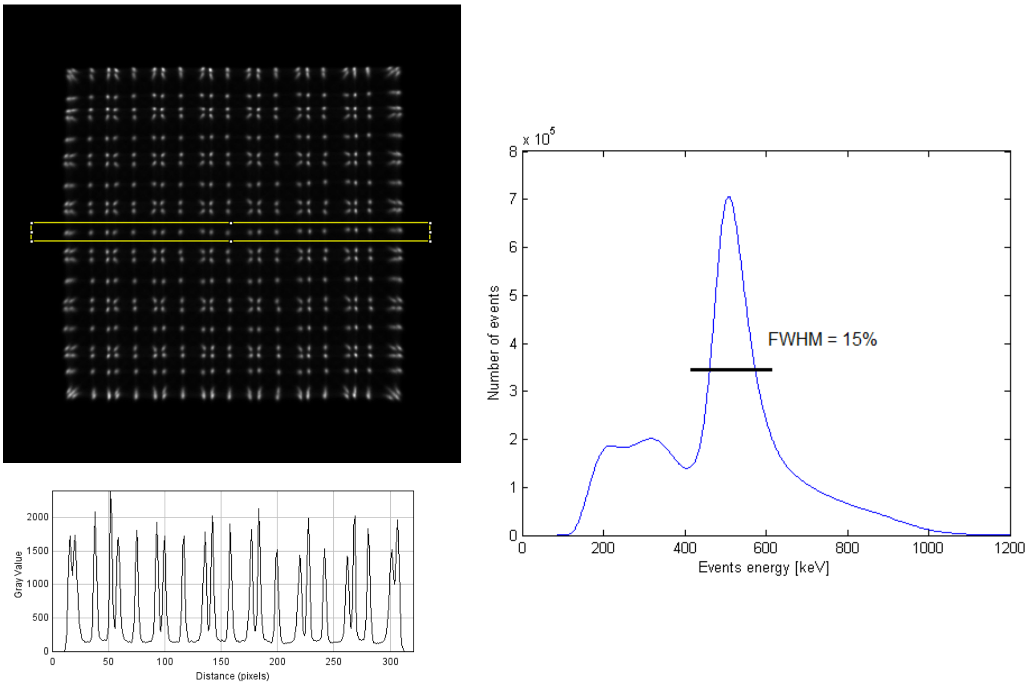

Figure 6.8: Left: Flood map for a ^{18}F-FDG source and his cross section plot. Right: Energy histogram for the same source.

6.4.2 Dead time measurements of the constant fraction discriminators

We calculated the dead time of constant fraction discriminators with the method of the two sources, as described in Section 5.3.2. The experimental setup is illustrated in Figures 6.9 and 6.10. In order to compare the dead time in the case of single or dual module detectors, we used the same PlugNPET prototype to acquire the A, AB, B point sources sequence. The comparison has been achieved by powering only one or both the modules in each detector, and measuring the count rates using the embedded statistics counters of the FPGA.

In the model of paralysable dead time, the transfer function between input PMT pulses N and output triggers R is the following:

$$R = Ne^{-N\tau} \tag{6.1}$$

where τ is the dead time. Given that N is unknown, τ can be obtained comparing the output rates of the two sources when summed separately and acquired together, using the (5.8). If the expected dead time reduction is

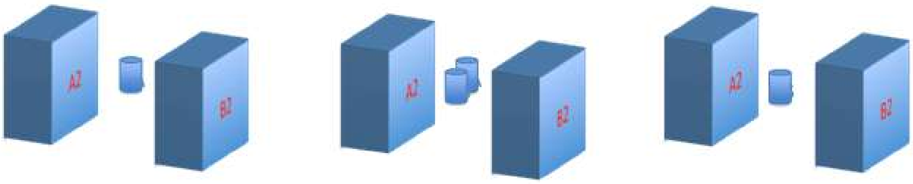

Figure 6.9: Experimental setup for CFD dead time measurements in the case of 2 total modules.

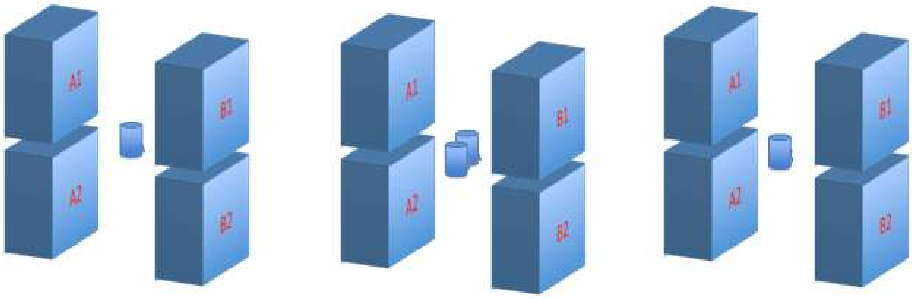

Figure 6.10: Experimental setup for CFD dead time measurements in the case of 4 total modules.

(Section 4.1.1):

$$f = n^2/(n^2 - (n-1)^2) \tag{6.2}$$

Where n is the number of modules per detector. For $n = 2$ is $f = 1.33$. The obtained results are summarized in Table 6.3, it results that $f_{CFD,2} = 1.79$.

Modules	R_A	R_{AB}	R_B	τ
1 vs 1	235 KHz	438 KHz	231 KHz	246 ns
2 vs 2	420 KHz	790 KHz	419 KHz	138 ns

Table 6.3: Two sources experiment results for the estimation of CFD dead time in 2 and 4 modules configuration.

The obtained dead times are sensibly shorter than the expected ones, due to improvements and fine tuning of the CFD carried out by the FIIG during the development of this thesis. However, the relationship between dead times in both configurations meets the expected behaviour and proves the goodness of the modular approach.

6.4.3 Dead time measurements of the acquisition system

With the same setup as described in Section 6.4.1, we calculated the dead time of the acquisition system relating the number of input coincidences, obtained by counting input CFD triggers R_I with the internal statistics counters, and the number of coincidence actually recorded R_O. Having the trigger counter a dead time of about 10 ns, we neglect any losses on the measurement of R_I.

The used formula to obtain this kind of non-paralysable dead time is the same as discussed in Section 5.3.2:

$$T = (R_I - R_O)/(R_O R_I) \tag{6.3}$$

Again, the expected dead time reduction for $n = 2$ is $f = 1.33$ (5.8). The obtained results are summarized in Table 6.4. It results that $f_{ACQ,2} = 1.54$.

Modules	R_I	R_O	T
1 vs 1	57 KHz	55 KHz	564 ns
2 vs 2	127 KHz	122 KHz	364 ns

Table 6.4: Experiment results for the estimation of acquisition system dead time in 2 and 4 modules configuration.

The obtained dead time in the first case is very close to the dead time of 490 ns reported by AGE Scientific for a single DAQ board [Franchi08b], the reduction factor is also very close to the expected one.

6.4.4 Estimation of the combined transference function

The transfer function of the PET system as a whole is determined by the following constants:

- Front-end dead time τ, paralysable
- Coincidence network dead time, negligible
- Acquisition system dead time T, non-paralysable
- Loss factor F, due to the CFD discrimination efficiency

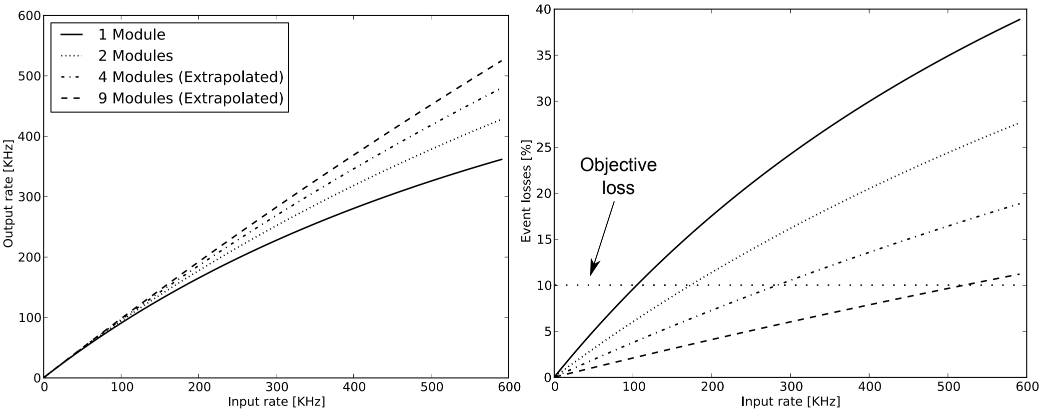

(a) Total transfer function.

(b) Event losses.

Figure 6.11: Comparison between the acquisition efficiency of the system between the configurations with 1, 2, 4 and 9 modules per detectors. Data about the 4 and 9 modules configurations has been extrapolated from the comparison between the 1 and 2 modules versions.

A system of this type has been modelled in [Wicks77]. The resulting transfer function can be derived by means of the following formula:

$$R \approx \frac{FNe^{-N\tau}}{1 + FNe^{-N\tau}(T - \tau)} \tag{6.4}$$

Although the F factor is important for the full characterization, for the scope of this thesis it can be ignored and set to 1. In Figure 6.11a plots of transfer functions for the system in the 1 vs 1 and 2 vs 2 configurations have been reported, and the expected behaviour for the 4 vs 4 and 9 vs 9 implementations have been extrapolated. The extrapolation has been done by numerically iterating the dead time reduction measured for the 2 vs 2 prototype, i.e applying a reduction factor $f_n = f_2^{n/2}$.

The plots show how modularization is necessary to keep event losses under 10% at rates starting from 100 kHz. The 9 vs 9 implementation is expected to keep such low losses up to rates of 500 kHz.

6.4.5 Preliminary image reconstruction with DoPET software

As a proof of correct working, an in-beam acquisition test has been conducted with the DAQTB2 at INFN CATANA (Centro di AdroTerapia e Applicazioni Nucleari Avanzate) facilities in Catania, Italy. A picture of the

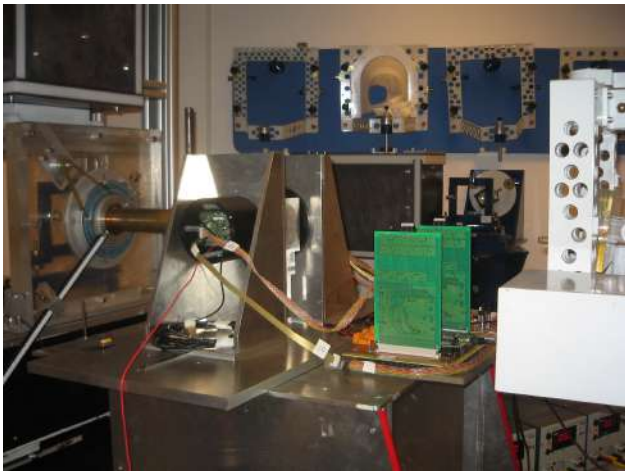

Figure 6.12: Acquisition experiment setup at CATANA.

experiment is shown in Figure 6.12. A 5 cm × 5 cm × 5 cm solid water cube $\rho = 1.046$ g/ cm^3 has been irradiated with a total proton radiation dose of 30 Gy in 20 minutes. The detectors setup is illustrated in Figure 6.13a.

By converting the acquired data to DoPET listmode format we were able to use the DoPET imaging software suite in order to do a preliminary image reconstruction. A comparative of the images reconstructed with DoPET and DAQTB is shown in Figure 6.13b.

As it can be seen, the image resolution obtained with the DAQTB2 was slightly worse. This result was expected because the number of detectors was the same for the old and the new system, thus with no architectural advances with respect to DoPET, but with the difference that the new system was still lacking timing and energy fine tuning at the time of the measurement. An important degrading effect that is present in both systems and that is expected to be considerably enhanced with wider detectors is the absence of information along the y axis due to the limited angular acceptance of the 5 cm × 5 cm detectors.

6.4.6 Projective images and preliminary reconstruction with PlugNPET

Given that a reconstruction software is not yet available for multi-module detectors, we cannot have a proofing reconstructed image for the acquisitions performed with PlugNPET. However, for a demonstrative goal, we can observe the projective 2D images obtained by filtering only parallel LORs orthogonal to the detector plates. The parallel filtering is done by accepting

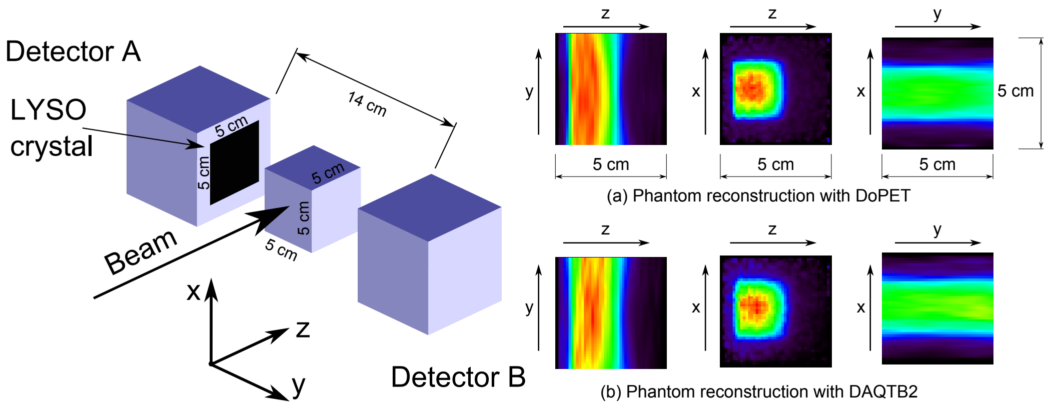

(a) Detectors geometrical setup (b) Reconstructed images

Figure 6.13: Comparative of the reconstructed images acquired with DoPET and DAQTB2. All the cross sections are positioned at the centre of the field of view.

only those LORs that fall within two specific facing pixels. In this way, the obtained image will have the same resolution as the total number of crystal pixels in the scintillating matrix. The demonstrating acquisitions have been done by interposing capillary and punctual sources between the detectors, placed 14cm apart, as illustrated in Figures 6.14a and 6.14b. The obtained images are reported in Figures 6.15a and 6.15b.

As a further demonstration, we also implemented a simple MLEM algorithm, based on a minimalistic geometrical model, in which all the voxels intersected by a given LOR are equiprobable. This model is far from being optimal and precludes any meaningful comparison with state of the art PET images, but it is still a valid source for demonstrating the proper system functioning. Figure 6.16 shows the reconstructed image for a in-beam acquisition with a setup identical to the one illustrated in Figure 6.13a, with the difference that now each detector is composed of two modules.

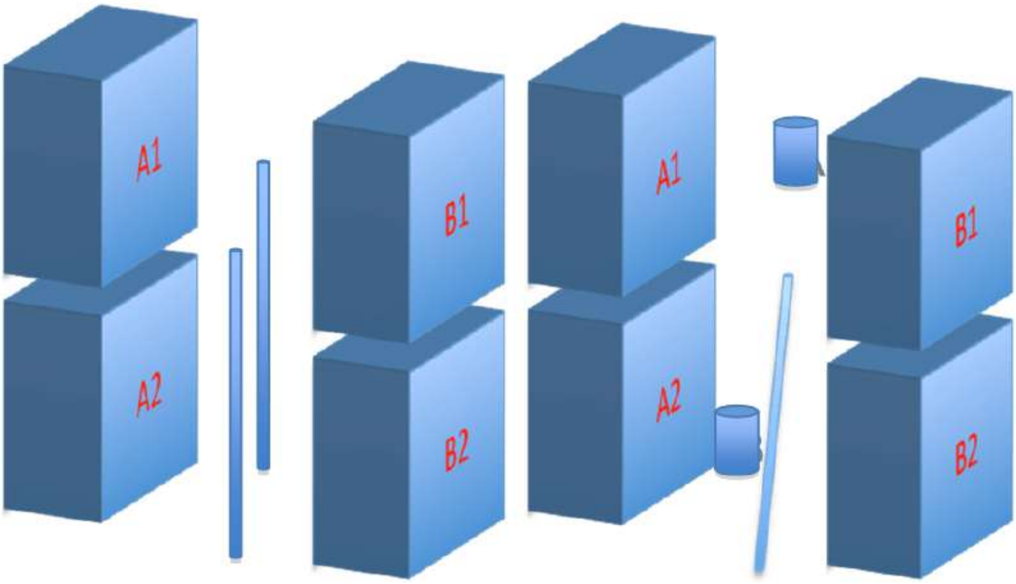

(a) Capillary sources (b) Capillary and punctual sources

Figure 6.14: Experimental setups for the projective imaging of various sources with the PlugNPET prototype.

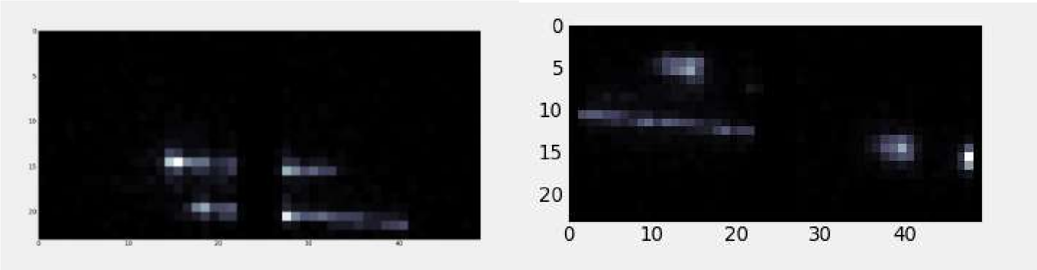

(a) Capillary sources (b) Capillary and point sources

Figure 6.15: Obtained projective images for the setups above.

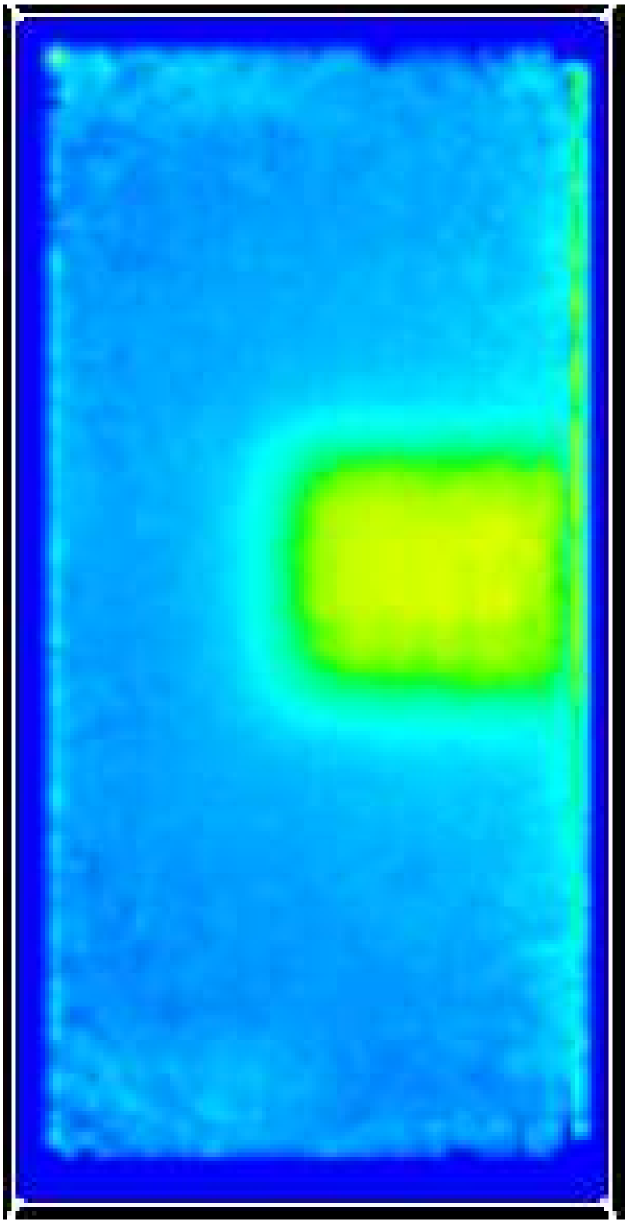

Figure 6.16: PlugNPET preliminary MLEM reconstruction. The acquisition setup is the same as in Figure 6.13a, with the difference that in this case the detector assembly is made of 2 vs 2 modules.

Chapter 7

Conclusion and future works

7.1 Conclusion

This thesis has focused on the design and implementation of the acquisition electronics for a dedicated clinical PET system, as well as the research of cost-efficient solutions for state of the art system performances in PEM and ibPET. This work contributes to different aspects of PET electronics, such as acquisition protocols and coincidence processing. Within this scope it has been demonstrated that:

1. Large area detector heads and high count rates, which are required by modern nuclear medicine applications, can not be achieved be means of a single analogic front-end. It is possible, however, to divide the sensitive area in sectors and distribute the work-load between several modules, thus obtaining the desired performances with minor architectural changes. Even if modularity is not a new concept, it has been demonstrated that it is feasible with the use of low cost standard techniques and off the shelf components.

2. Coincidence processing is the determining problem that could prevent multi-channel detection modularization. Modern timestamping approaches are the solution of choice when the number of detectors is middle-high, but they require an extremely expensive acquisition platform. We demonstrated that a multi-channel, trigger-based coincidence processing is possible with timing resolutions below 5 ns. The all-in-one FPGA approach brings down the coincidence processing cost, and the trigger-based method reduces the events that have to be processed and stored by at least one order of magnitude.

3. A new, symmetrical, delayed window technique has been designed and implemented. The new technique allows to loose different timing constraints that otherwise would tie the coincidence trigger-based approach to poor performances, thus making it a second class alternative to fully digital systems.

4. A series of fully working incremental prototypes have been realized. The prototypes demonstrate how the proposed architecture is suitable for different detector configurations, and represent a proof of concept for the adopted modular read out. The final prototype also represents a ready and valid tool for first investigations in the targeted applications, i.e. PEM and in-beam PET.

7.2 Future works

The experience achieved and the prototypes realized, open a wide range of research lines and further works to follow. Apart from the characterization of the full system, which is currently in its final development phase, and its fine tuning, we can identify four main directions of study:

1. Implement and characterise a reconstruction algorithm suitable for the QPEM scanner. The wider detector area and improved counting statistics are supposed to result in better imaging properties, but this improvement can only be assessed after a proper reconstruction methodology is developed. In designing a reconstruction methodology it would be desirable to keep the geometrical flexibility guaranteed by the hardware architecture.

2. Experiment on-chip signal processing. The FPGA based architecture provides great data processing horsepower. We could, for example, substitute the peak detectors mounted on the DAQ boards with free running ADCs with minimal hardware changes, given that the data acquisition protocol can be reprogrammed. As discussed in Section 4.3.2, we can also experiment real time data processing in the streaming pipeline, such as on-chip pixel identification, energy correction and more complex event validation.

3. Adopt different front-end detector technologies. The proposed architecture is not constrained to PMT-based detectors and can be used also with newer solid state devices, such as Silicon photo-multipliers (SiPM), for better detection performances and newer applications.

4. Study the impact of the new system on reference applications, i.e. PEM and in-beam imaging, that motivated this work and dictated the minimum performances required to allow their use in clinics.

As a final consideration, the fact that the architecture has been designed with special attention on cost, compactness, efficiency and flexibility, make us feel that a decisive development effort, in order to convert the proof of concept in a fully functional system, would result in a successful technology transfer. As discussed in Section 2.5, such a system is highly demanded by the scientific community. Even if the path to its adoption in clinical environments is still long, it could readily be adopted by third research groups in the field of dedicated PET human imaging.

Appendix A

Derivation of solid-angle formula for a dual planar detector system

We want to know the solid angle subtended by the area of two facing planar detectors viewed from a specified point. In order to perform the calculation we will decompose the problem in knowing the solid angle subtended by two oblique pyramids, whose bases are the two detector plates, and whose apices converge to the given point.

In a reference system centred in the point of view, each pyramid consists of four planes that pass through the origin, and intersect the unit sphere on great-circle arcs. Therefore, it will *not* be correct to simply integrate the differential area element $\sin\theta d\phi d\theta$ in spherical coordinates using constant limits of integration. This procedure would give us the solid angle between two lines of latitude and two lines of longitude; however, lines of longitude are great circles, but this is not the case for lines of latitude, so this approach is clearly incorrect.

Instead, to find the proper limits of integration, it will be necessary to write down the equations for the four planes making up the faces of the pyramid and integrate the area between them on the unit sphere. Given that the apex is placed at the origin, two faces of the pyramid will pass through the y axis and two will pass through the z axis.

Let our pyramid have apex angles (measured between opposite faces of the pyramid) α and β both in the range $(0, \pi)$, and let be $\alpha = \alpha_1 + \alpha_2$ $\beta = \beta_1 + \beta_2$, where $\alpha_{1,2}$ are the angles between two opposite faces and the plane xy, and $\beta_{1,2}$ are the angles between the other two faces and the plane xz. Note that if α_1 is positive then α_2 is negative and vice versa, and the same applies to $\beta_{1,2}$. The one of our faces is defined by a plane passing through the y axis at an angle α_1 from the x axis. Its equation is $z = x \tan \alpha_1$, or, converting to spherical coordinates,

$$\theta_1 = \cot^{-1}[\tan \alpha_1 \cos \phi] \tag{A.1}$$

Similarly, a plane passing through the z axis at an angle β_1 from the x axis is given simply by

$$\phi_1 = \beta_1 \tag{A.2}$$

These equations define our limits of integration, and the solid angle Ω of one of the two generally oblique pyramids covered by the two planar detectors becomes

$$\Omega = \int_{\beta_1}^{\beta_2} d\phi \int_{\theta_1}^{\theta_2} \sin \theta d\theta \tag{A.3}$$

Performing the θ integral gives

$$\Omega = -\int_{\beta_1}^{\beta_2} [\cos \theta_2 - \cos \theta_1] d\phi \tag{A.4}$$

We now apply four trigonometric identities to the integrand:

$$\begin{aligned}
\cot^{-1} x &= \pi/2 - \tan^{-1} x \\
\cos(\pi/2 - x) &= -\sin x \\
\sin[\tan^{-1} x] &= \frac{x}{\sqrt{1+x^2}} \\
\cos^2 x &= 1 - sin^2 x
\end{aligned}$$

From this we obtain:

$$
\begin{aligned}
I &= -\int_{\beta_1}^{\beta_2} \cos\theta d\phi \\
&= -\int_{\beta_1}^{\beta_2} \cos\left[\cot^{-1}(\tan\alpha \cdot \cos\phi)\right] d\phi \\
&= -\int_{\beta_1}^{\beta_2} \cos\left[\pi/2 - \tan^{-1}(\tan\alpha \cdot \cos\phi)\right] d\phi \\
&= \int_{\beta_1}^{\beta_2} \sin\left[\tan^{-1}(\tan\alpha \cdot \cos\phi)\right] d\phi \\
&= \int_{\beta_1}^{\beta_2} \frac{\tan\alpha \cdot \cos\phi}{\sqrt{1 + \tan^2\alpha \cdot \cos^2\phi}} d\phi \\
&= \int_{\beta_1}^{\beta_2} \frac{\cos\phi d\phi}{\sqrt{\cot^2\alpha + 1 - \sin^2\phi}} \\
&= \sin^{-1}\left(\frac{\sin\phi}{\sqrt{\cot^2\alpha + 1}}\right)\Big|_{\beta_1}^{\beta_2} \\
&= \sin^{-1}(\sin\phi \cdot \sin\alpha)\Big|_{\beta_1}^{\beta_2}
\end{aligned}
$$

Where we have changed variables to $u = \sin\phi$ in performing the integral and we applied the identity $1 + \cot^2 x = 1/\sin^2 x$. It follows that

$$
\Omega = I|_{\theta_1}^{\theta_2} = \sin^{-1}(\sin\beta \cdot \sin\alpha)|_{\beta_1}^{\beta_2}|_{\alpha_1}^{\alpha_2} \tag{A.5}
$$

Which is the required formula for the generic case of an oblique pyramid. In the particular case of a right pyramid, we have

$$
\begin{aligned}
\alpha_1 &= -\alpha/2 \\
\alpha_2 &= \alpha/2 \\
\beta_1 &= -\beta/2 \\
\beta_2 &= \beta/2
\end{aligned}
$$

And therefore

$$
\Omega_{right} = 4\sin^{-1}[\sin\alpha/2 \cdot \sin\beta/2] \tag{A.6}
$$

At this point it is important to note that the angles $\alpha_{1,2}$ and $\beta_{1,2}$ of each pyramid are not the angles that join the origin to the vertices of each planar

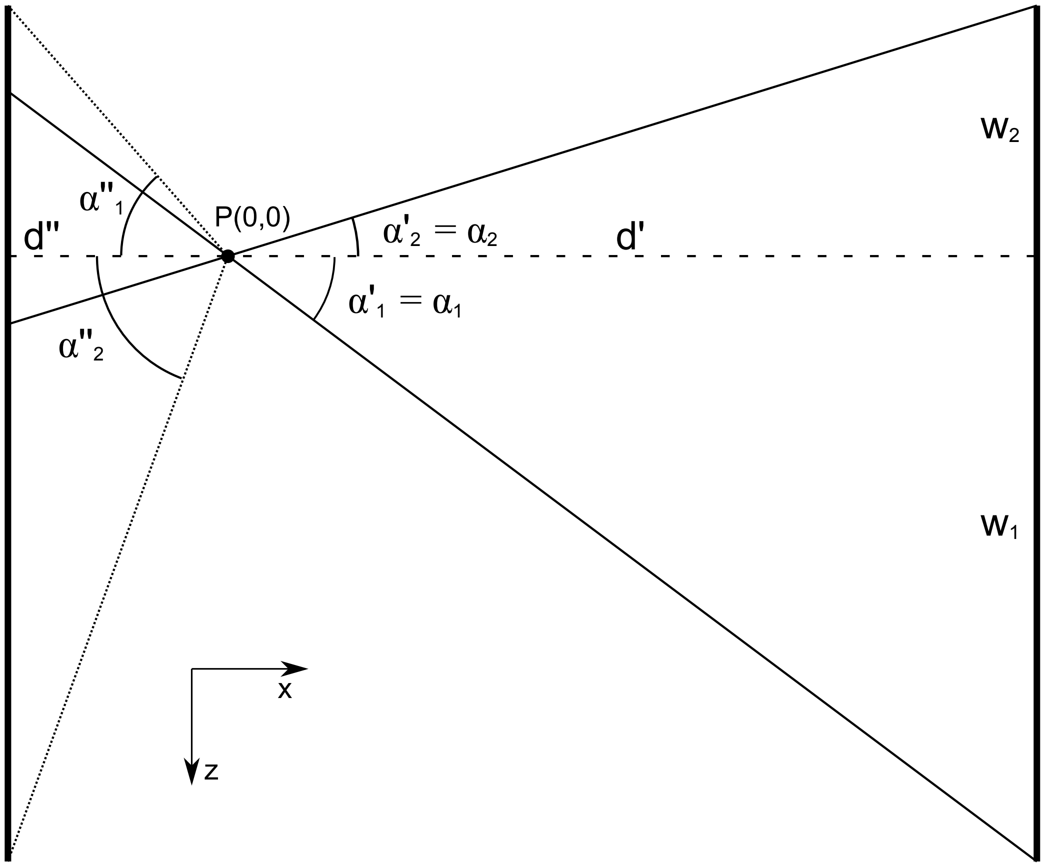

Figure A.1: Projection of the solid angle of interest on the plane xz.

detector, but the angles compatible with lines of response that fall entirely inside both pyramids. In order to calculate these angles we can analyse the problem separately in the xz plane for the calculation of $\alpha_{1,2}$ (Figure A.1).

It can be seen that

$$\alpha_{1,2} = \min(\alpha'_{1,2}, \alpha''_{1,2}) \tag{A.7}$$

And therefore

$$\begin{aligned}
\alpha_1 &= \min(\tan^{-1}\frac{w_1}{d'}, \tan^{-1}\frac{w_2}{d''}) \\
\alpha_2 &= \min(\tan^{-1}\frac{w_2}{d'}, \tan^{-1}\frac{w_1}{d''}) \\
\beta_1 &= \min(\tan^{-1}\frac{h_1}{d'}, \tan^{-1}\frac{h_2}{d''}) \\
\beta_2 &= \min(\tan^{-1}\frac{h_2}{d'}, \tan^{-1}\frac{h_1}{d''})
\end{aligned}$$

Where $w_{1,2}$ and $h_{1,2}$ are the projections of the angles on the sides of the detector plates, that sum the width w and the height h of the plate. Let's now translate the reference system so that the origin coincides with the centre of the field of view. Given an arbitrary point of view $P(x, y, z)$ It will be

$$\begin{aligned}
w_1 &= w/2 - z \\
w_2 &= z - w/2 \\
h_1 &= h/2 - y \\
h_2 &= y - h/2 \\
d' &= x - d/2 \\
d'' &= d/2 - x
\end{aligned}$$

And the total solid angle subtended from P to the detector plates will be

$$\Omega_{PEM} = \Omega(\alpha'_1, \alpha'_2, \beta'_1, \beta'_2) + \Omega(\alpha''_1, \alpha''_2, \beta''_1, \beta''_2) = 2 \cdot \Omega(\alpha_1, \alpha_2, \beta_1, \beta_2) \quad \text{(A.8)}$$

where

$$\begin{aligned}
\alpha_1 &= \min(\tan^{-1}\frac{w/2 - z}{x - d/2}, \tan^{-1}\frac{z - w/2}{d/2 - x}) \\
\alpha_2 &= \min(\tan^{-1}\frac{z - w/2}{x - d/2}, \tan^{-1}\frac{w/2 - z}{d/2 - x}) \\
\beta_1 &= \min(\tan^{-1}\frac{h/2 - y}{x - d/2}, \tan^{-1}\frac{y - h/2}{d/2 - x}) \\
\beta_2 &= \min(\tan^{-1}\frac{y - h/2}{x - d/2}, \tan^{-1}\frac{h/2 - y}{d/2 - x})
\end{aligned}$$

Glossary

ADC Analog to Digital Converter.

APD Avalanche Photodiode.

API Application Programming Interface.

ASIC Application Specific Integrated Circuit.

BASTEI Beta Activity meaSurements at the Therapy with Energetic Ions (camera).

BGO Bismuth germanate.

BIT Biomedical Image Technologies group, Universidad Politécnica de Madrid, Madrid, Spain.

BPET Breast PET.

C-PEM C-Shaped PEM.

CATANA Centro di AdroTerapia e Applicazioni Nucleari Avanzate (Hadrotherapy and advanced nuclear application center), Catania, Italy.

CERN Conseil européen pour la recherche nucléaire (European Organization for Nuclear Research), Geneva, Switzerland.

CFD Constant Fraction Discriminator.

CNR Consiglio Nazionale delle Ricerche (National Research Council), Italy.

cPCI Compact PCI.

CPET C-Shaped PET.

CT Computed Tomography.

DAQ Data Acquisition (module).

DoPET Dosimetry PET.

DoPET2 Second generation of DoPET.

EU European Union.

FDG FluoroDeoxyGlucose.

FIFO First In First Out.

FIIG Functional Imaging and Instrumentation Group, Università di Pisa, Pisa, Italy.

FOV Field Of View.

FPGA Field Programmable Gate Array.

FSM Finite State Machine.

FWHM Full-Width Half-Maximum.

GSI GSI Helmholtz Centre for Heavy Ion Research GmbH, Darmstadt, Germany, the former name was Gesellschaft für SchwerIonenforschung (Centre for Heavy Ion Research).

HR High Resolution.

HR-PET HR PET, i.e. a dedicated PET scanner with small field of view and high resolution.

HRRT High Resolution Research Tomograph, CTI PET Systems, Knoxville, U.S.A.

ibPET In-beam PET.

IEEE Institute of Electrical and Electronics Engineers.

INFN Istituto Nazionale di Fisica Nucleare (National Institute for Nuclear Physics), Italy.

LBNL Lawrence Berkeley National Laboratory, Berkeley, U.S.A..

LGSO Lutetium Gadolinium Oxyorthosilicate.

LOR Line Of Response.

LSO Lutetium Oxyorthosilicate.

LYSO Lutetium Yttrium Orthosilicate.

maxPET Dedicated Mammary and Axillary PET.

MDA Monroe Dunaway Anderson Cancer Center, Texas, U.S.A..

MLEM Maximum-Likelihood Expectation-Maximization.

MRI Magnetic Resonance Tomography.

N/D Not Declared.

NECR Noise Equivalent Count Rate.

NEMA National Electrical Manufacturers Association, U.S.A..

NIH National Institutes of Health, U.S.A..

NIM Nuclear Instrumentation Module.

PCB Printed Circuit Board.

PCI Peripheral Component Interconnect.

PECL Positive emitter-coupled logic.

PEM Positron Emission Mammography.

PEM-MRI Integrated PEM and MRI scanner.

PET Positron Emission Tomography.

PET-CT Integrated PET and X-ray CT scanner.

PET-MRI Integrated PET and MRI scanner.

PMT Photo Multiplier Tube.

PPV Positive predictive value.

PS-PMT Position sensitive PMT.

PSP Pulse Shape Preamplifier.

QDC Charge-to-Digital Converter.

QPEM Quad PEM.

RC Resistor-Capacitor (circuit).

RTL Register Transfer Level.

SBIR Small Business Incentive for Research program, U.S.A..

SCD Symmetric Charge Division.

SiAPD Silicon APD.

SiPM Silicon Photomultiplier.

SPECT Single Photon Emission Computed Tomography.

TDC Time to Digital Converter.

TNM Tumours, Node, Metastasis classification of malignant tumours.

TOF Time Of Flight.

TPS Treatment Planning System project, INFN and others.

UCLA University of California, Los Angeles, U.S.A..

US Ultrasound.

USB Universal Serial Bus.

VAX Virtual Address eXtension (computer architecture).

VESA Video Electronics Standards Association.

VHDL VHSIC Hardware Description Language.

VHSIC Very High Speed Integrated Circuits.

VME VERSA(tile)-bus Module Eurocard.

WB Whole body.

WB-PET Whole body PET scanner.

XML eXtensible Markup Language.

YAP Yttrium Aluminium Perowskite.

YAP-PEM PEM scanner based on YAP detectors developed at Università di Pisa.

YAP-PET PET scanner based on YAP detectors developed at Università di Pisa.

References

[Abreu05a] M. C. Abreu, J. D. Aguiar, E. Albuquerque, F. G. Almeida, P. Almeida, P. Amaral, P. Bento, R. Bugalho, B. Carrico, H. Cordeiro*et al.* *First experimental results with the Clear-PEM detector.* In IEEE Nuclear Science Symposium and Medical Imaging Conference Record, volume 3, 2005.

[Abreu05b] M. C. Abreu, P. Almeida, F. Balau, N. C. Ferreira, S. Fetal, F. Fraga, M. Martins, N. Matela, R. Moura, C. Ortigao*et al.* *Clear-PEM: A dedicated pet camera for improved breast cancer detection.* Radiation protection dosimetry, vol. 116, no. 1-4, page 208, 2005.

[Adler93] L. P. Adler, J. P. Crowe, N. K. Al-Kaisi & J. L. Sunshine. *Evaluation of breast masses and axillary lymph nodes with [F-18] 2-deoxy-2-fluoro-D-glucose PET.* Radiology, vol. 187, no. 3, page 743, 1993.

[Albuquerque09] E. Albuquerque, V. Bexiga, R. Bugalho, B. Carriço, C. S. Ferreira, M. Ferreira, J. Godinho, F. Gonçalves, C. Leong, P. Lous a, P. Machado, R. Moura, P. Neves, C. Ortig ao, F. Piedade, Jo ao F. Pinheiro, J. Rego, A. Rivetti, P. Rodrigues, José C. Silva, M. M. Silva, I. C. Teixeira, J. P. Teixeira, A. Trindade & J. Varela. *Experimental characterization of the 192 channel Clear-PEM frontend ASIC coupled to a multi-pixel APD readout of LYSO:Ce crystals.* Nuclear Instruments and Methods in Physics Research Section A, vol. 598, no. 3, pages 802–814, 2009.

[Attanasi09] F. Attanasi, N. Belcari, A. Del Guerra, W. Enghardt, S. Moehrs, K. Parodi, V. Rosso & S. Vecchio. *Comparison of two dedicated 'in beam' PET systems via simultaneous imaging of 12 C-induced ß-activity.* Physics in Medicine and Biology, vol. 54, no. 29, pages N29–N35, 2009.

[Avril99] N. Avril, M. Schelling, J. Dose, WA Weber & M. Schwaiger. *Utility of PET in Breast Cancer.* Clinical positron imaging: official journal of the Institute for Clinical PET, vol. 2, no. 5, page 261, 1999.

[Avril00] N. Avril, C. A. Rose, M. Schelling, J. Dose, W. Kuhn, S. Bense, W. Weber, S. Ziegler, H. Graeff & M. Schwaiger. *Breast Imaging With Positron Emission Tomography and Fluorine-18 Fluorodeoxyglucose: Use and Limitations.* Journal of Clinical Oncology, vol. 18, no. 20, pages 3495–3502, 2000.

[Badawi99] R. D. Badawi, M. P. Miller, D. L. Bailey & P. K. Marsden. *Randoms variance reduction in 3D PET.* Physics in Medicine and Biology, vol. 44, pages 941–954, 1999.

[Barth97] A. Barth, P. H. Craig & M. J. Silverstein. *Predictors of axillary lymph node metastases in patients with T1 breast carcinoma.* Cancer, vol. 79, no. 10, pages 1918–1922, 1997.

[Baum97] M. Baum. *Patients'perception of risk and breast cancer awareness.* British Journal of Radiology, vol. 70, no. 836, page 777, 1997.

[Belcari04] N. Belcari & A. Del Guerra. *Development of a Positron Emission Mammography scanner for breast cancer detection.* PhD thesis, Università degli studi di Pisa, 2004.

[Belcari07] N. Belcari, A. Del Guerra, M. Camarda, L. Spontoni, S. Vecchio & D. Bianchi. *Performance of a four-output front-end electronics for multi-anode*

PMTS readout of scintillator arrays. Nuclear Instruments and Methods in Physics Research Section A, vol. 572, no. 1, pages 335–337, 2007.

[Bennett78] G. W. Bennett, J. O. Archambeau, B. E. Archambeau, J. I. Meltzer & C. L. Wingate. *Visualization and transport of positron emission from proton activation in vivo.* Science, vol. 200, no. 4346, page 1151, 1978.

[Bento04] P. Bento, C. Leong, F. Gongalves, I. C. Teixeira, J. P. Teixeira, J. Nobre, P. Relvas, L. Silva, P. Rodrigues, A. Trindade*et al.* *Architecture and first prototype tests of the Clear-PEM electronics systems.* In IEEE Nuclear Science Symposium and Medical Imaging Conference Record, volume 6, 2004.

[Berg06] W. A. Berg, I. N. Weinberg, D. Narayanan, M. E. Lobrano, E. Ross, L. Amodei, L. Tafra, L. P. Adler, J. Uddo, W. Stein*et al.* *High-resolution fluorodeoxyglucose positron emission tomography with compression is highly accurate in depicting primary breast cancer.* Breast Journal, vol. 12, no. 4, page 309–323, 2006.

[Berg10] We. A. Berg, J. D. Blume, A. M. Adams, R. A. Jong, R. G. Barr, D. E. Lehrer, E. D. Pisano, W. P. Evans, M. C. Mahoney, L. Hovanessian Larsen, G. J. Gabrielli & E. B. Mendelson. *Reasons Women at Elevated Risk of Breast Cancer Refuse Breast MR Imaging Screening.* Radiology, vol. 254, no. 1, pages 79–87, 2010.

[Bergman98] A. M. Bergman, C. J. Thompson, K. Murthy, J. L. Robar, R. L. Clancy, M. J. English, A. Loutfi, R. Lisbona & J. Gagnon. *Technique to obtain positron emission mammography images in registration with x-ray mammograms.* Medical Physics, vol. 25, page 2119, 1998.

[Bonifacio09] D. A. B. Bonifacio, N. Belcari, S. Moehrs, M. Moralles, V. Rosso, S. Vecchio & A. Del Guerra.

A time efficient optical model for GATE simulation of a LYSO scintillation matrix used in PET applications. In IEEE Nuclear Science Symposium and Medical Imaging Conference Record, pages 1468–1473, 2009.

[Bowen09] S. L. Bowen, Y. Wu, A. J. Chaudhari, L. Fu, N. J. Packard, G. W. Burkett, K. Yang, K. K. Lindfors, D. K. Shelton, R. Hagge, A. D. Borowsky, S. R. Martinez, J. Qi, J. M. Boone, S. R. Cherry & R. D. Badawi. *Initial Characterization of a Dedicated Breast PET/CT Scanner During Human Imaging.* Journal of Nuclear Medicine, vol. 50, no. 9, pages 1401–1408, 2009.

[Boyle03] P. Boyle, P. Autier, H. Bartelink, J. Baselga, P. Boffetta, J. Burn, H. J. G. Burns, L. Christensen, L. Denis, M. Dicato, V. Diehl, R. Doll, S. Franceschi, C. R. Gillis, N. Gray, L. Griciute, A. Hackshaw, M. Kasler, M. Kogevinas, S. Kvinnsland, C. La Vecchia, F. Levi, J. G. McVie, P. Maisonneuve, J. M. Martin-Moreno, J. Newton Bishop, F. Oleari, P. Perrin, M. Quinn, M. Richards, U. Ringborg, C. Scully, E. Siracka, H. Storm, M. Tubiana, T. Tursz, U. Veronesi, N. Wald, W. Weber, D. G. Zaridze, W. Zatonski & H. zur Hausen. *European Code Against Cancer and scientific justification: third version.* Annals of Oncology, vol. 14, no. 7, pages 973–1005, 2003.

[Boyle04] P. Boyle, N. Gray, J. Henningfield, J. Seffrin & W. Zatonski. Tobacco: science, policy and public health. Oxford University Press, 2004.

[Boyle08] P. Boyle & B. Levin. World cancer report 2008. IARC Press, 2008.

[Brasse05] D. Brasse, P. E. Kinahan, C. Lartizien, C. Comtat, M. Casey & C. Michel. *Correction Methods for Random Coincidences in Fully 3D Whole-Body PET: Impact on Data and Image Quality.* Journal of Nuclear Medicine, vol. 46, no. 5, pages 859–867, 2005.

[Buchanan05] C. L. Buchanan, E. A. Morris, P. L. Dorn, P. I. Borgen & K. J. Van Zee. *Utility of Breast Magnetic Resonance Imaging in Patients With Occult Primary Breast Cancer.* Annals of Surgical Oncology, vol. 12, no. 12, pages 1045–1053, 2005.

[Byars10] L. Byars, C. J. Michel, H. Rothfuss & C. C. Watson. *System and method for scatter normalization of PET images.* US patent, no. 0078568, 2010.

[Camarda06] M. Camarda, N. Belcari, A. Del Guerra, S. Galeotti, F. Morsani, D. J. Herbert & A. Vaiano. *Development of the YAP-PEM scanner for breast cancer imaging.* Physica Medica, vol. 21, pages 114–116, 2006.

[Chae07] M. J. Chae, T. H. Lee, G. Y. Park, J. Y. Yu, M. S. Pai, H. J. Kang, G. J. Cheon, C. W. Choi & S. M. Lim. *Comparing 18F-FDG-PET/CT with other imaging modalities for detecting involving bone of multiple myeloma.* In Society of Nuclear Medicine Annual Meeting Abstracts, volume 48, page 351P, 2007.

[Chaudhari10] A. J. Chaudhari. *Conference Scene: 2009 IEEE NSS/MIC in the USA.* Imaging, vol. 2, no. 1, pages 13–15, 2010.

[Cherry95] S. R. Cherry & M. E. Phelps. *Positron emission tomography: methods and instrumentation.* Diagnostic Nuclear Medicine. Baltimore, Williams and Wilkins, vol. 1, pages 139–159, 1995.

[Cherry98] S. R. Cherry. *A Dedicated PET Scanner for Axillary Node Imaging.* Tech. report, Storming Media, p. 19, 1998.

[Cherry03] S. R. Cherry, J. A. Sorenson & M. E. Phelps. Physics in nuclear medicine. Saunders, 2003. pp. 181-182.

[Conti05] M. Conti, B. Bendriem, M. Casey, M. Chen, F. Kehren, C. Michel & V. Panin. *First experimental results of time-of-flight reconstruction on* *an LSO PET scanner.* Physics in Medicine and Biology, vol. 50, no. 19, pages 4507–4526, 2005.

[Crespo06] P. Crespo, G. Shakirin & W. Enghardt. *On the detector arrangement for in-beam PET for hadron therapy monitoring.* Physics in Medicine and Biology, vol. 51, no. 9, pages 2143–2164, 2006.

[Czernin02] J. Czernin. *FDG-PET in Breast Cancer: A Different View of its Clinical Usefulness.* Molecular Imaging & Biology, vol. 4, no. 1, pages 35–45, 2002.

[Dahlbom87] M. Dahlbom & E. J. Hoffman. *Problems in signal-to-noise ratio for attenuation correction in high resolution PET.* IEEE Transactions on Nuclear Science, vol. 34, no. 1, pages 288–293, 1987.

[Damiani02] C. Damiani, A. Cotta Ramusino, R. Malaguti, A. Del Guerra, G. Di Domenico & G. Zavattini. *A new electronic read-out for the YAPPET scanner.* Nuclear Instruments and Methods in Physics Research Section A, vol. 490, no. 1-2, pages 356–365, 2002.

[Derenzo93] S. E. Derenzo, W. W. Moses, R. H. Huesman & T. F. Budinger. *Critical instrumentation issues for< 2 mm resolution, high sensitivity brain PET.* Annals of Nuclear Medicine, vol. 7, page 3–3, 1993.

[Doshi99] N. K. Doshi, S. R. Cherry & R. W. Silverman. *Novel design of a modular detector for the maxPET breast cancer imaging system.* Journal of Nuclear Medicine, vol. 40, no. 5, page 1223, 1999.

[Doshi00a] N. K. Doshi & S. R. Cherry. *Design And Development Of A Mammary And Axillary Region Positron Emission Tomography System (maxpet).* PhD thesis, University of Los Angeles, California, 2000.

[Doshi00b] N. K. Doshi, Y. Shao, R. W. S. & S. R. Cherry. *Design and evaluation of an LSO PET detector for breast cancer imaging.* Medical Physics, vol. 27, no. 7, pages 1535–1543, 2000.

[Doshi01] N. K. Doshi, R. W. Silverman, Y. Shao & S. R. Cherry. *maxPET: A dedicated mammary and axillary region PET imaging system for breast cancer.* IEEE Transactions on Nuclear Science, vol. 48, no. 3, pages 811–815, 2001.

[Enghardt99] W. Enghardt, J. Debus, T. Haberer, B. G. Hasch, R. Hinz, O. Jäkel, M. Krämer, K. Lauckner & J. Pawelke. *The application of PET to quality assurance of heavy-ion tumor therapy.* Strahlentherapie und Onkologie, vol. 175, pages 33–36, 1999.

[Enghardt04] W. Enghardt, K. Parodi, P. Crespo, F. Fiedler, J. Pawelke & F. Ponisch. *Dose quantification from in-beam positron emission tomography.* Radiotherapy and Oncology, vol. 73, pages 96–98, 2004.

[Escalona10] S. Escalona, J. Blasco, M. Reza, E. Andradas & N. Gómez. *A systematic review of FDG-PET in breast cancer.* Medical Oncology, vol. 27, pages 114–129, 2010.

[Evans55] R. D. Evans. Atomic nucleus. McGraw-Hill New York, 1955.

[Fleming97] I. D. Fleming, J. S. Cooper, D. E. Henson, R. V. P. Hutter, P. J. Kennedy, G. P. Murphy, P. O. Sullivan, L. H. Sobin & J. W. Yarbro. American joint committee on cancer: AJCC cancer staging manual. Philadelphia: Lippincott-Raven, 1997.

[Fowler97] J. S. Fowler & A. P. Wolf. *Working against Time: Rapid Radiotracer Synthesis and Imaging the Human Brain.* Accounts of Chemical Research, vol. 30, no. 4, pages 181–188, 1997.

[Franchi08a] G. Franchi. *Note sul disegno di alcuni circuiti analogici usati nella fisica delle alte energie.* Unpublished notes, property of AGE Scientific s.r.l., Capezzano Pianore, Lucca, Italy, 2008.

[Franchi08b] G. Franchi. *Scheda DAQ per PET.* Internal documentation in possession of the FIIG - Dipartimento di Fisica - Università di Pisa, 2008.

[Franchi08c] G. Franchi, N. Belcari & A. Del Guerra. *Proposta di realizzazione di sottoparti per PET.* Internal documentation in possession of the FIIG - Dipartimento di Fisica - Università di Pisa, 2008.

[Franchi09] G. Franchi, N. Belcari, G. Sportelli & F. Spinella. *Studio della rete di coincidenza.* Internal documentation in possession of the FIIG - Dipartimento di Fisica - Università di Pisa, and the BIT - E.T.S.I. de Telecomunicación - Universidad Politécnica de Madrid, 2009.

[Freifelder95] R. Freifelder & J. S. Karp. *A dedicated PET scanner for breast cancer.* In IEEE Nuclear Science Symposium and Medical Imaging Conference Record, volume 3, pages 1358–1362, 1995.

[Freifelder97] R. Freifelder & J. S. Karp. *Dedicated PET scanners for breast imaging.* Physics in Medicine and Biology, vol. 42, no. 12, page 2463–2480, 1997.

[Freifelder01] R. Freifelder, C. Cardi, I. Grigoras, J.R. Saffer & J.S. Karp. *First results of a dedicated breast PET imager, BPET, using NaI(Tl) curve plate detectors.* In IEEE Nuclear Science Symposium and Medical Imaging Conference Record, volume 3, pages 1241–1245 vol.3, 2001.

[Guerra02] A. Del Guerra, N. Belcari, W. Bencivelli, A. Motta, S. Righi, A. Vaiano, G. Di Domenico, E. Moretti, N. Sabba, G. Zavattini*et al. Monte Carlo study and experimental measurements of breast tumor detectability with the YAP-PEM prototype.* In IEEE Nuclear Science Symposium and Medical Imaging Conference Record, volume 10, page 16, 2002.

[Guerra06] A. Del Guerra, A. Bartoli, N. Belcari, D. Herbert, A. Motta, A. Vaiano, G. Di Domenico, N. Sabba, E. Moretti, G. Zavattini*et al. Performance evaluation of the fully engineered YAP-(S) PET scanner for small animal imaging.* IEEE Transactions on Nuclear Science, vol. 53, no. 3, page 1078, 2006.

[Guerra08] P. Guerra, J. E. Ortuno, G. Kontaxakis, M. J. Ledesma-Carbayo, J. J. Vaquero, M. Desco & A. Santos. *Real-Time Digital Timing in Positron Emission Tomography.* IEEE Transactions on Nuclear Science, vol. 55, no. 5 Part 1, pages 2531–2540, 2008.

[Hasegawa04] T. Hasegawa, E. Yoshida, T. Yamaya, K. Maruyama & H. Murayama. *On-clock non-paralyzable count-loss model.* Physics in Medicine and Biology, vol. 49, no. 4, pages 547–555, 2004.

[Herraiz05] J. L. Herraiz, S. Espana, J. M. Udias, J. J. Vaquero & M. Desco. *Statistical Reconstruction Methods in PET: Resolution Limit, Noise, Edge Artifacts and considerations for the design of better scanners.* In IEEE Nuclear Science Symposium and Medical Imaging Conference Record, 2005.

[Heywang-Köbrunner96] S. H. Heywang-Köbrunner, R. Beck, R. Patt, T. Hilbertz & A. L. Baert. Contrast-enhanced MRI of the breast. Springer, 1996.

[Hoh97] C. K. Hoh, C. Schiepers, M. A. Seltzer, S. S. Gambhir, D. H. S. Silverman, J. Czernin, J. Maddahi & M. E. Phelps. *PET in oncology: Will it replace the other modalities?* Seminars in Nuclear Medicine, vol. 27, no. 2, pages 94–106, 1997.

[Houssami09] N. Houssami & D. F. Hayes. *Review of Preoperative Magnetic Resonance Imaging (MRI) in Breast Cancer: Should MRI Be Performed on All Women with Newly Diagnosed, Early Stage Breast Cancer?* CA: A Cancer Journal for Clinicians, page caac.20028, 2009.

[Huber03] J. S. Huber, W. S. Choong, J. Wang, J. S. Maltz, J. Qi, E. Mandelli & W. W. Moses. *Development of the LBNL positron emission mammography camera.* IEEE Transactions on Nuclear Science, vol. 50, no. 5 Part 2, pages 1650–1653, 2003.

[Huber06] J. S. Huber, W. W. Moses, G. C. Wang, S. E. Derenzo, R. H. Huesman, J. Qi, P. Virador, W. S. Choong, E. Mandelli, E. Beuville*et al. A retrospective on the LBNL PEM project.* Physica Medica, vol. 21, page 60–63, 2006.

[Humm03] J. Humm, A. Rosenfeld & A. Del Guerra. *From PET detectors to PET scanners.* European Journal of Nuclear Medicine and Molecular Imaging, vol. 30, no. 11, pages 1574–1597, 2003.

[IARC04] IARC. *Tobacco Smoke and Involuntary Smoking.* Technical report, International Agency for Researchon Cancer, 2004.

[Jaffray02] D. A. Jaffray, J. H. Siewerdsen, J. W. Wong & A. A. Martinez. *Flat-panel cone-beam computed tomography for image-guided radiation therapy.* International Journal of Radiation Oncology, Biology, Physics, vol. 53, no. 5, pages 1337–1349, 2002.

[Jemal09] A. Jemal, R. Siegel, E. Ward, Y. Hao, J. Xu & M. J. Thun. *Cancer Statistics, 2009.* CA A Cancer Journal for Clinicians, vol. 59, no. 4, pages 225–249, 2009.

[Joly09] B. Joly, G. Montarou, J. Lecoq, G. Bohner, M. Crouau, M. Brossard & P. E. Vert. *Test and Optimization of Timing Algorithms for PET Detectors with Digital Sampling Front-end.* In IEEE Nuclear Science Symposium and Medical Imaging Conference Record, pages 3353–3360, 2009.

[Jordanov94] V. T. Jordanov & G. F. Knoll. *Digital synthesis of pulse shapes in real time for high resolution radiation spectroscopy.* Nuclear Instruments and Methods in Physics Research Section A, vol. 345, no. 2, pages 337–345, 1994.

[Jr00] E. F. Patz Jr, P. C. Goodman & G. Bepler. *Screening for lung cancer.* The New England Journal of Medicine, vol. 343, no. 22, pages 1627–33, 2000.

[Karp08] J.S. Karp, S. Surti, M.E. Daube-Witherspoon & G. Muehllehner. *Benefit of time-of-flight in PET: experimental and clinical results.* Journal of Nuclear Medicine, vol. 49, no. 3, page 462, 2008.

[Kitamura08a] K. Kitamura & H. Kudo. *MAP-EM reconstruction using uniform background template for limited-angle PEM.* In IEEE Nuclear Science Symposium and Medical Imaging Conference Record, pages 4172–4174, 2008.

[Kitamura08b] K. Kitamura, J. Ohi, H. Tonami, Y. Yamada, T. Furumiya, M. Furuta, M.u Satoh, T. Tsuda, M. Nakazawa, N. Hashizume, Y. Yamakawa, A. Kawashima & Y. Kumazawa. *Development of a C-shaped breast PET scanner equipped with four-layer DOI detectors.* In IEEE Nuclear Science Symposium and Medical Imaging Conference Record, pages 5662–5665, 2008.

[Kramer00] M. Kramer, O. Jakel, T. Haberer, G. Kraft, D. Schardt & U. Weber. *Treatment planning for heavy-ion radiotherapy: physical beam model and dose optimization.* Physics in Medicine and Biology, vol. 45, no. 11, pages 3299–3318, 2000.

[Kriege04] M. Kriege, C. T. M. Brekelmans, C. Boetes, P. E. B., H. M. Zonderland, I. M. Obdeijn, R. A. Manoliu, T. Kok, H. Peterse, M. M. A. Tilanus-Linthorst, S. H. Muller, S. Meijer, J. C. Oosterwijk, L. V. A. M. Beex, R. A. E. M. Tollenaar, H. J. de Koning, E. J. T. Rutgers, J. G. M. Klijn & the Magnetic Resonance Imaging Screening Study Group. *Efficacy of MRI and Mammography for Breast-Cancer Screening in Women with a Familial or Genetic Predisposition.* The New England Journal of Medicine, vol. 351, no. 5, pages 427–437, 2004.

[Kuhl00] C. K. Kuhl, R. K. Schmutzler, C. C. Leutner, A. Kempe, E. Wardelmann, A. Hocke, M. Maringa, U. Pfeifer, D. Krebs & H. H. Schild. *Breast MR*

Imaging Screening in 192 Women Proved or Suspected to Be Carriers of a Breast Cancer Susceptibility Gene: Preliminary Results. Radiology, vol. 215, no. 1, pages 267–279, 2000.

[Lamare05] F. Lamare, S. L. Bowen, D. Visvikis, P. Cortes, Y. Wu, V. H. Tran, J. M. Boone, S. R. Cherry & R. D. Badawi. *Design simulation of a rotating dual-headed PET/CT scanner for breast imaging.* In IEEE Nuclear Science Symposium and Medical Imaging Conference Record, volume 3, 2005.

[Lecoq02] P. Lecoq & J. Varela. *Clear-PEM, a dedicated PET camera for mammography.* Nuclear Instruments and Methods in Physics Research Section A, vol. 486, no. 1-2, pages 1–6, 2002.

[Leong06] C. Leong, P. Bento, P. Lous a, J. Nobre, J. Rego, P. Rodrigues, J. C. Silva, I. C. Teixeira, J. P. Teixeira, A. Trindade*et al.* *Design and test issues of an FPGA based data acquisition system for medical imaging using PEM.* IEEE Transactions on Nuclear Science, vol. 53, no. 3, page 761, 2006.

[Levin99] C. S. Levin & E. J. Hoffman. *Calculation of positron range and its effect on the fundamental limit of positron emission tomography system spatial resolution.* Physics in Medicine and Biology, vol. 44, no. 3, pages 781–799, 1999.

[Levine03] E. A. Levine, R. I. Freimanis, N. D. Perrier, K. Morton, N. M. Lesko, S. Bergman, K. R. Geisinger, R. C. Williams, C. Sharpe, V. Zavarzin*et al.* *Positron emission mammography: initial clinical results.* Annals of Surgical Oncology, vol. 10, no. 1, page 86–91, 2003.

[Liberman04] L. Liberman. *Breast Cancer Screening with MRI-What Are the Data for Patients at High Risk?* New England Journal of Medicine, vol. 351, no. 5, page 497, 2004.

[Litzenberg92] D. W. Litzenberg, J. F. Bajema, F. D. Becchetti, D. A. Roberts, R. Ronningen, S. Van der Molen, J. A. Brown, R. K. Ten Haken, J. Caraher, C. Hazard*et al.* *On-line monitoring and PET imaging of proton radiotherapy beams.* In IEEE Nuclear Science Symposium and Medical Imaging Conference Record, volume 4, 1992.

[Llacer88] J. Llacer. *Positron emission medical measurements with accelerated radioactive ion beams.* Nuclear Science Applications, vol. 3, pages 111–131, 1988.

[Lu07] G. Lu, Z. Wang, H. Zhu, L. Chang, Y. Chen, J. Wu & Y. Zhao. *The advantage of PET and CT integration in examination of lung tumors.* Journal of Biomedical Imaging, vol. 2007, no. 2, page 8, 2007.

[Luo08] W. Luo, E. Anashkin & C. G. Matthews. *First test results of a commercially available clinical PET scanner using the NEMA NU 4-2008 small animal PET standards.* In IEEE Nuclear Science Symposium and Medical Imaging Conference Record, page 4718–4723, 2008.

[MacDonald08] L. MacDonald, J. Edwards, T. Lewellen, J. Rogers & P. Kinahan. *Clinical imaging characteristics of the positron emission mammography PEM Flex Solo II.* In IEEE Nuclear Science Symposium and Medical Imaging Conference Record, page 4494–4501, 2008.

[MacDonald09a] L. MacDonald, J. Edwards, T. Lewellen, D. Haseley, J. Rogers & P. Kinahan. *Clinical Imaging Characteristics of the Positron Emission Mammography Camera: PEM Flex Solo II.* Journal of Nuclear Medicine, vol. 50, no. 10, pages 1666–1675, 2009.

[MacDonald09b] L. MacDonald, J. Edwards, T. Lewellen, D. Haseley, J. Rogers & P. Kinahan. *Clinical Imaging Characteristics of the Positron Emission Mammography Camera: PEM Flex Solo II.* Journal of Nuclear Medicine, vol. 50, no. 10, page 1666, 2009.

[Mano01] M. M. Mano. *Digital Design*, 2001. Chapter 3: Simplification of Boolean Functions.

[Maramraju08a] S. H. Maramraju, S. Junnarkar, B. Ravindranath, S. Southekal, S. Stoll, S. D. Smith, W. Lenz, J.-F. Pratte, M. Purschke, S. Rescia, S. Krishnamoorthy, P. Vaska, C. Woody & D. Schlyer. *An MR compatible PET scanner based on RatCAP for small animal imaging at 9.4 T.* In IEEE Nuclear Science Symposium and Medical Imaging Conference Record, pages 3679–3682, 2008.

[Maramraju08b] S. H. Maramraju, D. Schlyer, P. Vaska, C. Woody, S. Junnarkar, B. Ravindranath, S. Southekal, D. Smith, D. Tomasi & W. Lenz. *Acquisition of simultaneous PET-MRI images based on RatCAP PET detector in the 9.4 T MRI.* In Society of Nuclear Medicine Annual Meeting Abstracts, volume 49, page 67P, 2008.

[Martinez05] L. Moliner Martinez, A. Soriano Asensi, A. Orero Palomares, M. Carles Farinya, F. Sanchez Martinez, J. M. Benlloch Baviera, C. Correcher Salvador & A. Gonzalez Martinez. *Performance Characteristics of the MAMMI PEMT Scanner Based on NEMA NU 2-2007.* In IEEE Nuclear Science Symposium and Medical Imaging Conference Record, 2005.

[McElroy05] D. P. McElroy, M. Hoose, W. Pimpl, V. Spanoudaki, T. Schüler & S. I. Ziegler. *A true singles list-mode data acquisition system for a small animal PET scanner with independent crystal readout.* Physics in Medicine and Biology, vol. 50, no. 14, pages 3323–3335, 2005.

[Müller06] H. Müller & W. Enghardt. *In-beam PET at high-energy photon beams.* Physics in Medicine and Biology, vol. 51, pages 1779–1789, 2006.

[Moehrs08] S. Moehrs, M. Defrise, N. Belcari, A.D. Guerra, A. Bartoli, S. Fabbri & G. Zanetti. *Multi-ray-based* *system matrix generation for 3D PET reconstruction.* Physics in medicine and biology, vol. 53, page 6925, 2008.

[Moses93] W. W. Moses & W. W. Derenzo. *Empirical observation of performance degradation in positron emission tomographs utilizing block detectors.* Journal of Nuclear Medicine, vol. 34, 1993.

[Moses01] W. W. Moses, J. W. Young, K. Baker, W. Jones, M. Lenox, M. H. Ho & M. Weng. *The electronics system for the LBNL positron emission mammography (PEM) camera.* IEEE Transactions on Nuclear Science, vol. 48, no. 3, pages 632–636, 2001.

[Moses06] W. W. Moses & C. J. Thompson. *Timing Calibration in PET Using a Time Alignment Probe.* IEEE Transactions on Nuclear Science, vol. 53, no. 5, pages 2660–2665, 2006.

[Motta04] A. Motta, S. Righi, A. Del Guerra, N. Belcari, A. Vaiano, G. Di Domenico, G. Zavattini, R. Campanini, N. Lanconelli & A. Riccardi. *A full Monte Carlo simulation of the YAP-PEM prototype for breast tumor detection.* Nuclear Instruments and Methods in Physics Research Section A, vol. 527, no. 1-2, page 201–205, 2004.

[Motta05] A. Motta, A. Del Guerra, N. Belcari, S. Moehrs, D. Panetta, S. Righi & D. Valentini. *Fast 3D-EM reconstruction using Planograms for stationary planar positron emission mammography camera.* Computerized Medical Imaging and Graphics, vol. 29, no. 8, pages 587–596, 2005.

[Mulshine05] J. L. Mulshine. *Clinical issues in the management of early lung cancer.* Clinical Cancer Research, vol. 11, no. 13, page 4993s, 2005.

[Munzenrider99] J. E. Munzenrider & N. J. Liebsch. *Proton therapy for tumors of the skull base.* Strahlentherapie und Onkologie, vol. 175, page 57–63, 1999.

[Murthy97] K. Murthy, A. Bergman, C. Thompson, J. Robar, R. Lisbona, A. Loutfi & J. Gagnon. *Early clinical results from PEM 1: a high resolution system for-positron emission mammography.* In IEEE Nuclear Science Symposium and Medical Imaging Conference Record, volume 2, 1997.

[Murthy99] K. Murthy, D. Jolly, M. Aznar, C. J. Thompson, P. Sciascia, A. Loutfi, R. Lisbona & J. H. Gagnon. *Quantification in Positron Emission Mammography (PEM) with Planar Detectors: Contrast Resolution Measurements Using a Custom Breast Phantom and Novel Spherical Hot-Spots.* IEEE Transactions on Nuclear Science, vol. 46, no. 6, page 2192–2196, 1999.

[Murthy00a] K. Murthy, M. Aznar, A. M. Bergman, C. J. Thompson, J. L. Robar, R. Lisbona, A. Loutfi & J. H. Gagnon. *Positron Emission Mammographic Instrument: Initial Results.* Radiology, vol. 215, no. 1, page 280, 2000.

[Murthy00b] K. Murthy, M. Aznar, C. J. Thompson, R. Lisbona, A. Loutfi & J. H. Gagnon. *Preliminary clinical evaluation of an instrument for positron emission mammography (PEM-I).* Journal of Nuclear Medicine, vol. 41, no. 12, page 1851–1858, 2000.

[Murthy00c] K. Murthy, M. Aznar, C. J. Thompson, A. Loutfi, R. Lisbona & J. H. Gagnon. *Results of Preliminary Clinical Trials of the Positron Emission Mammography System PEM-I: A Dedicated Breast Imaging System Producing Glucose Metabolic Images Using FDG.* Journal of Nuclear Medicine, vol. 41, no. 11, pages 1851–1858, 2000.

[Nakhostin09] M. Nakhostin, K. Ishii, Y. Kikuchi, S. Matsuyama, H. Yamazaki & A. E. Torshabi. *Time resolution improvement of Schottky CdTe PET detectors using digital signal processing.* Nuclear Instruments and Methods in Physics Research Section A, vol. 606, no. 3, pages 681–688, 2009.

[Oelfke96] U. Oelfke, G. K. Y. Lam & M. S. Atkins. *Proton dose monitoring with PET: quantitative studies in Lucite.* Physics in Medicine and Biology, vol. 41, pages 177–196, 1996.

[Olcott05] P. D. Olcott, J. A. Talcott, C. S. Levin, F. Habte & A. M. K. Foudray. *Compact readout electronics for position sensitive photomultiplier tubes.* IEEE Transactions on Nuclear Science, vol. 52, no. 1, pages 21–27, 2005.

[Oliver08] Josep F. Oliver, I. Torres-Espallardo, R. Fontaine, S. I. Ziegler & M. Rafecas. *Comparison of coincidence identification techniques for high resolution PET.* In IEEE Nuclear Science Symposium and Medical Imaging Conference Record, pages 4732 – 4735, oct. 2008.

[Paans92] A. M. J. Paans & J. M. Schippers. *Proton therapy in combination with PET as monitor: a feasibilitystudy.* In IEEE Nuclear Science Symposium and Medical Imaging Conference Record, pages 957–959, 1992.

[Park08] S. J. Park, S. Southekal, M. Purschke, S. S. Junnarkar, J. F. Pratte, S. P. Stoll, C. L. Woody, D. J. Schlyer & P. Vaska. *Digital coincidence processing for the RatCAP conscious rat brain PET scanner.* IEEE Transactions on Nuclear Science, vol. 55, no. 1, pages 510–515, 2008.

[Parodi02] K. Parodi, W. Enghardt & T. Haberer. *In-beam PET measurements of $\beta+$ radioactivity.* Physics in Medicine and Biology, vol. 47, pages 21–36, 2002.

[Parodi05] K. Parodi, P. Crespo, H. Eickhoff, T. Haberer, J. Pawelke, D. Schardt & W. Enghardt. *Random coincidences during in-beam PET measurements at microbunched therapeutic ion beams.* Nuclear Instruments and Methods in Physics Research Section A, vol. 545, no. 1-2, pages 446–458, 2005.

[Parodi07a] K. Parodi, H. Paganetti, E. Cascio, J. B. Flanz, A. A. Bonab, N. M. Alpert, K. Lohmann & T. Bortfeld. *PET/CT imaging for treatment verification after proton therapy: A study with plastic phantoms and metallic implants.* Medical Physics, vol. 34, no. 2, pages 419–435, 2007.

[Parodi07b] K. Parodi, H. Paganetti, H. A. Shih, S. Michaud, J. S. Loeffler, T. F. DeLaney, N. J. Liebsch, J. E. Munzenrider, A. J. Fischman, A. Knopf & T. Bortfeld. *Patient Study of In Vivo Verification of Beam Delivery and Range, Using Positron Emission Tomography and Computed Tomography Imaging After Proton Therapy.* International Journal of Radiation Oncology, Biology, Physics, vol. 68, no. 3, pages 920–934, 2007.

[Parodi08a] K. Parodi, T. Bortfeld, W. Enghardt, F. Fiedler, A. Knopf, H. Paganetti, J. Pawelke, G. Shakirin & H. Shih. *PET imaging for treatment verification of ion therapy: Implementation and experience at GSI Darmstadt and MGH Boston.* Nuclear Instruments and Methods in Physics Research Section A, vol. 591, no. 1, pages 282–286, 2008. Radiation Imaging Detectors 2007 - Proceedings of the 9th International Workshop on Radiation Imaging Detectors.

[Parodi08b] K. Parodi, T. Bortfeld & T. Haberer. *Comparison Between In-Beam and Offline Positron Emission Tomography Imaging of Proton and Carbon Ion Therapeutic Irradiation at Synchrotron- and Cyclotron-Based Facilities.* International Journal of Radiation Oncology, Biology, Physics, vol. 71, no. 3, pages 945–956, 2008.

[Pawelke96] J. Pawelke, L. Byars, W. Enghardt, W. D. Fromm, H. Geissel, B. G. Hasch, K. Lauckner, P. Manfrass, D. Schardt & M. Sobiella. *The investigation of different cameras for in-beam PET imaging.* Physics in Medicine and Biology, vol. 41, pages 279–296, 1996.

[Ramirez09] R. A. Ramirez, Y. Zhang, S. Liu, H. Li, H. Baghaei, S. An, C. Wang, M. L. Jan & W. H. Wong. *A Lower-Cost High-Resolution LYSO Detector Development for Positron Emission Mammography (PEM).* IEEE Transactions on Nuclear Science, vol. 56, no. 5, pages 2621–2627, 2009.

[Ravindranath08] B. Ravindranath, S. H. Maramraju, S. S. Junnarkar, S. S. Southekal, S. P. Stoll, J.-F. Pratte, M. L. Purschke, X. Hong, D. Bennett, K. Cheng, D. Tomasi, D. S. Smith, S. Krishnamoorthy, P. Vaska, C. L. Woody & D. J. Schlyer. *A simultaneous PET/MRI breast scanner based on the RatCAP.* In IEEE Nuclear Science Symposium and Medical Imaging Conference Record, pages 4650–4655, 2008.

[Raylman00] R. R. Raylman, S. Majewski, R. Wojcik, A. G. Weisenberger, B. Kross, V. Popov & H. A. Bishop. *The potential role of positron emission mammography for detection of breast cancer. A phantom study.* Medical Physics, vol. 27, no. 8, pages 1943–1954, 2000.

[Raylman05] R. R. Raylman, M. F. Smith & P. R. Menge. *A Monte-Carlo simulation study of detector array design for dedicated breast metabolic imaging systems.* Nuclear Instruments and Methods in Physics Research Section A, vol. 555, no. 1-2, pages 403–410, 2005.

[Raylman08a] R. R. Raylman, S. Majewski, M. F. Smith, J. Proffitt, W. Hammond, A. Srinivasan, J. McKisson, V. Popov, A. Weisenberger, C. O. Judy, B. Kross, S. Ramasubramanian, L. E. Banta, P. E. Kinahan & K. Champley. *The positron emission mammography/tomography breast imaging and biopsy system (PEM/PET): design, construction and phantom-based measurements.* Physics in Medicine and Biology, vol. 53, no. 3, pages 637–653, 2008.

[Raylman08b] R. R. Raylman, M. F. Smith, P. E. Kinahan & S. Majewski. *Quantification of radiotracer uptake* *with a dedicated breast PET imaging system.* Medical Physics, vol. 35, no. 11, pages 4989–4997, 2008.

[Ribeiro04] R. Ribeiro, C. Abreu, P. Almeida, F. Balau, P. Bordalo, N. C. Ferreira, S. Fetal, F. Fraga, P. Lecoq, M. Martins, N. Matela, R. Moura, C. Ortig ao, L. Peralta, S. Ramos, P. Rato, P. Rodrigues, A. I. Santos, A. Trindade & J. Varela. *Breast imaging with a dedicated PEM.* Nuclear Instruments and Methods in Physics Research Section A, vol. 527, no. 1-2, pages 87–91, 2004.

[Robar97] J. L. Robar, C. J. Thompson, K. Murthy, R. Clancy & A. M. Bergman. *Construction and calibration of detectors for high-resolution metabolic breast cancer imaging.* Nuclear Instruments and Methods in Physics Research Section A, vol. 392, no. 1, page 402–406, 1997.

[Rodgers88] J. L. Rodgers & W. A. Nicewander. *Thirteen Ways to Look at the Correlation Coefficient.* The American Statistician, vol. 42, no. 1, pages 59–66, 1988.

[Rodrigues07] P. Rodrigues, A. Trindade & J. Varela. *Clear-PEM system counting rates: a Monte Carlo study.* Journal of Instrumentation, vol. 2, no. 01, page P01004, 2007.

[Santos04] A. I. Santos, P. Almeida, M. V. Martins, N. Matela, N. Oliveira, N. C. Ferreira, J. D. Aguiar, F. G. Almeida, F. Lopes, J. Sampaio*et al.* *Design and evaluation of the Clear-PEM detector for positron emission mammography.* In IEEE Nuclear Science Symposium and Medical Imaging Conference Record, volume 6, 2004.

[Schilling08] K. Schilling, P. Conti, L. Adler & L. Tafra. *The role of positron emission mammography in breast cancer imaging and management.* Applied Radiology, vol. 37, no. 4, page 26, 2008.

[Schoder07] H. Schoder & M. Gonen. *Screening for cancer with PET and PET/CT: potential and limitations.*

Journal of Nuclear Medicine, vol. 48, no. 1 suppl., page 4S, 2007.

[Schuster07] D. M. Schuster, J. R. Votaw, P. T. Nieh, W. Yu, J. A. Nye, V. Master, F. D. B. Bowman, M. M. Issa & M. M. Goodman. *Initial experience with the radiotracer anti-1-amino-3-18F-fluorocyclobutane-1-carboxylic acid with PET/CT in prostate carcinoma.* Journal of Nuclear Medicine, vol. 48, no. 1, page 56, 2007.

[Semmler08] W. Semmler & M. Schwaiger. Molecular imaging. Springer, 2008.

[Stickel05] J. R. Stickel & S. R. Cherry. *High-resolution PET detector design.* Physics in Medicine and Biology, vol. 50, page 179–195, 2005.

[Swann04] B. K. Swann, B. J. Blalock, L. G. Clonts, D. M. Binkley, J. M. Rochelle, E. Breeding & K. M. Baldwin. *A 100-ps time-resolution CMOS time-to-digital converter for positron emission tomography imaging applications.* IEEE Journal of Solid-State Circuits, vol. 39, no. 11, page 1839–1852, 2004.

[Tafra05] L. Tafra, Z. Cheng, J. Uddo, M. B. Lobrano, W. Stein, W. A. Berg, E. Levine, I. N. Weinberg, D. Narayanan, E. Ross*et al. Pilot clinical trial of 18F-fluorodeoxyglucose positron-emission mammography in the surgical management of breast cancer.* The American Journal of Surgery, vol. 190, no. 4, page 628–632, 2005.

[Tafra07] L. Tafra. *Positron Emission Tomography (PET) and Mammography (PEM) for Breast Cancer: Importance to Surgeons.* Annals of Surgical Oncology, vol. 14, no. 1, pages 3–13, 2007.

[Thompson94] C. J. Thompson, K. Murthy, I. N. Weinberg & F. Mako. *Feasibility study for positron emission mammography.* Medical Physics, vol. 21, page 529–529, 1994.

[Thompson95] C.J. Thompson, K. Murthy, Y. Picard, I. N. Weinberg & R. Mako. *Positron emission mammography (PEM): a promising technique for detecting breast cancer.* IEEE Transactions on Nuclear Science, vol. 42, no. 4, pages 1012–1017, 1995.

[Thompson06] C. J. Thompson. *Instrumentation for positron emission mammography.* PET Clinics, vol. 1, no. 1, page 33–38, 2006.

[Tonami07] H. Tonami, J. Ohi, K. Kitamura, M. Satoh, T. Tsuda & Y. Kumazawa. *Sophisticated* $32 \times 32 \times 4$*-layer DOI detector for high resolution PEM scanner.* In IEEE Nuclear Science Symposium and Medical Imaging Conference Record, volume 5, pages 3803–3807, 2007.

[Trindade03] A. Trindade, P. Almeida, F. Balau, N. Ferreira, S. Fetal, F. Fraga, M. Martins, N. Matela, P. Mendes, R. Moura*et al.* *Clear-PEM: Monte Carlo performance and image reconstruction studies.* In IEEE Nuclear Science Symposium and Medical Imaging Conference Record, volume 3, 2003.

[Trummer09] J. Trummer, E. Auffray & P. Lecoq. *Depth of interaction resolution of LuAP and LYSO crystals.* Nuclear Instruments and Methods in Physics Research Section A, vol. 599, no. 2-3, pages 264–269, 2009.

[Uematsu05] T. Uematsu, S. Yuen, S. Yukisawa, T. Aramaki, N. Morimoto, M. Endo, H. Furukawa, Y. Uchida & J. Watanabe. *Comparison of FDG PET and SPECT for detection of bone metastases in breast cancer.* American Journal of Roentgenology, vol. 184, no. 4, page 1266, 2005.

[Varela05] J. Varela, P. Bento, C. Leong, I. C. Teixeira, J. P. Teixeira, J. Nobre, J. Rego, P. Lousa, P. Relvas, P. Rodrigues*et al.* *FPGA Based Architecture for the Data Acquisition Electronics of the Clear-PEM System.* Applied Reconfigurable Computing, page 131, 2005.

[Vecchio08] S. Vecchio. *Development of a positron emission tomograph for in-vivo dosimetry in hadrontherapy.* PhD Thesis, Università di Pisa, 2008.

[Vecchio09] S. Vecchio, F. Attanasi, N. Belcari, M. Camarda, G. A.P Cirrone, G. Cuttone, F. Di Rosa, N. Lanconelli, S. Moehrs, V. Rosso*et al.* *A PET prototype for in-beam monitoring of proton therapy.* IEEE Transactions on Nuclear Science, vol. 56, no. 1 Part 1, pages 51–56, 2009.

[Vynckier93] S. Vynckier, S. Derreumaux, F. Richard, A. Bol, C. Michel & A. Wambersie. *Is it possible to verify directly a proton-treatment plan using positron emission tomography?* Radiotherapy and oncology, vol. 26, no. 3, page 275, 1993.

[Wahl91] R. L. Wahl, R. L. Cody, G. D. Hutchins & E. E. Mudgett. *Primary and metastatic breast carcinoma: initial clinical evaluation with PET with the radiolabeled glucose analogue 2-[F-18]-fluoro-2-deoxy-D-glucose.* Radiology, vol. 179, no. 3, page 765, 1991.

[Wang02] Y. Wang, H. Li, Y. Liu, T. Xing, J. Uribe, F. Baghaei, R. Farrell & W. H. Wong. *A modular low dead-time coincidence system for high resolution PET cameras.* In IEEE Nuclear Science Symposium and Medical Imaging Conference Record, volume 2, 2002.

[Wang04] G.-C. Wang, J. S. Huber, W. W. Moses, W.-S. Choong & J.S. Maltz. *Calibration of a PEM detector with depth of interaction measurement.* IEEE Transactions on Nuclear Science, vol. 51, no. 3, pages 775–781, 2004.

[Wang05] G. C. J. Wang. *Calibration and characterization of the LBNL positron emission mammography camera.* PhD thesis, University of California, Berkeley, 2005.

[Wang06] G. C. Wang, J. S. Huber, W. W. Moses, J. Qi & W. S. Choong. *Characterization of the LBNL PEM camera.* IEEE Transactions on Nuclear Science, vol. 53, no. 3 Part 2, page 1129–1135, 2006.

[Watson09] C.C. Watson. *A hybrid algorithm for randoms variance reduction.* In IEEE Nuclear Science Symposium and Medical Imaging Conference Record, pages 3882 –3885, 2009.

[Weinberg93] I. N. Weinberg. *Dedicated apparatus and method for emission mammography.* US patent, no. 5252830, 1993.

[Weinberg96a] I. Weinberg, S. Majewski, A. Weisenberger, A. Markowitz, L. Aloj, L. Majewski, D. Danforth, J. Mulshine, K. Cowan, J. A. Zujewski*et al.* *Preliminary results for positron emission mammography: real-time functional breast imaging in a conventional mammography gantry.* European Journal of Nuclear Medicine and Molecular Imaging, vol. 23, no. 7, page 804–806, 1996.

[Weinberg96b] I. N. Weinberg, J. A. Frank, A. Markowitz, S. Majewski, A. Weisenberger, C. J. Thompson, K. Murthy & F. Mako. *Imaging Characterization of A Prototype Dedicated Instrument for Positron Emission Mammography.* Clinical Nuclear Medicine, vol. 21, no. 2, page 162, 1996.

[Weinberg97] I. N. Weinberg, A. Markowitz, S. Majewski, A. Weisenberger, L. Majewski & R. Wojcik. *Would Breast Compression Improve Visualization of Small Primary Cancers With Scintimammography?-A Feasibility Study.* Clinical Nuclear Medicine, vol. 22, no. 4, page 278, 1997.

[Weinberg02] I. N. Weinberg, P. Y. Stepanov, D. Beylin, V. Zavarzin, E. Anashkin, K. Lauckner, S. Yarnall, M. Doss, R. Pani, L. P. Adler*et al.* *A biopsy-ready PEM scanner with real-time X-ray correlation capability.* In IEEE Nuclear Science Symposium and Medical Imaging Conference Record, volume 2, 2002.

[Weinberg04] I. Weinberg, D. Beylin, S. Yarnall, E. Anashkin, P. Stepanov, S. Dolinsky, V. Zavarzin, W. Peter, K. Lauckner, K. Morton*et al.* *Applications of a PET device with 1.5 mm FWHM intrinsic spatial resolution to breast cancer imaging.* In IEEE International Symposium on Biomedical Imaging: Nano to Macro, page 1396–1399, 2004.

[Weinberg05a] I. N. Weinberg, D. Beylin, V. Zavarzin, S. Yarnall, P. Y. Stepanov, E. Anashkin, D. Narayanan, S. Dolinsky, K. Lauckner & L. P. Adler. *Positron emission mammography: high-resolution biochemical breast imaging.* Technology in cancer research & treatment, vol. 4, no. 1, page 55, 2005.

[Weinberg05b] I. N. Weinberg, D. Beylin, V. Zavarzin, S. Yarnall, P. Y. Stepanov, E. Anashkin, D. Narayanan, S. Dolinsky, K. Lauckner & L. P. Adler. *Positron emission mammography: high-resolution biochemical breast imaging.* Technology in cancer research & treatment, vol. 4, no. 1, page 55, 2005.

[Weinberg06a] I. N. Weinberg. *Applications for positron emission mammography.* Physica Medica, vol. 21, page 132–137, 2006.

[Weinberg06b] I. N. Weinberg, E. Anashkin, D. Narayanan & W. Peter. *Display method for image-based questionnaires.* US patent, no. 11/458,518, 2006.

[Weir05] L. Weir, D. Worsley & V. Bernstein. *The Value of FDG Positron Emission Tomography in the Management of Patients with Breast Cancer.* The Breast Journal, vol. 11, no. 3, pages 204–209, 2005.

[Weissleder01] R. Weissleder & U. Mahmood. *Molecular Imaging.* Radiology, vol. 219, no. 2, pages 316–333, 2001.

[WHO08] WHO. *The global burden of disease: 2004 update.* Technical report, World Health Organization, 2008.

[Wicks77] R. Wicks & M. Blau. *The Effect of Window Fraction on the Deadtime of Anger Cameras: Concise Communication.* Journal of Nuclear Medicine, vol. 18, no. 7, page 732, 1977.

[Wollenweber04] S. D. Wollenweber, R. C. Williams, D. Beylin, S. Dolinsky & I. N. Weinberg. *Investigation of the quantitative capabilities of a positron emission mammography system.* In IEEE Nuclear Science Symposium and Medical Imaging Conference Record, volume 4, 2004.

[Wu09] Y. Wu, S. L. Bowen, K. Yang, N. Packard, L. Fu, G. Burkett, J. Qi, J. M. Boone, S. R. Cherry & R. D. Badawi. *PET characteristics of a dedicated breast PET/CT scanner prototype.* Physics in Medicine and Biology, vol. 54, page 4273–4287, 2009.

[Yamada07] Y. Yamada, K. Kitamura, N. Hashizume, Y. Yamakawa & Y. Kumazawa. *Reconstruction of 4-Layer DOI detector equipped C-shaped PEM via list-mode iterative algorithm.* In IEEE Nuclear Science Symposium and Medical Imaging Conference Record, volume 6, pages 4397–4400, 2007.

[Yamakawa08] Y. Yamakawa, K. Kitamura, Y. Yamada, N. Hashizume, A. Kawashima & Y. Kumazawa. *Random correction using singles count rates for DOI Positron Emission Mammography.* In IEEE Nuclear Science Symposium and Medical Imaging Conference Record, pages 5129–5132, 2008.

[Yasuda05] S. Yasuda & M. Ide. *PET and cancer screening.* Annals of Nuclear Medicine, vol. 19, no. 3, pages 167–177, 2005.

[Zaidi06] H. Zaidi & M.L. Montandon. *The new challenges of brain PET imaging technology.* Current Medical Imaging Reviews, vol. 2, no. 1, pages 3–13, 2006.

[Zhang03] N. Zhang, C. J. Thompson, F. Cayouette, D. Jolly & S. Kecani. *A prototype modular detector design* *for high resolution positron emission mammography imaging.* IEEE Transactions on Nuclear Science, vol. 50, no. 5, page 1624–1629, 2003.

[Zhang08] Y. Zhang, R. Ramirez, H. Li, S. Liu, Sh. An, C. Wang, H. Baghaei, W.-H. Wong & M.-L. Jan. *The system design, engineering architecture and preliminary results of a lower-cost high-sensitivity high-resolution Positron Emission Mammography camera.* In IEEE Nuclear Science Symposium and Medical Imaging Conference Record, pages 4794–4797, 2008.

Acknowledgements

Here we go, we have finished even this chapter. It has not been easy and I could not have accomplished the challenge by my own, without all the help from the people who accompanied me in this journey. Actually, it was so much help, that it might have been hard for them too.

First and foremost I offer my sincerest gratitude to Prof. Andrés Santos, who has supported me through these years, wisely advising, whilst allowing me to work in my own way. Thank you for your trust, and for the opportunity of joining your group. Thanks to Pedro, who most closely assisted me: thanks for your time and for the much work you spent for me. Thanks also to Chus, Giorgos and Eva for your kind support.

Thanks to the friends of the group, Gert, Juan, Jose, Miguel, Ana y Rosario. Thank you for your friendship and for your advices. Thanks to Laura, Carlos, David, Oscar and all the newcomers for the great environment you all made together. It was a big family and I really felt at home.

Many thanks to Prof. Del Guerra for accepting me into your group and for your advices. Thanks to Nicola, for all your time and for your great insights. Thanks to Valeria, for letting me into your workgroup, and for your kind suggestions in the latest phases of this thesis. Thanks to Gabriela for your aid at Pisa, and for the review of the manuscript.

Thanks to my family, at the distance, but always present. Thanks to Javi, Jesus, Carlos and Andrés, for the nice time in the coffee breaks and at lunch time. Many thanks to the friends at Pisa, Sascha, Daniel, Sebnem, Sara V., Sara M. and Francesca, we spent a few time together, but enough to make it very hard to leave.

Thanks to Raquel, for your advices, stories, and the great time in the "Fridays break". They all came when I most needed them. Thanks to Victor, for revising my English, including these acknowledgements. Also thanks for the great time spent together all these years.

To Mariangela: you have been my motivation, my support, my north. Without you I would have not done any of this. Thank you.

I'm sure I'm leaving out somebody, please forgive me, it's the emotion.

“E quindi uscimmo a riveder le stelle”

Dante Alighieri,
Divina Commedia, Inferno XXXIV, 139.